

Alternative Wide-Band-Gap Materials for Gamma-Ray Spectroscopy

by

Crystal L. Thrall

A dissertation submitted in partial fulfillment
of the requirements for the degree of
Doctor of Philosophy
(Nuclear Engineering and Radiological Sciences)
in The University of Michigan
2013

Doctoral Committee:

Professor Zhong He, Chair
Professor Roy Clarke
Research Scientist Mark D. Hammig
Professor Emeritus Glenn F. Knoll
Professor Sara A. Pozzi

© Crystal L. Thrall 2013

All Rights Reserved

To my family.

ACKNOWLEDGEMENTS

As I contemplated whom I should acknowledge, I recognized that this dissertation would not have been even remotely possible without the continuous support I received from my family, fellow researchers, and friends. I owe my deepest gratitude to my husband, Brian Kitchen, who supported me emotionally, physically, spiritually, and intellectually through every moment of my graduate school career. To my parents, Ken and Edna Thrall, who always played an active role in my education and emphasized its importance. Without them, my higher education at the University of Michigan simply would not have been possible. I would also like to thank my daughter, Rae, for inspiring me to complete this work and my sister, Christine, for providing an artist's perspective on my research.

I am extremely privileged to have been a part of the Orion group. I am indebted to my advisor, Professor Zhong He, for his guidance and support throughout my six years of graduate school. As Professor He has reminded me numerous times, the Orion group would not be successful without the great work of his graduate students. It has been a truly humbling experience to work alongside such brilliant and hard-working individuals: Dr. Feng Zhang, Dr. JaeCheon Kim, Dr. Steve Anderson, Dr. Weiyi Wang, Dr. Chris Wahl, Dr. Yuefeng Zhu, Dr. Jason Jaworski, Dr. Andy Boucher, Sonal Joshi, Hao Yang, Josh Mann, and Steven Brown. I would especially like to thank Dr. Willy Kaye, Dr. Miesher Rodrigues, Dr. Burcin Donmez, and Will Koehler and for their insightful discussions that helped my research. I also owe my gratitude to James Berry for his electrical engineering expertise and technical

support.

Additionally, I would like to thank Professor Glenn Knoll, Professor Sara Pozzi, Professor Roy Clarke, and Dr. Mark Hammig for serving on my committee and providing insight for this work.

I am also very fortunate to have been a part of the University of Michigan Nuclear Engineering community for the past decade, to which I owe many thanks to Pam Derry. I was touring the campus before I had been admitted into the undergraduate engineering program when I received a note requesting my presence in her office. During that meeting, Pam convinced a timid high school kid to pursue a Nuclear Engineering degree. Since then, I feel as if this department has become my second family. I am especially appreciative of the NERS women, Anne Campbell, Jennifer Dolan, Sarah Gucker, Cassie Brown, Sonal Joshi, Eva Sunny, Emily Wolters, and Jinan Yang who created a community in a place where women are difficult to find. The friendship and mentorship of my fellow nukes who graduated before me, John Harvey, Adrienne Lehnert, Chris Wahl, Troy Becker, Greg Davidson, Seth Johnson, Eva Sunny, Emily Wolters, and Jinan Yang, helped me find confidence that I would also one day complete my graduate studies. I also owe my gratitude to Ed Birdsall, Sheena Lewis, Cherilyn Davis, Peggy Gramer, Shannon Thomas, and Carolin Joaquin for the many favors they've done at my request.

I am also incredibly blessed to have many friends outside my family and the department who were essential for me to maintain stability in other aspects of my life throughout graduate school. I owe many thanks to my small group, the Humphries, the Carters, the Alexanders, the Gardiniers, and the Wards, for their prayers and emotional support. To my mommy friends, Ceris Geoghegan, Karen Duff, Brianna Ballard, Adrienne Clarke, Constanze Huther, Natalia Czap, Catherine Horning, Leigh Ann Phillips-Knope, and all of the Ann Arbor Babywearers, thank you for helping me with my transition into parenthood. A mom's most valuable information re-

source is a mom network, and I don't know how I could have juggled grad school and mommy responsibilities without your babywearing, sleeping, elimination communication, breastfeeding, teething, and general parenting wisdom.

Finally to my fellow thesis-writing friends, Alex Evans and Azaree Lintereur, I owe you many thanks for providing a safe place to complain. We have walked very similar paths and shared similar struggles through graduate school, so I could always commiserate with you. Your dedication and hard work has been a continuous source of inspiration.

TABLE OF CONTENTS

DEDICATION	ii
ACKNOWLEDGEMENTS	iii
LIST OF FIGURES	viii
LIST OF TABLES	xviii
ABSTRACT	xix
CHAPTER	
I. Introduction	1
1.1 Motivation for Thallium-bromide Development	1
1.2 The Evolution of Thallium-bromide and its Current Challenges	2
1.3 Contribution of This Work	4
II. Theory	5
2.1 Signal Generation and the Shockley-Ramo Theorem	5
2.2 Depth Sensing and Energy Correction	10
2.3 Material Properties	13
2.4 Ionic Conduction	14
III. Detector Fabrication, Experimental Setup, and Methods	18
3.1 TlBr Detector Fabrication and Design	18
3.2 Experimental Setup	20
3.2.1 Standard Experimental Setup	20
3.2.2 Collimator Measurement Setup	22
3.3 Methods	22
3.3.1 Data Post-processing	22
3.3.2 Gamma-ray Data Analysis	26

3.3.3	Alpha Waveform Analysis	27
IV.	Characterization of Stable Operation	29
4.1	Depth Reconstruction	29
4.2	Spectroscopic Performance	31
4.3	Material Properties	35
4.3.1	Electron Drift Velocity	38
4.4	Summary	38
V.	Characterization of the Conditioning Phase	47
5.1	Results	48
5.2	Discussion	55
5.3	Summary	65
VI.	Characterization of Room Temperature Operation	67
6.1	Methods	67
6.2	Results	68
6.2.1	Detector 70BA1R	68
6.2.2	Detector 70BA1L	73
6.2.3	Detector 47AR(R)	75
6.3	Discussion	76
VII.	Investigation of Other Alternative Wide-Band-Gap Materials	88
7.1	Mercuric-sulfide	88
7.1.1	RMD, Inc. Detectors	88
7.1.2	University of Michigan Detectors	92
7.2	Mecuric-oxide	94
7.3	Summary	99
VIII.	Conclusions and Future Work	100
8.1	Conclusions	100
8.2	Future Work	101
BIBLIOGRAPHY	104

LIST OF FIGURES

Figure

2.1	(a) The geometry of a semiconductor detector with planar electrodes. (b) The anode weighting potential as a function of normalized detector depth for a planar detector. The motion of both electrons and holes contribute to the signal.	7
2.2	(a) The geometry of an ionization chamber with a Frisch Grid. (b) The anode weighting potential as a function of distance. The weighting potential is zero except near the anode.	9
2.3	(a) The geometry of semiconductor detector with a pixelated anode and planar cathode. The P represents the pixel-to-pixel pitch. (b) The anode and cathode weighting potentials as a function of detector depth. The anode weighting potential was calculated for the center of the central pixel for a typical TlBr detector.	11
2.4	Example cathode waveforms illustrating measurable hole movement. The solid line illustrates a cathode-side event with only electrons contributing to the signal. The dashed lines indicate the hole component of the cathode signal for interactions occurring at various detector depths. By using a shaping time long enough to eliminate ballistic deficit in the electron component, the measured cathode signal amplitude loses its depth dependence.	12
2.5	(a) An example of a depth-separated spectrum for a detector with high $\mu_h\tau_h$ such that the CAR is overestimated. (b) The same spectrum separated by time.	13
2.6	(a) Illustration of ionic conduction via vacancy migration. Analogous to hole conduction, vacancies conduct as ions vacate their lattice positions to nearby vacancies. (b) Illustration of ionic conduction via interstitial migration.	16

3.1	(a) Graphical representation of a typical TlBr ingot. The heater ring moves from right to left, therefore the impurity concentration increases from right to left. The ingot is divided into three sections and given a letter designation. Each section is further subdivided as shown in the figure. The dark area represents the unusable end of the ingot where most of the impurities reside at the end of crystal growth and purification. (b) A cross-sectional representation of a typical TlBr ingot. The L and R at the end of the detector name represents the right or left side of the ingot. Because L and R originate from the same section of the ingot, they should have similar physical characteristics and therefore similar detector performance.	19
3.2	A photograph of a typical TlBr detector fabricated by RMD. (a) The pixel array. The top row and left column of "pixels" are grounded to create a guard ring. (b) The cathode side. A hole is drilled into the substrate to allow alpha particle irradiation in some detectors. (c) Map of pixels to their number designations. The G's represent "pixels" grounded together to form a guard ring. These grounded "pixels" are also connected to the metal strips surrounding the pixel array.	20
3.3	Block diagram illustration of the data acquisition setup. The aluminum enclosure contains the detector and readout electronics. All ten channels (nine anode pixels and the planar cathode) are connected to the Gage digitizer on the personal computer via RG174 coaxial cables. The $\pm 6V$ power supply powers the preamplifiers and the high voltage supply provides high voltage for the cathode. . . .	21
3.4	Schematic of the printed circuit board used to test TlBr detectors. .	23
3.5	Test pulse preamplifier output signal amplitudes for each channel. Channel-by-channel signal gain variations are corrected using the methods described in Section 3.3.2.1.	24
3.6	Block diagram of the collimator measurement setup. The separation between the two blocks of tungsten is controlled by a micrometer. The vertical position of the collimator is controlled by a positioning stage and measured with a micrometer. This diagram is not to scale.	24
3.7	A photograph of inside the detector enclosure demonstrates the geometry constraints for the collimator setup. The detector is as close as possible to the edge of the enclosure, and the collimator was placed directly in front of the detector.	25
3.8	Collecting pixel (with positive slopes near time zero) and the cathode (with negative slopes during $-10 \mu s \leq t < 0 \mu s$) photopeak waveforms measured from ^{137}Cs irradiating all depths. The slow rise in the cathode waveforms, which are plotted negative to differentiate from anode pulses, indicates hole collection.	28

3.9	From left to right: the raw alpha waveforms after filtering, the normalized alpha waveforms, and the aligned waveforms after applying a baseline shift. In each figure, the x-axis represents time and the y-axis represents the pulse amplitude.	28
4.1	Detector 935-16B1R CAR depth distributions for various collimated depths. The same measurement time was used for each distribution. Because this detector has relatively low $\mu_h\tau_h$, the true depth has a one-to-one relationship with the CAR depth.	30
4.2	Depth calculated from the CAR parameter as a function of true depth for detectors 935-16B1R and 44B2L. Having relatively high $\mu_h\tau_h$, the slope approaches unity (from 0.84 to 0.95) and the offset approaches zero (1.2 to 0.64) for detector 44B2L as the cathode shaping time decreases. Data from the cathode side were not included in the linear fits due to the similarity in cathode pulse amplitudes for the collimator position at the cathode and the collimator position 0.635 mm away from the cathode. For comparison, the slope and offset for a detector with low $\mu_h\tau_h$ (935-16B1R) are 0.98 and 0.03 respectively. .	31
4.3	Graphical representation of the energy resolution as a function of the ingot location from which the detector originated. The x-axis represents the relative ingot location. Numerical values were assigned to the relative ingot location starting from the section A. The number labels indicate the number of zone refining passes.	33
4.4	(a) Detector 935-16B1R and (b) detector 935-16B1L pixel-by-pixel Cs^{137} depth-corrected spectra during the stable condition.	34
4.5	Pixel-by-pixel Cs^{137} energy-corrected spectra for detector 47AR(R) during the stable condition. Good spectroscopic performance is demonstrated in all pixels.	35
4.6	(a) Detector 70BA1R and (b) detector 70BA1L pixel-by-pixel Cs^{137} energy-corrected spectra during the stable condition.	36
4.7	Pixel-by-pixel Cs^{137} energy-corrected spectra for detector 44B2L during the stable condition. Good spectroscopic performance is demonstrated in all pixels.	37
4.8	(a)The energy resolution as a function of depth is relatively uniform for the best-performing pixels in detector 935-16B1R, indicating low electron trapping. (b) The weighting potential effect is apparent in the photopeak centroid channel as a function of depth plot, but there is little effect due to charge trapping. The CAR was overestimated in pixel 1 as a result of the signal crosstalk described in section 3.2.1.1.	39
4.9	(a)The energy resolution as a function of depth is relatively uniform for the best-performing pixels in detector 935-16B1L, indicating uniform electron trapping. (b) The weighting potential and uniform bulk trapping effect is apparent in the photopeak centroid channel as a function of depth plot. The CAR was overestimated in pixel 1 as a result of the signal crosstalk described in section 3.2.1.1.	40

4.10	(a)The energy resolution as a function of depth is relatively uniform for the best-performing pixels in detector 70BA1R, indicating low electron trapping. (b) The weighting potential effect is apparent in the photopeak centroid channel as a function of depth plot, but this detector is less affected by charge trapping than detector 935-16B1R.	41
4.11	(a) The energy resolution for detector 44B2L is overall worse than the other detectors; however, the energy resolution as a function of depth is relatively uniform. (b) The weighting potential as well as the effect from electron trapping is apparent in the photopeak centroid channel as a function of depth plot.	42
4.12	Detector 935-16B1R electron drift velocity calculated from Cs-137 photopeak events. The depth was calculated from the CAR, so the lack of data near the anode side is due to imperfect calculation of the CAR. The error bars represent experimental error, and the large error near the anode is due to poor counting statistics. The electron drift velocity is otherwise relatively uniform and approximately 10^5 cm/s in most depths.	43
4.13	Detector 935-16B1L electron drift velocity calculated from ^{137}Cs photopeak events. The depth was calculated from the CAR, so the lack of data near the anode side is due to imperfect calculation of the CAR. The error bars represent experimental error, and the large error near the anode is due to poor counting statistics. The electron drift velocity is otherwise relatively uniform and approximately 2×10^5 cm/s in most depths.	44
4.14	Detector 44B2L electron drift velocity calculated from Cs-137 photopeak events. The depth was calculated from the CAR, so the lack of data near the anode side is due to imperfect calculation of the CAR. Many depths have poor counting statistics, but the electron drift velocity in most depths is approximately 10^5 cm/s.	44
4.15	Detector 70BA1R electron drift velocity calculated from ^{241}Am alpha particle cathode-side irradiation. The electron drift velocity is uniform in most pixels except pixel (1,1) where the drift velocity at the anode side is more than double that of the cathode side.	45
4.16	Detector 70BA1L electron drift velocity calculated from ^{241}Am cathode-side irradiation. The drift velocity is not uniform with respect to detector depth; however, each pixel shares a similar drift velocity profile, having higher drift velocities near both electrodes.	45
4.17	Detector 47AR(R) electron drift velocity calculated from ^{241}Am cathode side irradiation. Similar to detector 70BA1R, the drift velocities are higher near both electrodes.	46
5.1	The overall corrected energy resolution improved significantly for detector 935-16B1R. Significant improvement was observed in all pixels.	49

5.2	(a) The signal amplitude and photopeak efficiency increased as detector 935-16B1R stabilized. (b) The photopeak is initially not present in most depths in pixel 8. Similar poor performance at depths away from the anode was observed in all pixels. Both measurement times are the same for comparison.	50
5.3	Event classification for the first 24-hour measurement and a 24-hour measurement after detector 935-16B1R stabilized shown together on the same plots. (a) As the signal gain increases, more events cross the trigger threshold and more events pass the amplitude threshold in post-processing. The fraction of single-pixel events increases from approximately 60% of the total events initially to approximately 70% of the total events as the fraction of multiple pixel events decreases from 35% to 25%. (b) The contribution of each pixel to single-pixel events becomes relatively constant and more uniform in the detector's stable state.	51
5.4	The overall corrected energy resolution was not measurable in the first measurement and improved significantly by the second measurement for detector 935-16B1L.	52
5.5	(a) The signal amplitude and photopeak efficiency increased as detector 935-16B1L stabilized. (b) The 3D spectrum for the best performing pixel, pixel 8, shows the spectrum changes most near the cathode side. Similar poor performance at depths away from the anode was observed in all pixels. Both measurement times are the same for comparison.	53
5.6	Event classification for the first 24-hour measurement and a 24-hour measurement after detector 935-16B1L stabilized shown together on the same plots. (a) Between the two measurements, the total number of events as well as the single-pixel events increase while the number of multiple pixel events decreases. (b) The contribution of each pixel to single-pixel events becomes relatively constant in the detector's stable state.	54
5.7	In the first measurement, the energy resolution was not measurable and improved significantly by the second measurement for detector 44B2L. Both measurement times are the same for comparison. . . .	55
5.8	(a) The signal amplitude and photopeak efficiency increased as detector 44B2L stabilized. (b) The photopeak is not initially present in most depths, but is clearly present in all depths after the detector stabilizes. Similar poor performance at depths away from the anode was observed in all pixels.	56

5.9	Event classification for the first 20-hour measurement and an 20-hour measurement after detector 44B2L stabilized. (a) The total events increased as the signal gain also increased. The fraction of single pixel events increased by approximately 15% of the total counts while the fraction of multiple pixel events decreased by approximately 15%. (b) The contribution of each pixel to processed single-pixel events becomes more uniform and constant, but shows less change during this transition phase than other detectors tested.	57
5.10	(a) The spectroscopic performance for detector 70BA1R did not show a significant change. (b) Because the spectroscopic performance was good in both measurements, the depth-dependent photopeak data are useful for comparison. The photopeak centroid increased slightly after the detector stabilized.	58
5.11	(a) The total counts and change in event classification for detector 70BA1R remained relatively constant after almost one month of normal operation. (b) The distribution of the single-pixel contribution by pixel also shows little change.	59
5.12	(a) Detector 70BA1R experienced a less drastic change in electron drift velocity than detector 70BA1L; however, the electron drift velocity also became more uniform as the detector stabilized. (b) The average drift velocity also increased similar to detector 70BA1L. . .	60
5.13	(a) The energy resolution improved on the best pixel and overall for detector 70BA1L, but the efficiency appears to degrade, possibly due to an accidental change in source geometry. (b) The photopeak centroid increased in every pixel between measurements.	61
5.14	(a) The total counts decreased in the later measurement for detector 70BA1L. The instability is likely due to changes in the electronic noise during the measurement. (b) The distribution of the single-pixel event contribution by pixel also shows pixel 8 received a large portion of the counts during the unstable period.	62
5.15	(a) Weaker drift velocity is initially observed in the central depths of detector 70BA1L. During the conditioning phase, the drift velocity increases in the central depths and eventually becomes more uniform over all depths. (b) The average drift velocity increases as the detector stabilizes.	63
5.16	(a) The spectrum characteristics remained relatively constant for detector 47AR(R). The overall corrected energy resolution degraded slightly from 1.75% to 1.89% FWHM at 662 keV. (b) The drift velocity remained relatively uniform throughout the duration of the measurement.	64
5.17	Charge density as a function of detector depth for detectors (a) 70BA1L and (b) 70BA1R. The y-axis represents electrons per unit volume such that positive values represent negative charge. As the detectors stabilize, negative charge becomes more concentrated at the electrodes.	66

6.1	Depth-corrected Cs ¹³⁷ spectra for the first hour of room temperature operation compared to hours 20 and 24. Data measured at -20°C prior to the room temperature measurement were used to calibrate these data.	70
6.2	Total counts as a function of depth for the first hour of room temperature operation compared to hours 20 and 24. Data measured at -20°C prior to the room temperature measurement were used to calibrate these data.	70
6.3	Change in event classification as a function of time for detector 70BA1R.	71
6.4	Drift velocity as a function of depth calculated from ²⁴¹ Am alpha particle waveforms. The drift velocity uniformly decreases in most depths as the detector polarizes. The drift velocity increases near the anode side as the detector polarizes, possibly indicating a build up of bromine vacancies. Due to geometric constraints, pixels 1, 2, 4, and 5 are the only pixels with statistically significant alpha data.	71
6.5	The drift velocity was averaged over all depths at each measurement time for detector 70BA1R. The average drift velocity decreased by approximately 10% from the beginning of the room temperature measurement as the detector polarized.	72
6.6	Three standard deviations of the charge arrival position calculated from cathode-side alpha events for detector 70BA1R, which includes 97% of the total charge cloud.	72
6.7	Drift velocity as a function of depth calculated from ²⁴¹ Am alpha particle waveforms for detector 70BA1L. The drift velocity uniformly decreases in most depths as the detector polarizes. The drift velocity gradually decreases near the anode side as it increases near the cathode side. The central pixel became count starved as the detector failed.	73
6.8	The drift velocity was averaged over all depths at each measurement time for detector 70BA1L. The overall average drift velocity initially increases in most pixels (as much as 10% in Pixel 1), and remains relatively constant throughout remainder of the measurement. . . .	74
6.9	Change in event classification as a function of time for detector 70BA1L.	74
6.10	(a) Detector 47AR(R) depth-corrected spectra for the initial 24-hour measurement compared to the last 24-hour measurement. (b) The gain decreases slightly in the raw spectrum between the first and the last 24-hour measurements.	77
6.11	(a) The photopeak position decreases uniformly in pixels where the photopeak is still present. (b) The peak counts also decrease nearly uniformly in all depths except very near the cathode of every pixel.	78
6.12	The energy-corrected photopeak position is plotted as a function of time with the 87 measurement days separated into 100 bins. The photopeak position decreased by approximately 5 keV (1%) after two weeks of room-temperature operation and remained relatively stable in the pixels with a detectable photopeak.	79

6.13	The alpha peak centroids in the (a) cathode spectrum and (b) anode spectrum similar trend with the peak position decreasing by approximately 50% by the end of the measurement.	80
6.14	Initial and final three-dimensional spectra for all nine pixels. The pixels are shown in ascending order with figure (a) corresponding to pixel 1. These data show performance degradation occurring at all depths.	83
6.15	(a) Detector 47AR(R) drift velocity as a function of depth calculated from ^{241}Am alpha particle waveforms and (b) the overall average drift velocity as a function of time. Because the average drift velocity would be overestimated, the average drift velocity plot is a conservative estimate.	84
6.16	Event classification for the first 48 hour-measurement compared to the last 48 hours on the same plot for detector 47AR(R).	85
6.17	Optical microscope images of the anode of detectors 70BA1R after failure. The top row and left column of pixels comprise the guard ring, and the anode pixels are oriented such that pixels 1, 2, and 3 are in the top row. Any physical damage to the contact is not visually obvious.	86
6.18	Optical microscope images of the anode of detectors 70BA1L after failure. The bottom row and right column of pixels are connected and serve as a guard ring. The anode pixels are oriented such that pixels 1, 2, and 3 are in the top row. Large portions of the gold contact are missing in this detector	86
6.19	Optical microscope images of the anode of detectors 47AR(R) after failure. The bottom row and right column of pixels are connected and serve as a guard ring, and the anode pixels are oriented such that pixels 1, 2, and 3 are in the top row. Pixels 7, 8, and 9 suffered the most damage and also demonstrated the worst spectroscopic performance.	87
7.1	(a) Detector Cinn1 was fabricated from naturally occurring cinnabar and was 0.55 mm thick. The black dot is a conductive carbon paste used to make the 1-mm diameter electrodes. (b) Detector Cinn1 response to ^{137}Cs compared to a measurement with no source present. Both spectra were measured in 30 minutes at -300 V with a 2 μs shaping time.	89
7.2	(a) Detector HgS-1 was fabricated from naturally occurring cinnabar and was 0.5 mm thick. Gold was evaporated onto the surfaces to create 1.1-mm diameter electrodes. (b) Detector HgS-1 response to ^{137}Cs compared to a measurement with no source present. Both spectra were measured in 4 hours at -500 V with a 1 μs shaping time.	90

7.3	(a) ^{137}Cs spectra taken at the bias voltages used to calculate the electron mobility-lifetime product from equation 7.5. (b) The measured induced charge and the predicted induced charge calculated from a nonlinear least squares fit of equation 2.3 to the data while varying $\mu_e\tau_e$ and eN_o . The corresponding spectra are not shown in (a) for visual purposes.	91
7.4	(a) The crystal as it was received from the rock shop. (b) The resulting detector.	93
7.5	Single crystal and powder XRD spectra for the HgS detector fabrication at the University of Michigan. The powder diffraction spectrum reveals there are no contaminants. The single crystal diffraction spectrum indicates that this is a single crystal.	93
7.6	(a) The orientation of the crystal lattice. Additional aspects of the lattice are shown in (b) and (c). In all of these images, mercury atoms are visualized with large spheres, and the sulfur atoms are the smaller spheres.	94
7.7	Measurement setup for HgS and HgO experiments. The preamplifier signals were connected to a Canberra model 2026 amplifier. The amplified signals were connected to an Ortec multichannel analyzer with 2048 channels.	95
7.8	An ^{241}Am alpha spectrum measured for 22 hours compared with a background spectrum measured for 16 hours with -200 V applied bias. The shaping time was 12 μs , and the same gain setting was used for both measurements.	95
7.9	^{57}Co spectrum measured for 20 minutes compared to a spectrum measured for 16 hours using -200 V bias. A 2 μs shaping time was used for each measurement. Due to a lower signal amplitudes from the gamma rays, a higher gain setting was used for these measurements than what was used for the alpha measurement.	96
7.10	^{137}Cs spectra measured for 20 minutes at different operating voltages. A 2 μs shaping time was used for each measurement. The same shaping time and gain setting were used for the ^{137}Cs and ^{57}Co measurements.	96
7.11	(a) Keithley 4200 semiconductor characterization system and (b) the Alessi probe station used to measure HgS I-V characteristics. The device being tested was placed on the probe station stage, and the probes were put in contact with the electrodes. Then the probe station is connected to the Keithley which controls the voltage and measures the characteristics.	97
7.12	The I-V curve was generated by changing the voltage from zero to ten volts then from ten to zero volts in 0.5 V increments with no delay between measurements. The I-V curve for negative voltages was generated in the same way. The estimated resistivity from these data is $10^{11} \Omega\text{-cm}$	97

7.13	The I-V curve was generated by changing the voltage from zero to ten volts then from ten to zero volts in 0.5 V increments with no delay between measurements. The I-V curve for negative voltages was generated in the same way. The linearity of the I-V curve indicates the HgO detector is Ohmic. The resistivity was estimated from the slope of this curve to be $5\text{E}9\ \Omega\text{-cm}$ and is reported in table 7.1. . . .	98
7.14	HgO response to a $0.1\ \mu\text{Ci}\ ^{241}\text{Am}$ alpha source measured for one hour and a $100\ \mu\text{Ci}\ ^{137}\text{Cs}$ source measured for two hours. A two-hour background measurement yielded zero counts and is not shown on the plot. The spectra were measured at an operating voltage of -350 V using a $12\ \mu\text{s}$ shaping time. The detector is 0.5 mm thick with 0.6 mm diameter carbon paste electrodes	98

LIST OF TABLES

Table

1.1	Properties of Semiconductor Materials	2
3.1	TlBr Detector Fabrication Parameters	19
4.1	TlBr Spectroscopic Performance [1, 2]	33
7.1	Properties of Semiconductor Materials	88
7.2	Calculated $\mu_e\tau_e$ Values for Detector HgS-1	91

ABSTRACT

Alternative Wide-Band-Gap Materials for Gamma-Ray Spectroscopy

by

Crystal Thrall

Chair: Zhong He

Thallium-bromide (TlBr), mercury-sulfide (HgS), and mercury-oxide (HgO) detectors have been investigated as room-temperature or close-to-ambient-temperature operational semiconductor gamma-ray spectrometers. The three-dimensional position-sensitive single-polarity charge sensing technique, successfully used on CdZnTe gamma-ray imaging spectrometers, has been applied to 5-mm thick TlBr detectors and has resulted in energy resolutions as good as 0.73% FWHM and 0.97% FWHM at 662 keV on the best anode pixel and from all nine pixelated anodes respectively. Furthermore, three-dimensional position-sensing readout technology enabled characterization of both initial transient behavior and room-temperature failure behavior as a function of three-dimensional location within the TlBr detector material. Cathode-side alpha-particle irradiation also enabled the study of the electron drift velocity as a function of detector depth during both initial and room-temperature transient phases. This work presents the latest spectroscopic performance, characteristic initial transient behavior observed at -20°C , and room-temperature failure behavior on a number of 5-mm thick TlBr detectors manufactured by Radiation Monitoring Devices. Experimental

results suggest uniform stable performance may be achieved through improved surface preparation and contact fabrication. This work also presents preliminary radiation and electronic response results for HgS and HgO detectors.

CHAPTER I

Introduction

1.1 Motivation for Thallium-bromide Development

Gamma-ray spectroscopy is required for many industrial, medical, science, and homeland security applications. Currently, high purity germanium (HPGe) detectors offer superior spectroscopic performance, but necessary cryogenic cooling presents challenges for practical use. Having low thermally generated charge carrier concentrations, wide-bandgap semiconductors allow for room-temperature operation. Of the available room-temperature semiconductor gamma-ray detector technologies (e.g. CdZnTe (CZT), CdTe, and HgI₂), CZT is spectroscopically the closest competitor to HPGe, achieving energy resolution as good as 0.48% FWHM at 662 keV [3].

Table 1.1 compares the properties of these traditional materials to those of thallium-bromide (TlBr), which has recently become a possible alternative material for room-temperature semiconductor gamma-ray detectors. Having a higher atomic number and density, TlBr has greater gamma-ray detection efficiency, and its wide bandgap permits low-noise operation at room temperature. Furthermore, because it has only one solid phase, a simple interpenetrating primitive cubic crystal structure (also known as the cesium-chloride structure), and a relatively low melting point (480 °C), TlBr is ideal for melt growth, a relatively easy growth and purification process.

Table 1.1: Properties of Semiconductor Materials

Material	Atomic Number	Density (g/cm ³)	Band Gap (eV)	Ionization Energy (eV/e-h pair)	Resistivity Ω -cm
Ge	32	5.33	0.72	3.61	
HgI ₂	80,53	6.4	2.13	4.2	10 ¹² -10 ¹³ [4]
CdTe	48, 52	6.1	1.5	4.4	10 ⁸ -10 ⁹ [5]
CdZnTe	48, 30, 52	6.1	1.7	4.7	10 ¹⁰ -10 ¹¹ [6]
TlBr	81, 35	7.6	2.7	6.5	10 ¹¹ [7]

1.2 The Evolution of Thallium-bromide and its Current Challenges

Robert Hofstadter introduced thallous-halides as potential materials for radiation detection in 1947 [8]. In the 1980s, Ur-Rahman *et al.* observed the motion of both holes and electrons in TlBr crystals at low temperatures (around -90°C), but material quality limited the electron mobility-lifetime product ($\mu_e\tau_e$) to $10^{-8} \text{ cm}^2/\text{V}$ [9]. Subsequent research by Shah *et al.* showed that both holes and electrons were mobile near room temperature; however, charge carrier trapping due to crystal impurities and defects limited detector performance [10]. In the early 1990s, Shah *et al.* fabricated 0.1-mm-thick planar detectors that achieved $\mu_e\tau_e$ on the order of $10^{-5} \text{ cm}^2/\text{V}$ and hole mobility-lifetime products ($\mu_h\tau_h$) on the order of $10^{-6} \text{ cm}^2/\text{V}$ from 99.9999% pure TlBr powder, which they further purified through multiple-pass zone refining in a two-zone horizontal furnace [11, 12].

In the late 1990s and early 2000s, researchers gained further charge transport improvement by growing crystals via the horizontal traveling molten zone method, which resulted in larger detectors [13, 14, 15, 16, 17]. Better crystal growing techniques lead to fabricating single-polarity charge sensing devices via pixellated anodes [18, 19, 20]. Researchers gradually improved the crystal quality and detector fabrication, which lead to better spectroscopic performance [21, 22, 23, 24]. Given the improvement in charge transport properties, researchers have been attempting to grow larger single

crystals [25, 26, 27, 28] with the largest device fabricated being 10 mm x 8 mm x 18 mm [29].

These recent developments indicate that TlBr is a very promising material for room-temperature gamma-ray detection and measurements. However, performance degradation and eventually complete irreversible failure while under bias complicates room-temperature operation for practical applications. It is believed that ionic conduction within the lattice is the root cause of this so-called polarization phenomenon [30]. In order to avoid polarization, TlBr detectors must be cooled to suppress the ionic conductivity [31]. TlBr detectors can achieve long-term stability at -20°C [32, 33], and work has been ongoing toward characterizing and improving the stability and performance at room temperature.

A popular theory suggests that lattice ions migrate and build up at the electrodes, creating an internal electric field opposite the applied bias. As a result, charge carrier creation and collection efficiency decreases. By applying thallium electrodes, Hitomi *et. al.* were able to achieve 30 hours of stable operation at room temperature [34]. Further experiments with thallium electrodes showed that TlBr detectors could achieve stable room-temperature operation for up to 600 hours by periodically switching the bias direction [35, 36]. Hitomi hypothesized that thallium electrodes suppress accumulated Tl^{+} and Br^{-} ions under the cathode and anode through favorable chemical reactions [34, 35, 36, 37]. While thallium electrodes are a possible solution for stable room-temperature operation, thallium metal is highly toxic and thus not ideal. Furthermore, periodically reversing the bias is not conducive to single-polarity charge sensing device configurations (i.e. pixellated or coplanar grid devices).

Voss and Conway *et. al.* hypothesized that chemical reactions rather than accumulating ions at the electrodes caused room-temperature failure and sought a solution through surface preparation improvement [38, 39]. Supposedly, bromine ions may react chemically with gold to create a gold-bromine compound as well as more

bromine vacancies. Chemically etching the TlBr surface with hydrofluoric (HF) or hydrochloric (HCl) acid creates either TlBrF or TlBrCl heterojunctions which have larger bandgaps than TlBr [40]. Therefore, electronic injection and chemical reactions at the contact were suppressed. Alternatively, a bromine-methanol chemical etch* removes the polishing damage layer without creating an electronic barrier. As a result, bromine vacancies accumulate at the surface and reduce the electronic injection barrier.

1.3 Contribution of This Work

In principle, the current CZT technology [3, 41, 42] can simply be applied to TlBr; however, the material has unique characteristics which require further study and understanding. The work presented in this dissertation furthers the understanding of the unique physical processes that occur during operation at -20°C as well as room temperature. Chapter V characterizes the initial transient behavior experienced by TlBr detectors prior to stable operation. Once stability is achieved, good depth and energy resolution can be expected from TlBr detectors, which is described in Chapter IV. Chapter IV also describes how single-polarity charge sensing techniques are complicated in TlBr detectors with relatively high hole mobility-lifetime products.

A practical solution for room-temperature operation has yet to be implemented, but TlBr continues to be a promising material for room-temperature gamma-ray detection and measurements. Chapter VI characterizes the failure process using both alpha particle and gamma ray data. Chapter VIII summarizes the results of this work and describes future work that will possibly lead to the development of a commercialized TlBr-based room-temperature radiation sensor.

*The standard detector fabrication process at RMD, Inc. includes bromine-methanol chemical etch, described in section 3.1.

CHAPTER II

Theory

2.1 Signal Generation and the Shockley-Ramo Theorem

The Shockley-Ramo theorem [43] is a key principle to the operation of various radiation detector types, including pixelated semiconductors such as the TlBr detectors studied in this work. When radiation deposits energy in a semiconductor, electron-hole pairs are generated. In order to calculate the charge induced on the electrodes without the Shockley-Ramo theorem, one must first calculate the electric field along the track of a moving charge then integrate the normal component of the electric field over the electrode surface.

In order to avoid such cumbersome calculations, Ramo and Shockley independently formed a simpler method to calculate the induced charge. The theorem states that the instantaneous current i induced on an electrode is given by the dot product of the velocity v of charge carrier q and the weighting field E_w , shown in equation 2.1.

$$i = q\vec{v} \cdot \vec{E}_w \quad (2.1)$$

Equivalently, the change in weighting potential ϕ as a point charge q moves from position x_0 to x_f , is directly proportional to the induced charge Q , described by

equation 2.2.

$$Q = q[\phi(x_f) - \phi(x_0)] \quad (2.2)$$

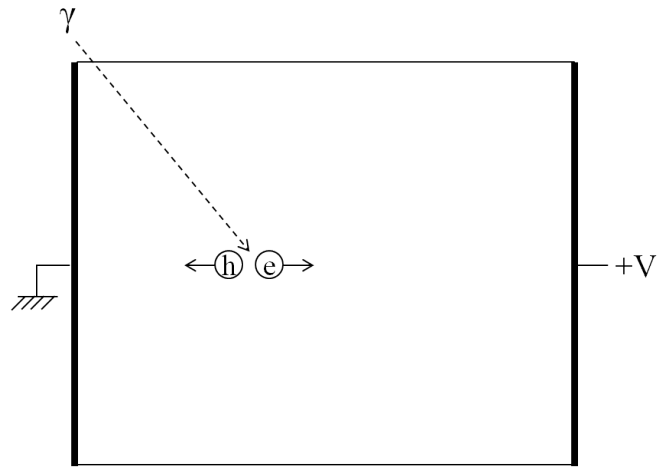
Unlike electric potential, the weighting potential depends only on the detector geometry and is therefore constant and unique for each electrode. For a given electrode, the weighting potential is the electric potential that would exist at a position in a particular detector under the following conditions:

1. The selected electrode is set to unit potential.
2. All other electrodes are set to zero potential.
3. All space charge is removed.

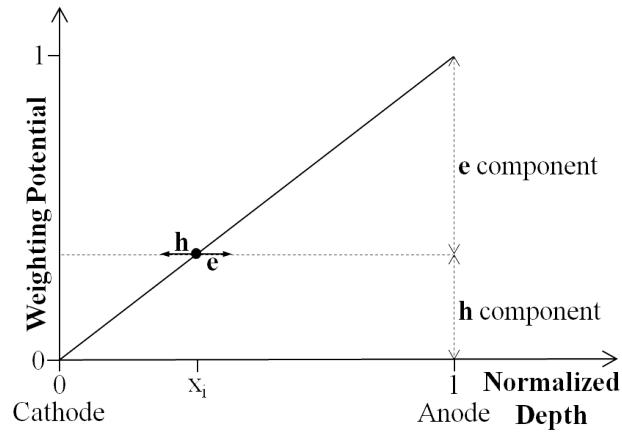
For a detector with planar electrodes, the weighting potential is linear as shown in figure 2.1. In the absence of charge trapping, the signal amplitude would be the same regardless of interaction depth. Therefore the energy resolution of a planar detector would be limited only by electronic noise and charge carrier statistics, and each gamma-ray energy would correspond uniquely to a specific signal amplitude. In reality, semiconductors suffer from trapping of both electrons and holes, and the total induced charge Q is described by the Hecht relation [44]:

$$Q = eN_0 \left\{ \frac{\nu_h \tau_h}{W} \left(1 - \exp \left[\frac{-x_i}{\nu_h \tau_h} \right] \right) + \frac{\nu_e \tau_e}{W} \left(1 - \exp \left[\frac{x_i - W}{\nu_e \tau_e} \right] \right) \right\} \quad (2.3)$$

where e is the electronic charge, N_0 is the number of charge carriers, ν is the charge carrier velocity, τ is the charge carrier lifetime, x_i is the radiation interaction location measured from the cathode, W is the detector thickness, and the subscripts e and h represent electrons and holes respectively. It is clear from equation 2.3 that total induced charge depends on the interaction depth, which limits the practical use of



(a)



(b)

Figure 2.1: (a) The geometry of a semiconductor detector with planar electrodes. (b) The anode weighting potential as a function of normalized detector depth for a planar detector. The motion of both electrons and holes contribute to the signal.

planar devices. Fortunately, a combination of technologies have been invented that circumvent the charge carrier trapping problem.

Because the transport properties of electrons are generally significantly better than those of holes, techniques were developed such that full-amplitude signals depend only on electron collection [45]. Single-polarity charge sensing may be achieved simply by optimizing the anode geometry such that the weighting potential is zero at all depths except those very near the anode. The concept is similar to that of a Frisch grid for gas and liquid ionization detectors, the first single-polarity charge sensing technique [46, 47]. Placing a Frisch grid in close proximity to the anode at an intermediate potential between the anode and cathode creates a weighting potential shown in figure 2.2. The grid shields the movement of charge carriers at distances between the cathode and the grid; therefore, only the motion of electrons between the grid and the anode contribute to the signal.

There are a number of single-polarity charge sensing technologies for semiconductors [43], but the detectors tested in this work utilized a pixelated anode and planar cathode configuration illustrated in figure 2.3(a). Similar to the Frisch grid technique, a pixelated electrode achieves single-polarity charge sensing by optimizing the weighting potential [48]. Applying the Shockley-Ramo theorem, anode pixel weighting potentials are calculated by setting the pixel of interest to unit potential and all other electrodes to zero potential.

Figure 2.3(b) shows the anode pixel weighting potential for a typical TlBr detector* is near zero at most depths and dramatically increases one pixel pitch from the anode. As a result, anode output signals depend mostly on the movement of electrons. In the absence of electron trapping, each deposited energy would correspond uniquely to an output signal amplitude at each depth of interaction. Charge transport is never perfect in reality, and the depth-dependent cathode signal becomes

*Details of a typical TlBr detector are described in Chapter III.

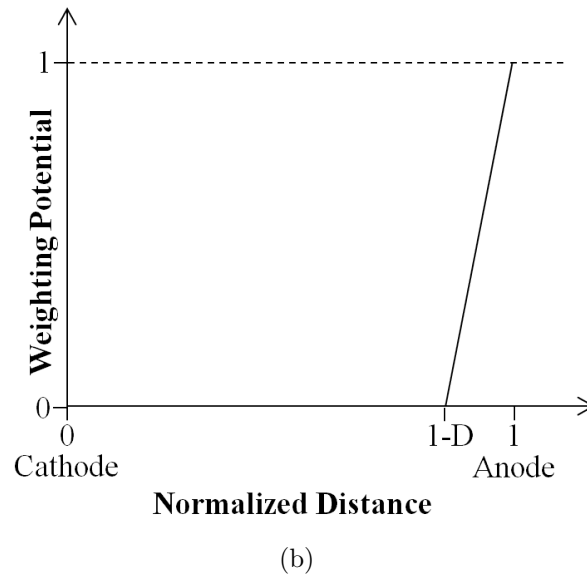
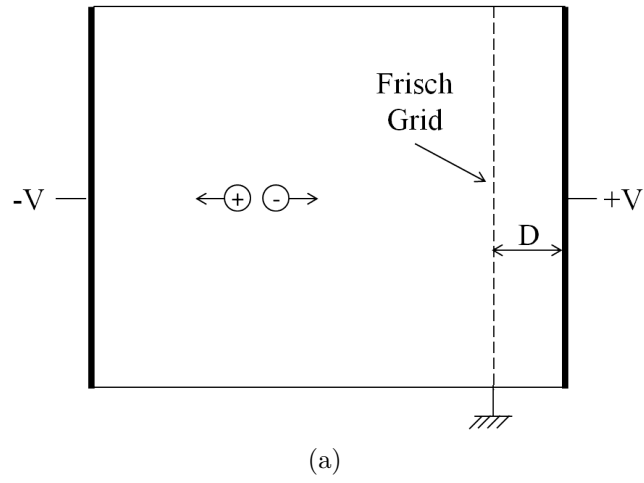


Figure 2.2: (a) The geometry of an ionization chamber with a Frisch Grid. (b) The anode weighting potential as a function of distance. The weighting potential is zero except near the anode.

useful in correcting for weighting potential and charge trapping effects.

2.2 Depth Sensing and Energy Correction

Because the cathode signal Q_C has a linear dependence with the detector depth Z , and the anode signal Q_A depends mostly on the number of charge carriers N and the electronic charge e_0 , the ratio of the cathode signal to the anode signal is a linear function of the depth, as shown in equations 2.4, 2.5, and 2.6.

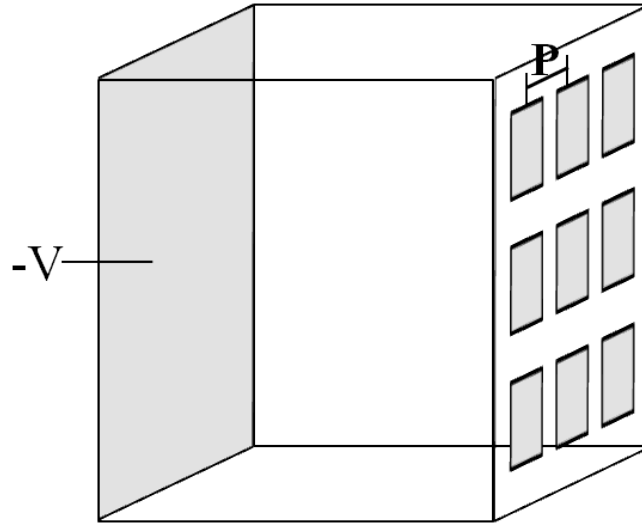
$$Q_C = Ne_0[\phi_f - \phi_i] = Ne_0Z \cdot G_C \quad (2.4)$$

$$Q_A = Ne_0[\phi_f - \phi_i] \approx Ne_0 \cdot G_A \quad (2.5)$$

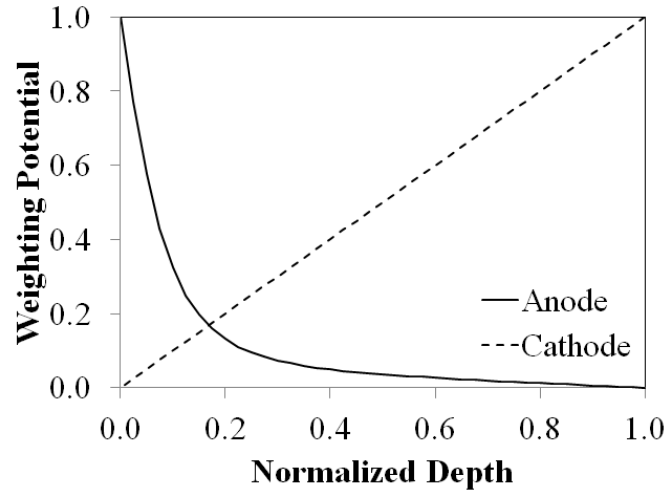
$$\frac{Q_C}{Q_A} = \frac{Ne_0Z}{Ne_0} = A \cdot Z \quad (2.6)$$

Knowing the depth of interaction, a gamma-ray energy spectrum can be binned as a function of cathode-to-anode-ratio (CAR) depth. After binning, the photopeaks of a calibration gamma ray source, such as cesium-137 (^{137}Cs), can be aligned by applying a gain factor to each depth to generate a depth-corrected spectrum [49, 50].

While depth-correction works well for detectors with relatively immobile holes, the CAR can be overestimated in a detector having high $\mu_h\tau_h$ relative to its $\mu_e\tau_e$ (with $\mu_h\tau_h$ reported as high as 20% of $\mu_e\tau_e$ [17]). Relatively mobile holes contribute to the slow rise in the cathode waveforms, shown in figure 2.4. As a result, a fixed cathode shaping time will overestimate the cathode signal amplitude at most depths which distorts the CAR depth-based energy correction. To overcome this problem, the energy correction can be calculated based on the electron drift time rather than the CAR.



(a)



(b)

Figure 2.3: (a) The geometry of semiconductor detector with a pixelated anode and planar cathode. The P represents the pixel-to-pixel pitch. (b) The anode and cathode weighting potentials as a function of detector depth. The anode weighting potential was calculated for the center of the central pixel for a typical TlBr detector.

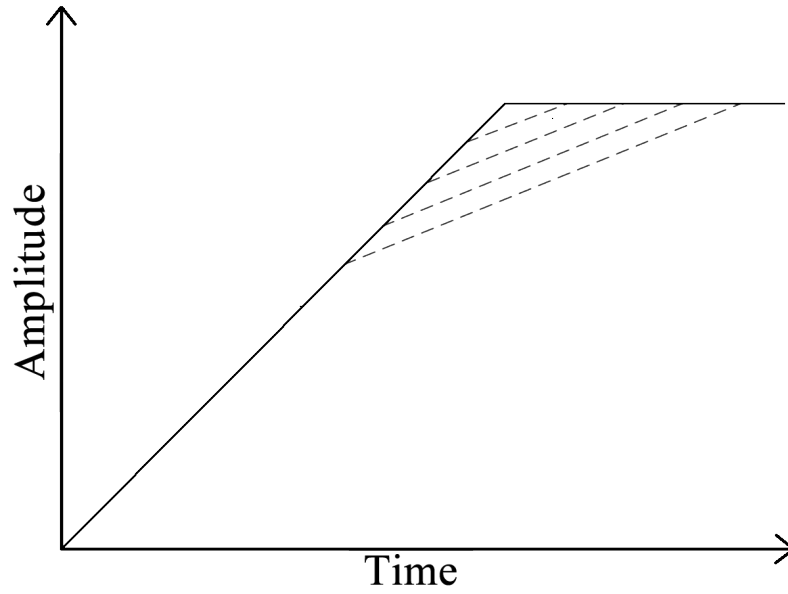


Figure 2.4: Example cathode waveforms illustrating measurable hole movement. The solid line illustrates a cathode-side event with only electrons contributing to the signal. The dashed lines indicate the hole component of the cathode signal for interactions occurring at various detector depths. By using a shaping time long enough to eliminate ballistic deficit in the electron component, the measured cathode signal amplitude loses its depth dependence.

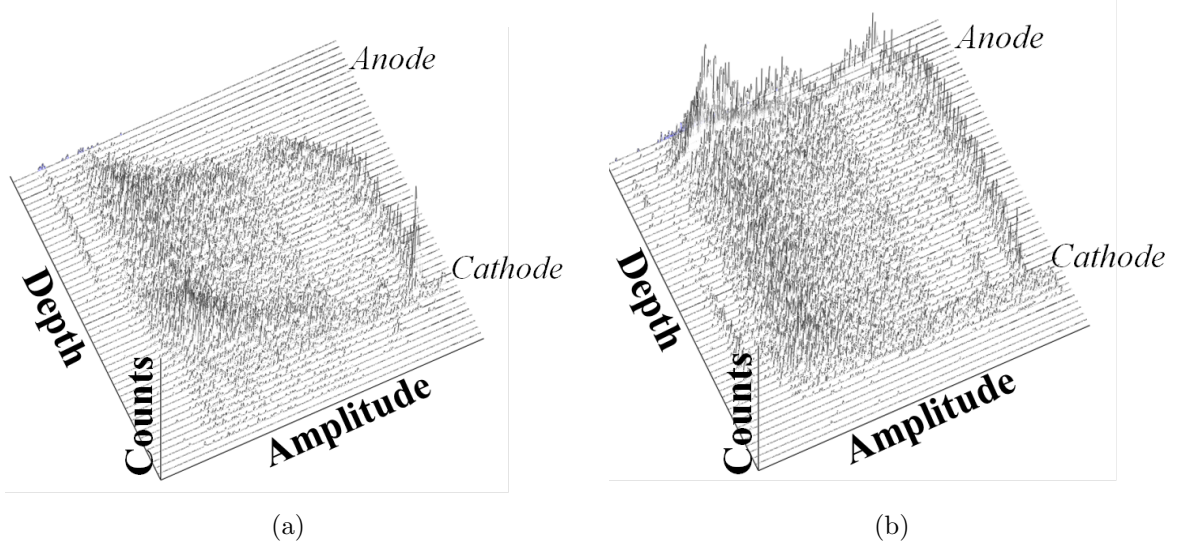


Figure 2.5: (a) An example of a depth-separated spectrum for a detector with high $\mu_h\tau_h$ such that the CAR is overestimated. (b) The same spectrum separated by time.

Similar to the CAR, each depth corresponds uniquely to an electron drift time. In figure 2.5(a), the depth-separated spectrum is shifted such that there are very few counts near the anode. The time-separated spectrum in figure 2.5(b) shows a more uniform count distribution from the anode to the cathode and the weighting potential change starts closer to the anode as expected. The drift time may not be linearly proportional to true depth; however, each depth has a unique drift time and may be used to generate energy-corrected spectra.

2.3 Material Properties

Depth information provides insight into the material properties of a detector [51, 52, 53, 54, 55]. For example, the energy resolution and photopeak centroid channels as functions of depth reveal trapping behavior within a device [56]. Uniformity in the energy resolution at each depth indicates uniform material, i.e. no concentration of trapping centers, whereas poor electron transport would cause increasing energy resolution degradation from the anode side to the cathode side. The photopeak

centroid is affected by both weighting potential and charge trapping. In the absence of electron trapping, the photopeak centroid amplitude would remain uniform at most depths and decrease near the anode side as a result of the weighting potential. Assuming uniform bulk trapping, the photopeak centroid amplitude should increase as a function of depth from the cathode side to the anode side. A trapping center at a given depth would cause a sharp decrease in photopeak centroid and energy resolution degradation at that depth.

Depth-dependent photopeak electron drift time data may also be used to calculate the electron drift velocity as a function of depth. Charge carrier mobility μ changes as a function of temperature and impurity concentration [57], so assuming these parameters are constant for each detector, the electron drift velocity v reflects the behavior of the electric field E through the relationship in equation 2.7.

$$\vec{v} = \mu \vec{E} \tag{2.7}$$

2.4 Ionic Conduction

Ionic conduction in solid state materials, also known as solid electrolytes, may be desirable for various applications such as batteries and chemical sensors [58]. However, ionic conduction may be inconvenient for room-temperature semiconductor gamma-ray measurement applications. To understand why ionic conduction is problematic, it is first necessary to understand the physical processes that cause ionic conduction in ionic crystals such as TlBr.

At any finite temperature, the probability of defect formation inside a crystal lattice is nonzero [59]. The Helmholtz free energy function, which applies to closed thermodynamic systems, states that if the system is at a constant pressure then,

$$G = H - TS \tag{2.8}$$

where T is the temperature and H is the total enthalpy of the total atoms comprising the system. The entropy, S , of the system is characterized by

$$S = k_B \ln w \quad (2.9)$$

where k_B is Boltzmann's constant and w is the number of possible configurations of atoms. As a result, the concentration of vacancies, C_v , and interstitials, C_i , is given by equations 2.10 and 2.11 respectively, where E_f is the formation energy of the specific defect and S_f is the change in total entropy as a result of the specific defect.

$$C_v = \exp\left(\frac{S_f^v}{k_B}\right) \exp\left(\frac{-E_f^v}{k_B T}\right) \quad (2.10)$$

$$C_i = \exp\left(\frac{S_f^i}{k_B}\right) \exp\left(\frac{-E_f^i}{k_B T}\right) \quad (2.11)$$

The ions that compose an ionic crystal lattice may conduct through the lattice generally by way of vacancy or interstitial migration [60, 61]. Vacancy migration occurs as a result of either thermally generated Schottky defect formation or the presence of charged impurities. An ion adjacent to a vacancy may leave its site for the neighboring vacancy, leaving a new vacancy behind that another ion may potentially fill. This effect is illustrated in figure 2.6(a). On the other hand, interstitial migration occurs when ions in interstitial sites move to adjacent interstitial sites as illustrated in figure 2.6(b).

The total electrical conductivity of a crystal, σ_T , is given by equation 2.12 where z_i is the charge number, e is the elementary charge, $[i]$ is the concentration, and μ_i is the mobility of the charge carrier i [62].

$$\sigma_T = \sum_i |z_i| e [i] \mu_i \quad (2.12)$$

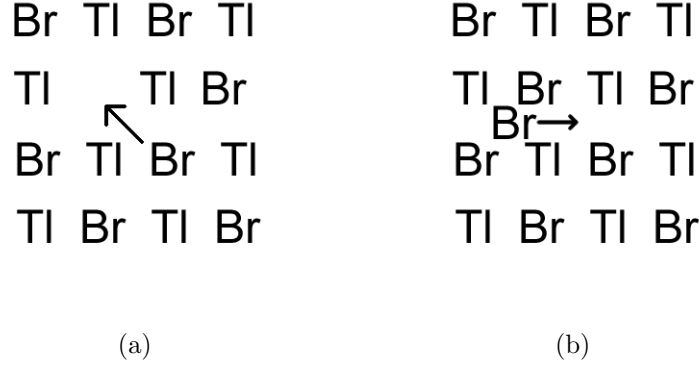


Figure 2.6: (a) Illustration of ionic conduction via vacancy migration. Analogous to hole conduction, vacancies conduct as ions vacate their lattice positions to nearby vacancies. (b) Illustration of ionic conduction via interstitial migration.

The intrinsic defects that predominantly occur in TlBr are Schottky type, which form thallium and bromine vacancies [63]. The mobility of each of these defects is given by equation 2.13 where μ_0 is a pre-exponential factor and H_m is the migration energy.

$$\mu_i = \frac{\mu_{0,i}}{T} \exp \left(-\frac{H_{m,i}}{k_B T} \right) \quad (2.13)$$

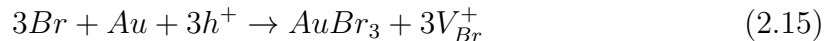
Assuming the contribution of thermally generated charge carriers is negligible, the total conductivity is given by equation 2.14 [64].

$$\sigma_T = q [V_{Tl}] \frac{\mu_{0,Tl}}{T} \exp \left(\frac{-H_{m,Tl}}{k_B T} \right) + q [V_{Br}] \frac{\mu_{0,Br}}{T} \exp \left(\frac{-H_{m,Br}}{k_B T} \right) \quad (2.14)$$

Due to its lower migration energy, bromine vacancies are significantly more mobile than thallium vacancies and therefore dominate the ionic component of the conductivity [31, 62, 63, 65, 66]. As the bromine concentration increases at the anode electrode, a chemical reaction may occur depending on the surface preparation and electrode material [40, 67].

As a result of the chemical reaction in equation 2.15, a 2.08 eV sub-bandgap transi-

tion forms during room-temperature operation in TlBr detectors with gold electrodes[†] [40].



These researchers experimented with other metals and achieved the longest stability with a platinum anode and nickel cathode. Other various combinations of metals such as nickel on both electrodes or silver on both electrodes resulted in worse performance than gold electrodes, presumably due to the occurrence of different chemical reactions. The results presented in Chapter VI agree with this hypothesis that the failure mechanism occurs at the contacts and shows evidence that a chemical reaction occurred during the room temperature failure process.

[†]RMD fabricates most TlBr detectors with gold electrodes which is discussed in Chapter III.

CHAPTER III

Detector Fabrication, Experimental Setup, and Methods

3.1 TlBr Detector Fabrication and Design

Detectors tested in this work were manufactured by Radiation Monitoring Devices, Inc (RMD). and each was created using similar methods [26]. The crystals were grown via the traveling molten zone method, and multiple pass zone refining was implemented for further purification. After crystal growth and purification, the samples were cut then lapped with 16 μm grain lapping paper and cleaned with an ultrasonic cleaner before polishing. The samples were polished with 3 μm grain Al_2O_3 paper. Once again, an ultrasonic cleaner removed any residual particles from the samples before proceeding. Next, the samples were chemically etched in a solution of 5% bromine in methanol for 20 seconds. After the sample was completely dried with nitrogen gas, an evaporator was used to apply the metal electrodes through a shadow mask. Most electrodes have a 20 nm thick layer of chromium followed by an 80 nm thick layer of gold. Table 3.1 summarizes the fabrication parameters for each detector, and figure 3.1 describes the nomenclature for the detectors in table 3.1.

Every detector was approximately 5 mm x 5 mm x 5 mm with a planar cathode and a pixelated anode. Fine palladium wires were attached to the electrodes with a

Table 3.1: TlBr Detector Fabrication Parameters

Detector	Start Material	Number of Zone Refining Passes	Growth Rate (mm/h)	Contacts	Thickness (mm)
935-16B1R	RAP purified	100	2.5	Cr/Au	5.2
935-16B1L	RAP purified	100	2.5	Cr/Au	5.1
44B2L	Sublimed	99	2.5	Cr/Au	5.48
48A2R	Sublimed	99	2.5	Cr/Au	5.1
58A4L	RAP purified	101	2.5	Cr/Au	5.37
58A3R	RAP purified	101	2.5	Cr/Au	5.14
70BA1L	No purification	300	2.5	Cr/Au	5.22
70BA1R	No purification	300	2.5	Cr/Au, Cr	5
61A2L	No purification	100	2.5	Cr	5.34
47AR	No purification	200	2.5	Cr/Au	7.53
47AR(R)	No purification	200	2.5	Cr/Au	6.38
48A3L	No purification	200	2.5	Cr/Au	4.94
43A4(R)	Sublimed	48	5	Cr/Au	4.3
44A12R(R)	Sublimed	99	2.5	Cr, Cr	4.3
70BA2R(RR)	No purification	300	2.5	Cr, Cr	3.7

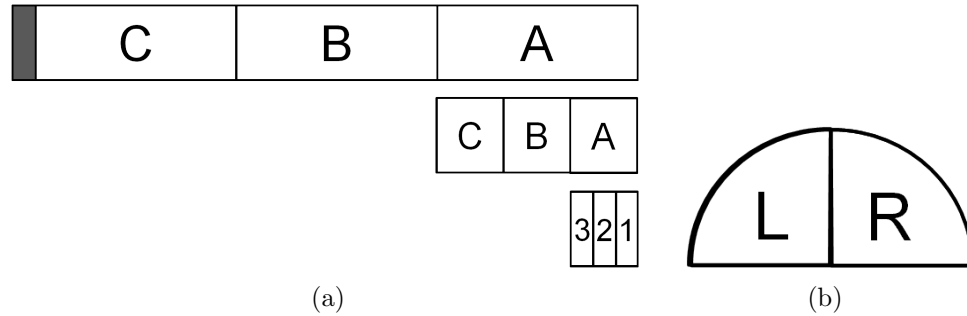


Figure 3.1: (a) Graphical representation of a typical TlBr ingot. The heater ring moves from right to left, therefore the impurity concentration increases from right to left. The ingot is divided into three sections and given a letter designation. Each section is further subdivided as shown in the figure. The dark area represents the unusable end of the ingot where most of the impurities reside at the end of crystal growth and purification. (b) A cross-sectional representation of a typical TlBr ingot. The L and R at the end of the detector name represents the right or left side of the ingot. Because L and R originate from the same section of the ingot, they should have similar physical characteristics and therefore similar detector performance.

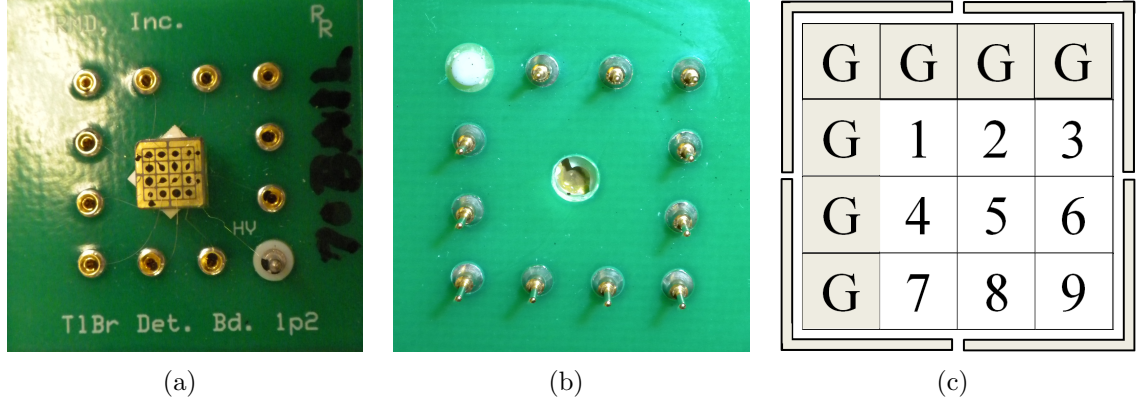


Figure 3.2: A photograph of a typical TlBr detector fabricated by RMD. (a) The pixel array. The top row and left column of “pixels” are grounded to create a guard ring. (b) The cathode side. A hole is drilled into the substrate to allow alpha particle irradiation in some detectors. (c) Map of pixels to their number designations. The G’s represent “pixels” grounded together to form a guard ring. These grounded “pixels” are also connected to the metal strips surrounding the pixel array.

carbon paste, and the detector was mounted to a ceramic substrate which was then mounted to a printed circuit board. The anode is arranged in 4 x 4 pixel array with pixel dimensions of 0.8 mm x 0.8 mm and a 1-mm pixel pitch. Seven of the pixels were connected and grounded to create a guard ring. Figure 3.2 shows a typical TlBr detector. The cathode is on the printed circuit board side, but alpha irradiation is possible in some detectors through a hole in the board as shown in figure 3.2(b).

3.2 Experimental Setup

3.2.1 Standard Experimental Setup

To read out the detector signals, the electrodes are connected to Endicott Interconnect Technologies, Inc. (formerly eV Microelectronics) model eV-5093 charge sensitive preamplifiers via the printed circuit board shown in figure 3.4. The printed circuit board described in figure 3.4 was contained in an aluminum enclosure and connected to a personal computer via RG174 coaxial cables as shown in figure 3.3. Voltage signals from the preamplifier outputs of all nine anode pixels and the planar

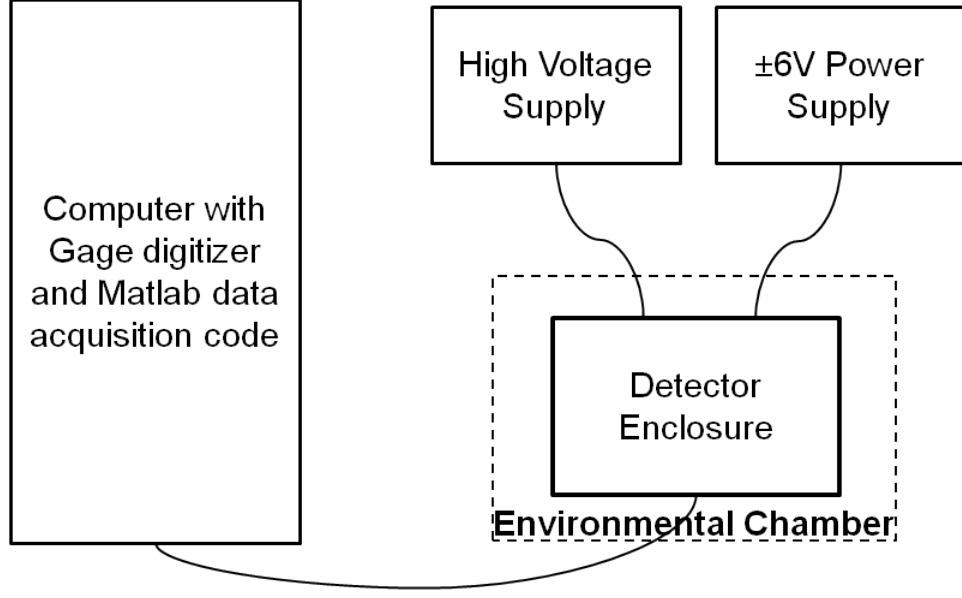


Figure 3.3: Block diagram illustration of the data acquisition setup. The aluminum enclosure contains the detector and readout electronics. All ten channels (nine anode pixels and the planar cathode) are connected to the Gage digitizer on the personal computer via RG174 coaxial cables. The $\pm 6\text{V}$ power supply powers the preamplifiers and the high voltage supply provides high voltage for the cathode.

cathode were digitized and recorded using a 14-bit GaGe Octopus CompuScope PCI bus on a personal computer. The data were acquired using a Matlab code in pulse mode, such that all ten channels were read out after a single anode channel triggered the system. Each recorded waveform had 512 data points sampled every 100 ns (i.e. $51.2\ \mu\text{s}$). Measurements in Chapters IV and V were performed in a Thermotron S-1.2-3200 environmental chamber to maintain a constant ambient temperature of -20°C , while the measurements for Chapter VI were performed at room temperature.

3.2.1.1 Circuit Board Design

The circuit shown in figure 3.4 was the second design iteration. In the original circuit design, poor grounding lead to signal crosstalk and gain variation between channels, demonstrated in figure 3.5. Implementing ground and power planes and increasing the separation between the cathode channel and the nine pixel channels eliminated the crosstalk problem. Some measurements presented in this work were

performed with the original circuit design, and the resulting features are discussed.

3.2.2 Collimator Measurement Setup

The relationship between the CAR reconstructed depth and the true depth was studied using the setup illustrated in figure 3.6. The collimator vertical position was mounted to a positioning stage which was adjustable on the order of microns. Due to the geometry constraints illustrated in figure 3.7, the minimum achievable distance between the detector and the collimator was approximately 1.5 inches.

3.3 Methods

3.3.1 Data Post-processing

Prior to analysis, the data were filtered for single pixel events and then processed to determine pulse amplitudes and timing. Pulse height estimates calculated by the change in the signal baseline were first compared to a simple threshold to determine the number of interactions per event. Guard ring data were not recorded; therefore, a multiple pixel event involving the guard ring could be confused for a single pixel event, adding low-energy counts to the spectrum continuum. Consequently, events having a cathode signal greater than three times the pixel signal of an alleged single-pixel event were identified as guard ring events and discarded.

A second simple threshold separated alpha events from gamma-ray events. Then, pulse amplitudes for single-pixel gamma-ray events were evaluated using a digital CR-(RC)¹ filter with 10 μ s anode and 20 μ s cathode shaping times. A constant fraction timing method resolved the time at which charge was induced on the pixel. Due to its slow rise, the cathode signal was passed through a fast shaper and compared to a threshold to determine the time at which the interaction occurred.

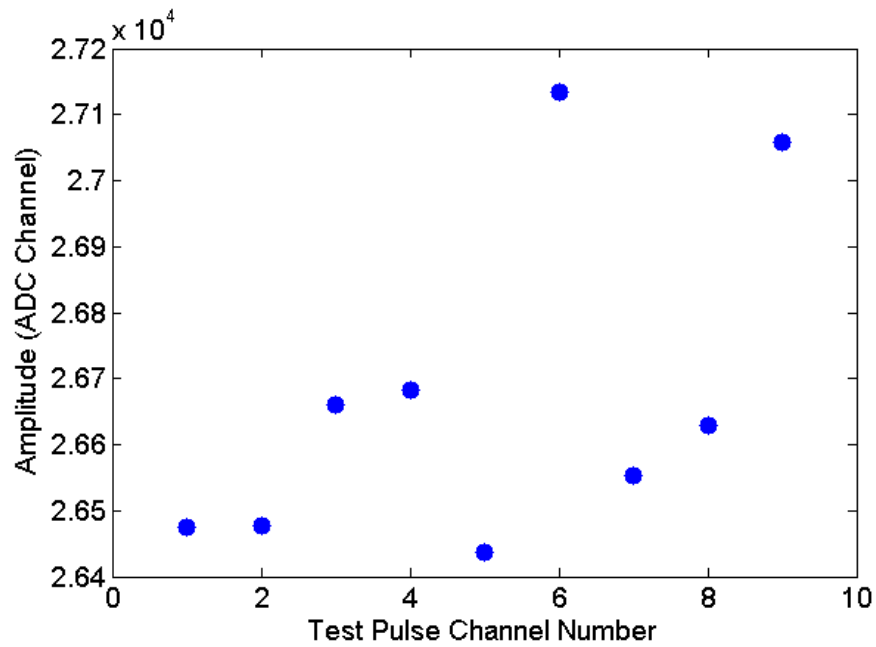


Figure 3.5: Test pulse preamplifier output signal amplitudes for each channel. Channel-by-channel signal gain variations are corrected using the methods described in Section 3.3.2.1.

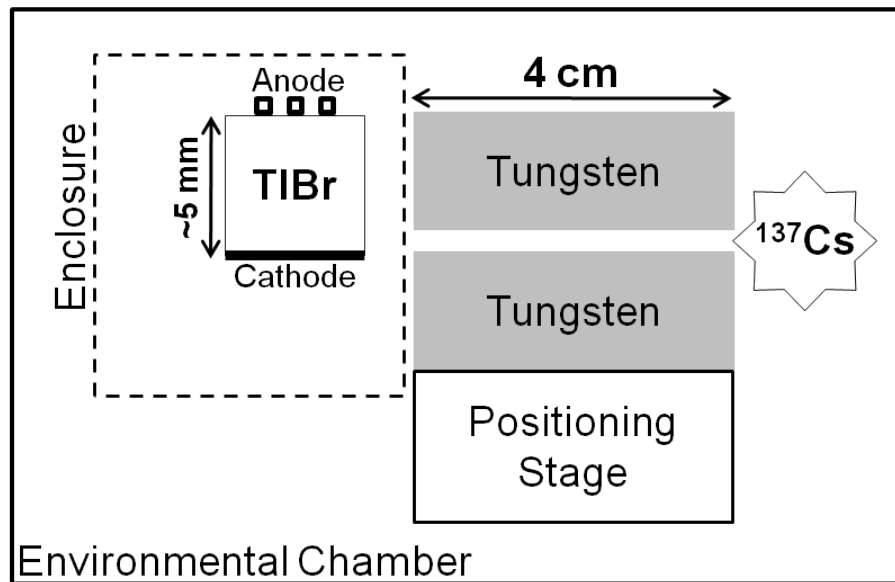


Figure 3.6: Block diagram of the collimator measurement setup. The separation between the two blocks of tungsten is controlled by a micrometer. The vertical position of the collimator is controlled by a positioning stage and measured with a micrometer. This diagram is not to scale.

3.3.2 Gamma-ray Data Analysis

3.3.2.1 Depth-dependent Data from the Cathode-to-Anode Signal Ratio

The TlBr devices tested in this work were pixelated, such that the anode signal is uniform at all depths while the cathode signal changes linearly with depth. Consequently, the cathode-to-anode signal ratio can provide depth-dependent data which are used to study material properties. For example, the energy resolution and photopeak centroid channels as functions of depth revealed trapping behavior within a device. Furthermore, depth-dependent photopeak electron drift time data may be used to calculate the electron drift velocity as a function of depth. Leading edge time pick-off methods were implemented without concern for amplitude walk because only single-interaction ^{137}Cs photopeak events were considered. Using these data, the mobility (assuming it remains constant) may then be calculated from Eq. 3.4 which is derived from Eq. 3.1, 3.2, and 3.3, and where V_{bias} is the applied voltage, E_x is the electric field along the detector depth, and d is the detector thickness. Note that Eq. 3.2 is distinguished from 3.3 to explicitly show the assumption that mobility is constant. The electric field may then be estimated as a function of depth from Eq. 3.3.

$$V_{bias} = \int_0^d E_x(x) dx \quad (3.1)$$

$$v_x(x) = E_x(x) \mu(x) \quad (3.2)$$

$$E_x(x) = \frac{v_x(x)}{\mu} \quad (3.3)$$

$$\mu = \frac{1}{V_{bias}} \int_0^d v_x(x) dx \quad (3.4)$$

3.3.2.2 Depth Correction Verification using a Collimator

The relationship between the CAR reconstructed depth and the true depth was studied using a mechanical tungsten collimator. Measurements of 230 μCi of ^{137}Cs collimated through a 50 μm slit were made starting at the cathode side and moving to the anode side in 0.635 mm increments. The cathode side was established by determining the position at which source counts were first detected. Details of the experimental setup are described in section 3.2.2.

3.3.2.3 Energy Correction Considerations for Detectors with Non-Negligible

$$\mu_h\tau_h$$

Some TlBr detectors have non-negligible hole mobility-lifetime products ($\mu_h\tau_h$), on the order of $10^{-4} \text{ cm}^2/\text{V}$ [68], relative to their electron mobility-lifetime products ($\mu_e\tau_e$), demonstrated by the slow rise in the measured cathode waveforms in Fig. 3.8. As a result, the CAR is overestimated at most depths which distorts the CAR depth-based energy correction. To circumvent this problem, the energy correction was calculated based on the electron drift time for detectors with high $\mu_h\tau_h$.

3.3.3 Alpha Waveform Analysis

In order to visualize trends present in the alpha-particle data, raw waveforms were filtered and adjusted based on techniques previously applied to CdZnTe detectors [69], as illustrated in Fig. 3.9. Using filters based on peak amplitudes and peaking times, the gamma-ray and pileup events were eliminated. Due to attenuation in air or source material or a possible thin inactive region on the cathode, the remaining alpha waveforms have a range of peak amplitudes. However, all alpha-particle-induced electron clouds are produced only at the cathode side and drift through the entire bulk of the crystal, so the waveforms were normalized. Finally, a baseline shift was applied to align all of the waveforms. The drift velocity was determined at each depth

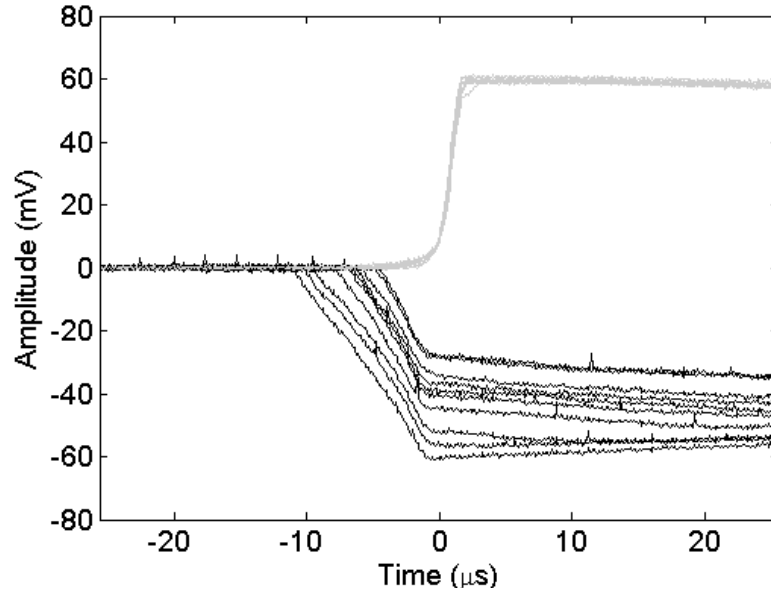


Figure 3.8: Collecting pixel (with positive slopes near time zero) and the cathode (with negative slopes during $-10 \mu s \leq t < 0 \mu s$) photopeak waveforms measured from ^{137}Cs irradiating all depths. The slow rise in the cathode waveforms, which are plotted negative to differentiate from anode pulses, indicates hole collection.

for each pixel by calculating an average waveform from thousands of waveforms and assuming a change in amplitude is proportional to a change in depth.

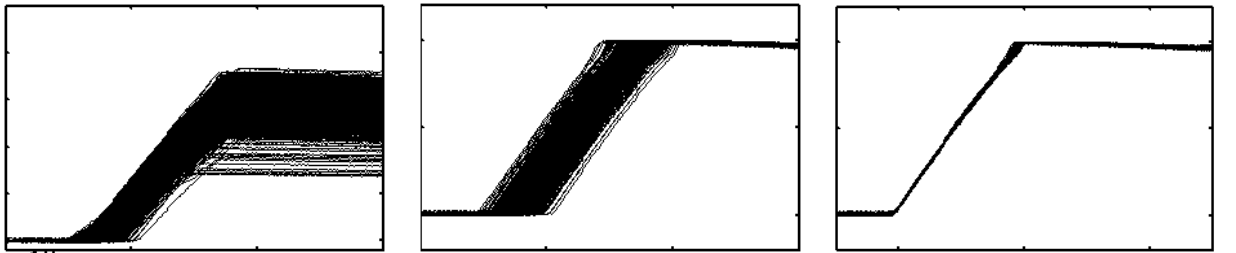


Figure 3.9: From left to right: the raw alpha waveforms after filtering, the normalized alpha waveforms, and the aligned waveforms after applying a baseline shift. In each figure, the x-axis represents time and the y-axis represents the pulse amplitude.

CHAPTER IV

Characterization of Stable Operation

While TlBr detectors demonstrate undesirable transient behavior (described in chapters V and VI), this chapter shows that TlBr detectors can achieve good energy and depth resolution. Additionally, these detectors demonstrated good charge transport properties and suffered little performance degradation due to electron trapping.

4.1 Depth Reconstruction

Accurate depth reconstruction is necessary in order to correct for the effects of charge carrier trapping and the weighting potential in pixelated detectors. The efficacy of CAR depth reconstruction in TlBr detectors was studied using the methods described in section 3.3.2.2. CAR depth distributions at various collimated depths are shown in Fig. 4.1. The centroid of the CAR reconstructed depth distribution matched each true depth, and the FWHM for each distribution was approximately 300 μm for this detector. These data show that the CAR properly reconstructs depth in a pixelated TlBr detector with relatively low $\mu_h\tau_h$.

Some TlBr detectors have shown a relatively high $\mu_h\tau_h$. For these detectors, the CAR is overestimated due to the hole contribution in the cathode signal. Furthermore, high $\mu_h\tau_h$ causes nonlinearity in the CAR near the cathode side due to complete electron and hole collection occurring within the cathode shaping time. This region

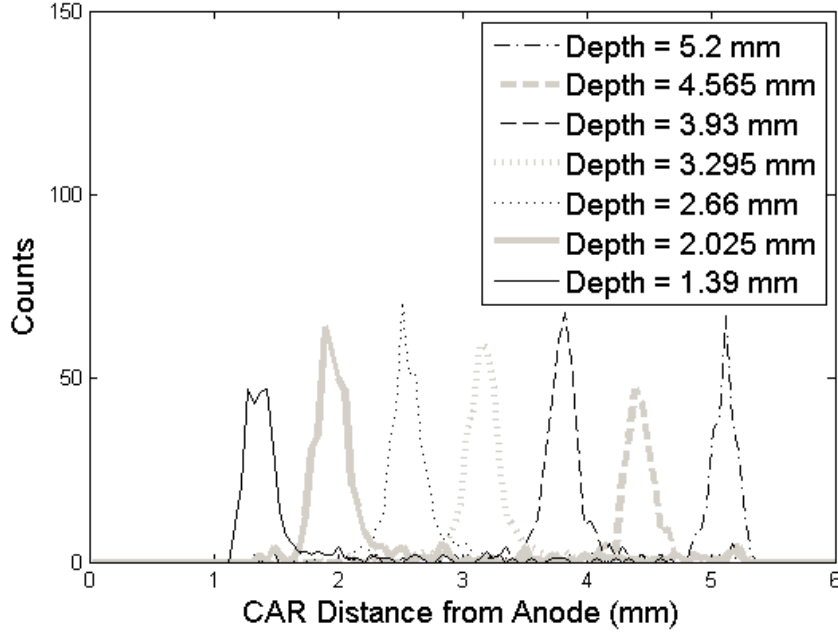


Figure 4.1: Detector 935-16B1R CAR depth distributions for various collimated depths. The same measurement time was used for each distribution. Because this detector has relatively low $\mu_h\tau_h$, the true depth has a one-to-one relationship with the CAR depth.

of nonlinear CAR will increase as $\mu_h\tau_h$ increases. Fig. 4.2 shows the CAR depth as a function of true depth for a detector with relatively high $\mu_h\tau_h$ using 24 μs and 8 μs cathode shaping times. Perfect depth reconstruction would produce a one-to-one relationship between the CAR depth and the true depth, but fig. 4.2 shows the CAR is overestimated at each depth. The slope approaches unity and the offset approaches zero as the shorter cathode shaping time excludes portions of the hole movement; however, ballistic deficit causes portions of the electron component to be excluded at depths near the cathode as the cathode shaping time decreases.

To achieve optimal spectroscopic performance the CAR need not be a strict linear function of depth; however, each depth must be associated with a single CAR value in order to properly reconstruct the deposited energy. Contrariwise, accurate depth reconstruction is essential for Compton imaging because images are created from the three-dimensional interaction locations. Because the cathode shaping time may not

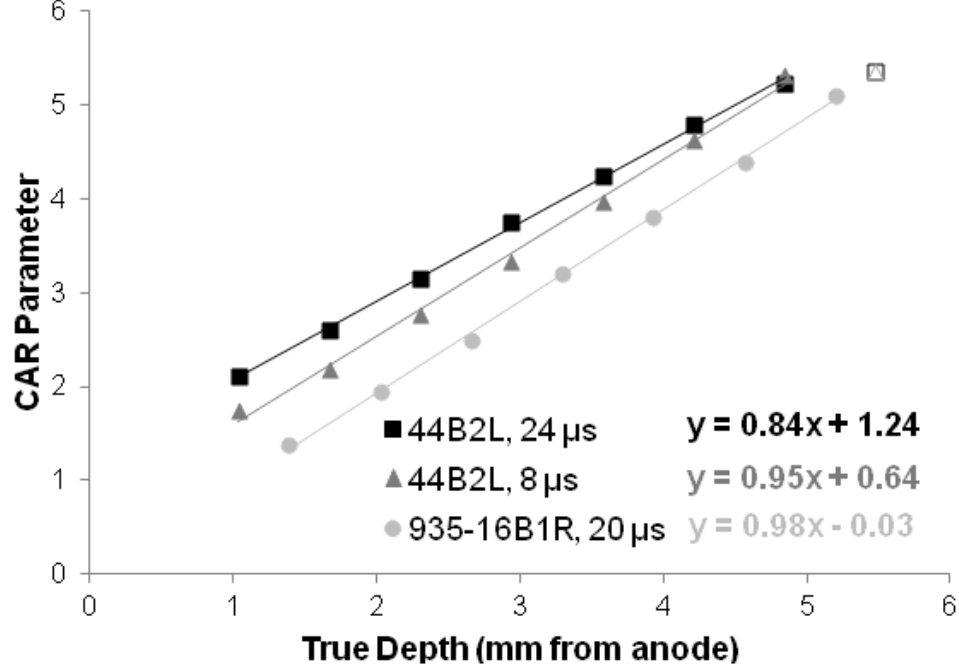


Figure 4.2: Depth calculated from the CAR parameter as a function of true depth for detectors 935-16B1R and 44B2L. Having relatively high $\mu_h\tau_h$, the slope approaches unity (from 0.84 to 0.95) and the offset approaches zero (1.2 to 0.64) for detector 44B2L as the cathode shaping time decreases. Data from the cathode side were not included in the linear fits due to the similarity in cathode pulse amplitudes for the collimator position at the cathode and the collimator position 0.635 mm away from the cathode. For comparison, the slope and offset for a detector with low $\mu_h\tau_h$ (935-16B1R) are 0.98 and 0.03 respectively.

be perfectly optimized for each depth, the electron components of cathode waveforms could instead be isolated with digital signal processing. For the purposes of this work, it was sufficient to perform the energy correction using the electron drift time instead of the CAR*.

4.2 Spectroscopic Performance

Table 4.1 summarizes the FWHM at 662 keV for multiple TlBr detectors, each approximately 5 mm thick with nine anode pixels and a planar cathode. The spectroscopic performances of these devices were relatively consistent, maintaining an overall

*The methods for drift time energy correction are described in section 3.3.2.3.

energy resolution near 2% at 662 keV. Figure 4.3 shows that the best-performing detectors do not necessarily originate from the beginning (the most pure) end of the ingot.

Detector 935-16B1R achieved the best performance, shown in figure 4.4(a), reaching sub-1% overall depth-corrected energy resolution. Similar performance was observed in detector 935-16B1L, which was the pair to detector 935-16B1R. Detector 47AR(R) in figure 4.5 also achieved near-1% overall depth-corrected energy resolution and demonstrated good spectroscopic performance in most pixels. Due to relatively low hole mobility in these detectors, the standard CAR depth-correction technique was implemented.

Detectors 70BA1R and 70BA1L demonstrated relatively high $\mu_h\tau_h$. Likewise, detector 44B2L exhibited relatively high $\mu_h\tau_h$. The energy-corrected spectra in figures 4.6 and 4.7 were generated using the drift time as a depth indicator. Despite the relatively high $\mu_h\tau_h$, these detectors performed well as single-polarity charge-sensing detectors.

These spectra demonstrate features indicative of a TlBr ^{137}Cs spectrum. At 662 keV, the ^{137}Cs photopeak is pronounced. A smaller peak near 590 keV is also present due to the detector geometry and data processing techniques. Thallium can emit a 73 keV $\text{K}\alpha_1$ characteristic x-ray, which may either be collected by neighboring pixel or escape the detector entirely. Because only single pixel events were analyzed, events in which the ^{137}Cs photoelectric interaction and the characteristic x-ray photoelectric interaction occurred in different pixels were classified as multiple-pixel events and discarded. The ^{137}Cs Compton continuum begins near 500 keV, and a backscatter peak is present near 200 keV. Charge lost in the gap between pixels results in low-energy tailing on all the spectral features.

Table 4.1: TlBr Spectroscopic Performance [1, 2]

Detector ID	Date Tested	Overall Energy Resolution	Best Pixel Energy Resolution
		at 662 keV	at 662 keV
58A3R	June 2010	1.32%	0.93%
58A4L	May 2010	1.98%	1.04%
48A2R	March 2011	4.26%	3.16%
935-16B1R	May 2011	0.97%	0.73%
935-16B1L	June 2011	1.17%	0.94%
44B2L	September 2011	2.45%	1.71%
70BA1L	December 2011	1.69%	1.35%
70BA1R	December 2011	1.35%	1.12%
47AR(R)	April 2012	1.47%	0.96%
44A12R(R)	June 2012	4.28%	2.94%
43A4(R)	September 2012	3.87%	2.89%
70BA2R(RR)	September 2012	2.98%	2.04%
44AB1(R)	September 2012	1.82%	1.37%

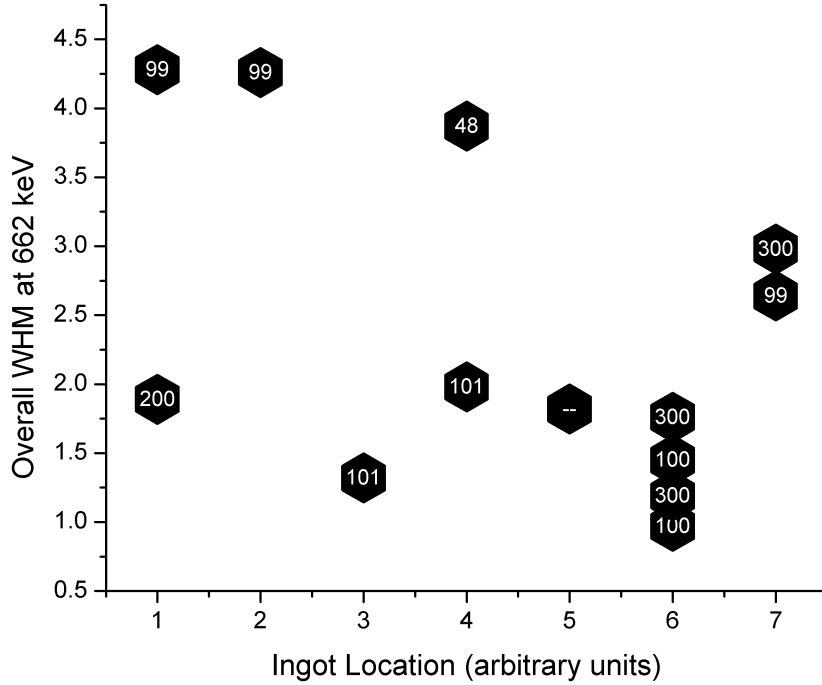
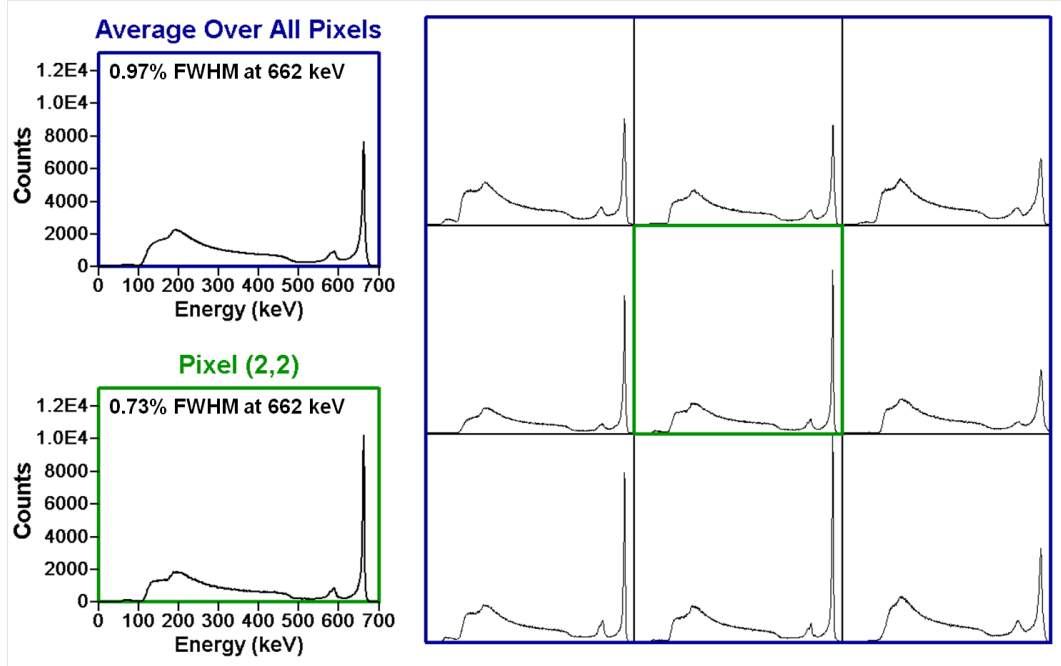
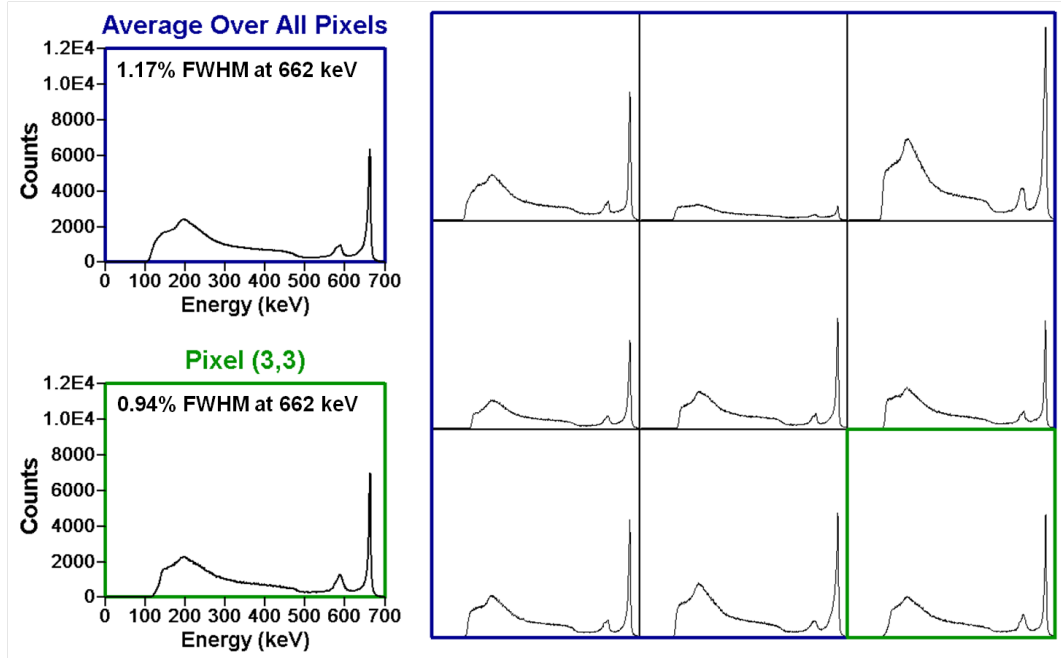


Figure 4.3: Graphical representation of the energy resolution as a function of the ingot location from which the detector originated. The x-axis represents the relative ingot location. Numerical values were assigned to the relative ingot location starting from the section A. The number labels indicate the number of zone refining passes.



(a)



(b)

Figure 4.4: (a) Detector 935-16B1R and (b) detector 935-16B1L pixel-by-pixel Cs^{137} depth-corrected spectra during the stable condition.

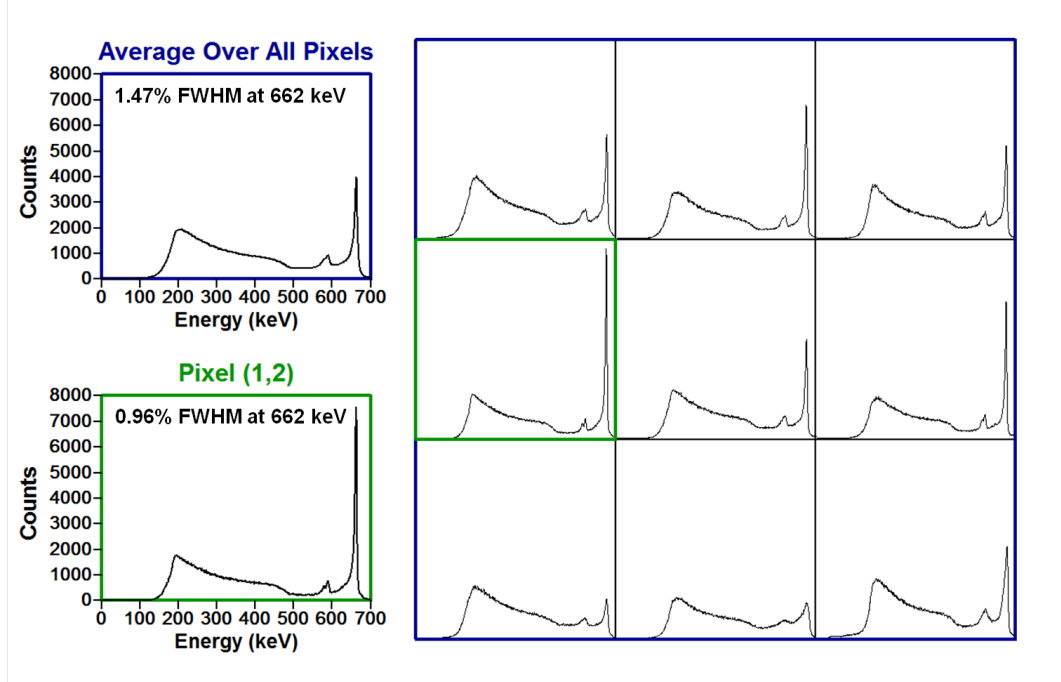
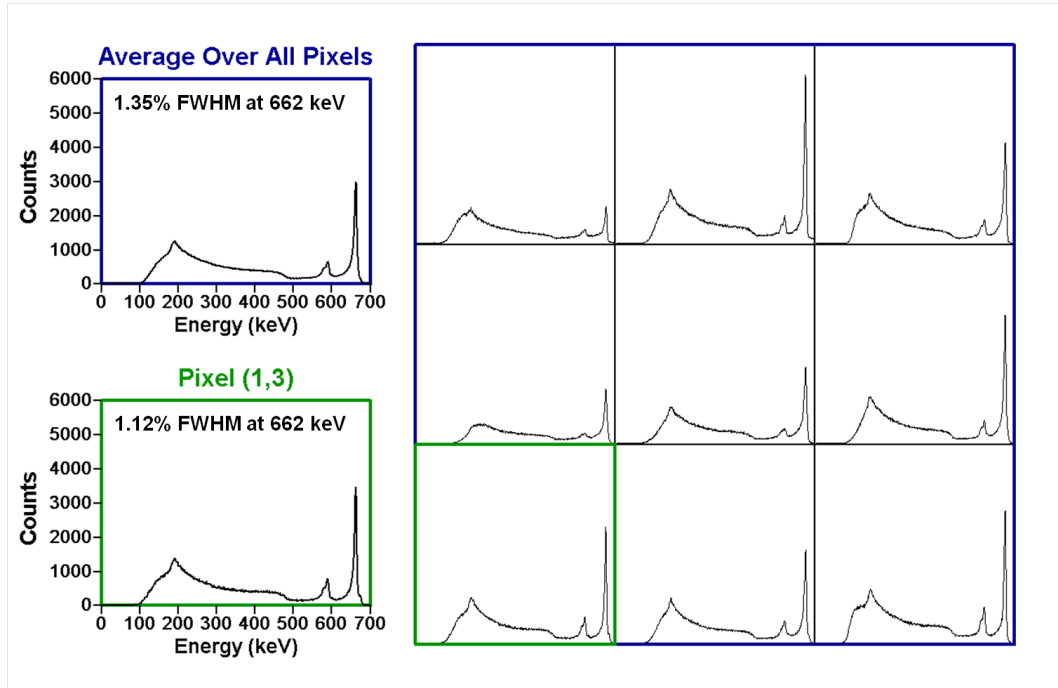


Figure 4.5: Pixel-by-pixel Cs^{137} energy-corrected spectra for detector 47AR(R) during the stable condition. Good spectroscopic performance is demonstrated in all pixels.

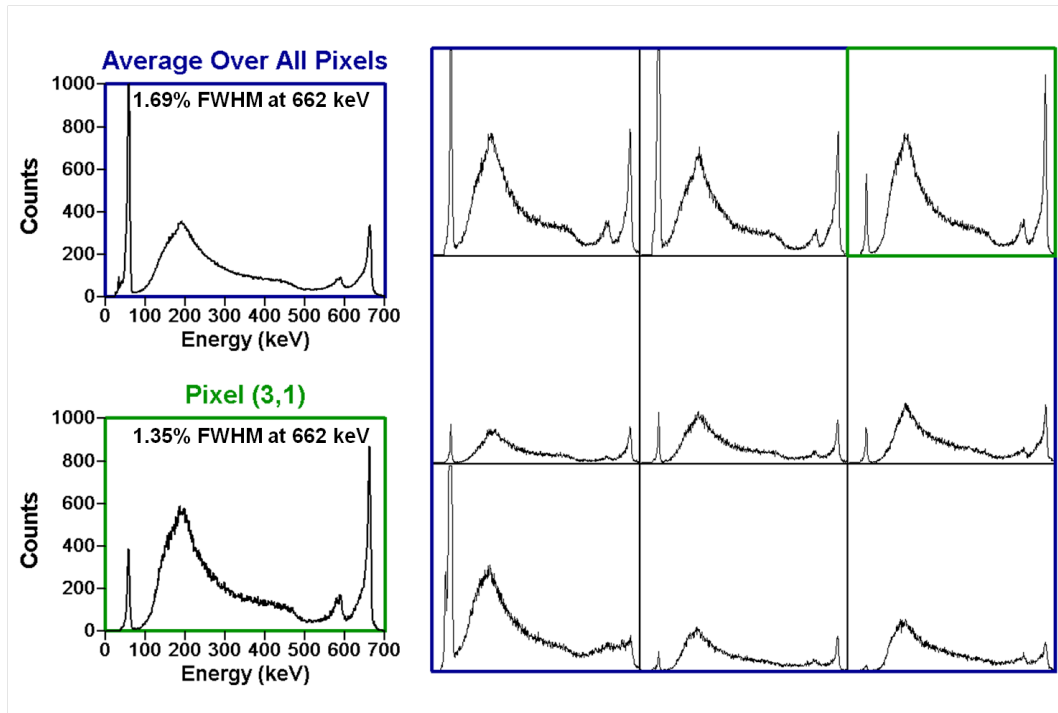
4.3 Material Properties

The energy resolution and photopeak centroid were binned as a function of depth in the CAR depth correction process, making it possible to evaluate the bulk detector material quality. Surface preparation and electrode quality will cause systematic performance degradation at all depths, and are therefore differentiable from factors that cause depth-dependent performance variation.

Fig. 4.8 shows detector 935-16B1R has little or no performance degradation due to charge carrier trapping in the best-performing pixels (refer to fig. 4.4(a)). Uniformity in the energy resolution at each depth indicates uniform material, i.e. no concentration of trapping centers, whereas poor electron transport would cause the energy resolution to degrade from the anode to the cathode. The photopeak centroid is affected by both weighting potential and trapping (e.g. Pixel (3,3) in fig. 4.8(b)). In the absence of electron trapping, the photopeak centroid amplitude would remain



(a)



(b)

Figure 4.6: (a) Detector 70BA1R and (b) detector 70BA1L pixel-by-pixel Cs^{137} energy-corrected spectra during the stable condition.

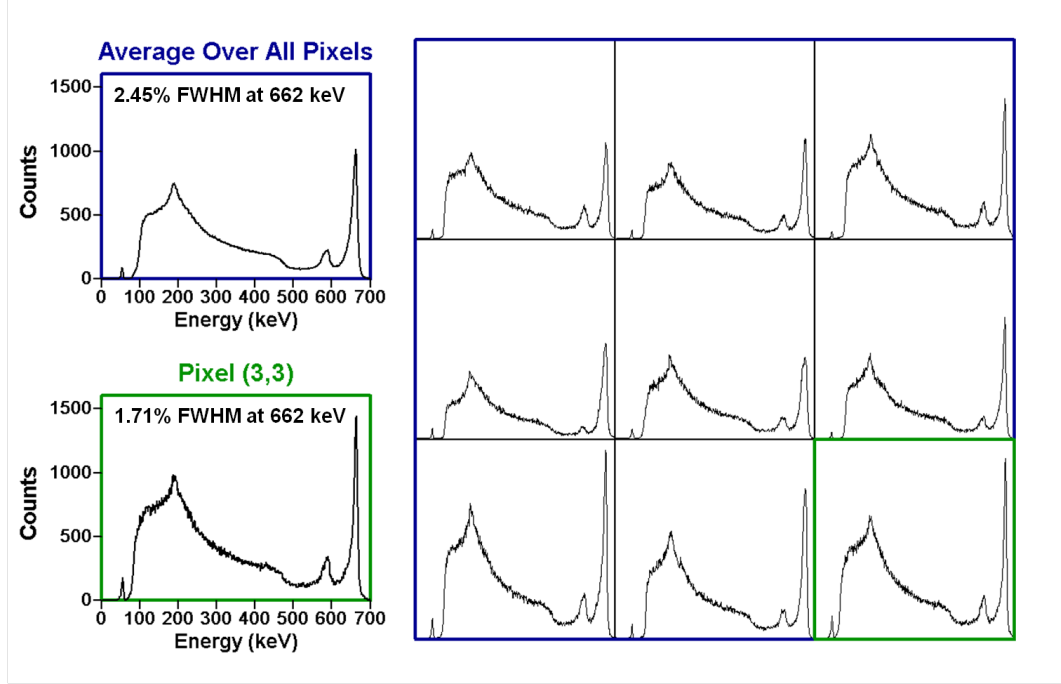


Figure 4.7: Pixel-by-pixel Cs^{137} energy-corrected spectra for detector 44B2L during the stable condition. Good spectroscopic performance is demonstrated in all pixels.

uniform or gradually vary at most depths and decrease more rapidly near the anode side as a result of large weighting potential change (e.g. Pixel (1,3) in fig. 4.8(b)). Assuming uniform bulk trapping the photopeak centroid amplitude should increase as a function of depth from the cathode side to the anode side (e.g. Pixel (3,3) in fig. 4.8(b)). A trapping center at a given depth would cause a sharp decrease in photopeak centroid and increase in energy resolution at that depth (e.g. Pixel (3,3) in fig. 4.8). The sharp increase in FWHM near the anode side in every pixel of every detector is due to the large anode weighting potential change.

Because detectors 935-16B1L and 935-16B1R originated from the same horizontal location described in figure 3.1(a), the material quality and impurity concentration should be similar. However, detector 935-16B1L experienced worse overall spectroscopic performance than detector 935-16B1R, and figure 4.9 shows less performance degradation due to electron trapping centers.

Having relatively high $\mu_h\tau_h$, detectors 70BA1R, 70BA1L and 44B2L were analyzed

using the drift time energy correction described in section 3.3.2.3. Consequently, the centroid and FWHM are binned as a function of drift time as a depth indicator rather than CAR depth. Similar to detectors 935-16B1R and 935-16B1L, these detectors demonstrated little performance degradation due to electron trapping.

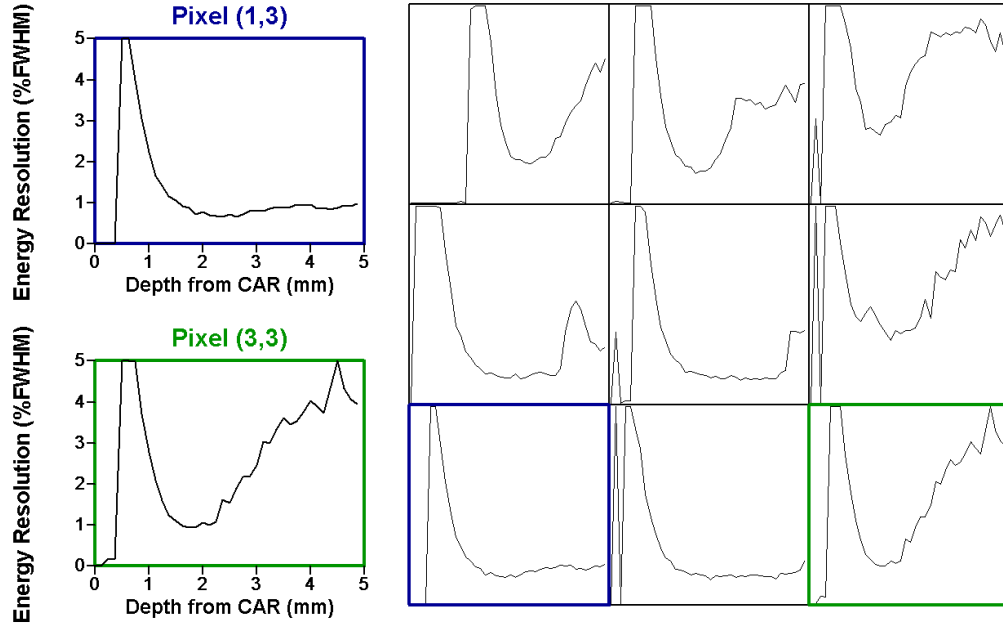
4.3.1 Electron Drift Velocity

Using the methods described in section 3.3.3, cathode-side alpha irradiation data provide the depth-dependent electron drift velocity (figures 4.15, 4.16, and 4.17). For detectors lacking cathode access, the electron drift velocity was calculated from photopeak drift time data (figures 4.12, 4.13, and 4.14). Assuming the mobility is constant, the electron drift velocity profiles reveal the electric field is approximately 2000 V/cm at all depths in all detectors.

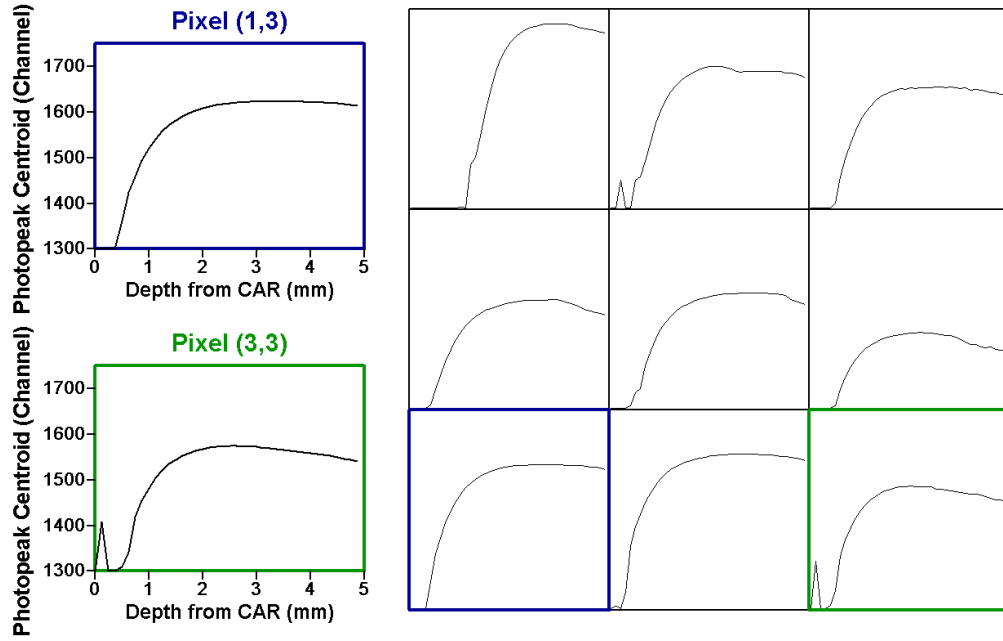
4.4 Summary

Hole movement in some detectors distorted the CAR, but this obstacle was overcome by using the drift time rather than the CAR to execute the energy correction. Because the CAR-calculated depth is less sensitive to a non-uniform electric field, standard CAR depth correction was implemented for detectors with negligible hole transport. Furthermore, the CAR is the most accurate depth correction process for many detectors and creates the ability to evaluate bulk detector material quality from gamma-ray data. Good depth resolution was demonstrated for a 5-mm thick TlBr detector with low $\mu_h\tau_h$. Overall energy resolution of 1.01% FWHM at 662 keV and 0.78% at 662 keV on a single pixel was demonstrated on detector 935-16B1R.

From the limited number of samples, no definitive conclusions may be drawn with respect to how the manufacturing process relates to detector performance. The number of zone refining passes is not necessarily related to the difference in spectroscopic performance, material quality or hole transport property. Detectors 935-16B1L



(a)



(b)

Figure 4.8: (a) The energy resolution as a function of depth is relatively uniform for the best-performing pixels in detector 935-16B1R, indicating low electron trapping. (b) The weighting potential effect is apparent in the photopeak centroid channel as a function of depth plot, but there is little effect due to charge trapping. The CAR was overestimated in pixel 1 as a result of the signal crosstalk described in section 3.2.1.1.

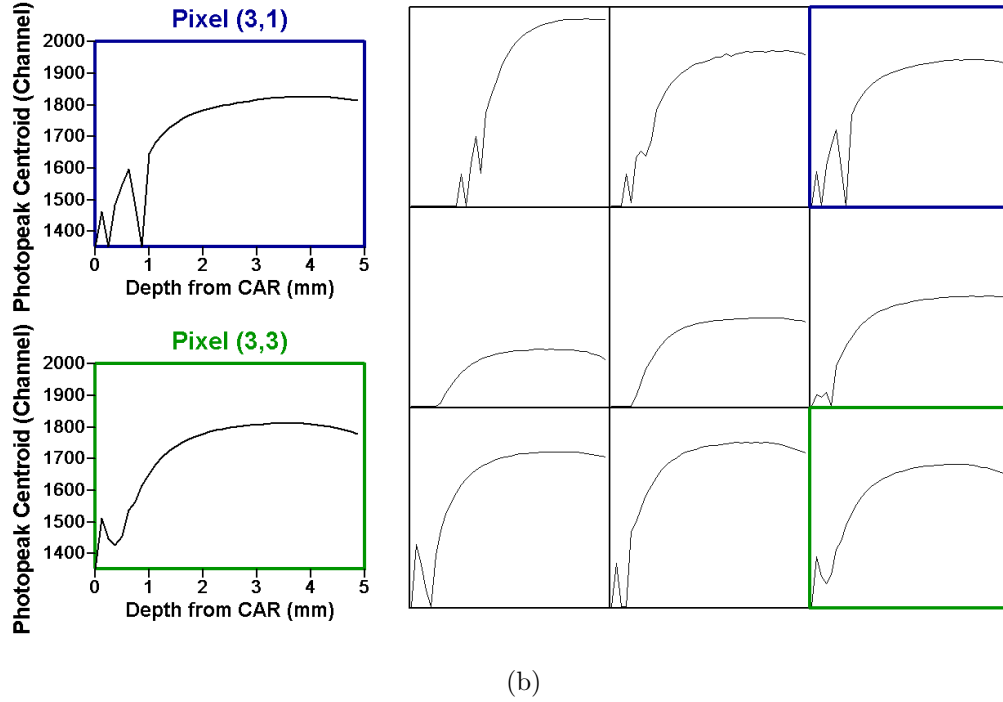
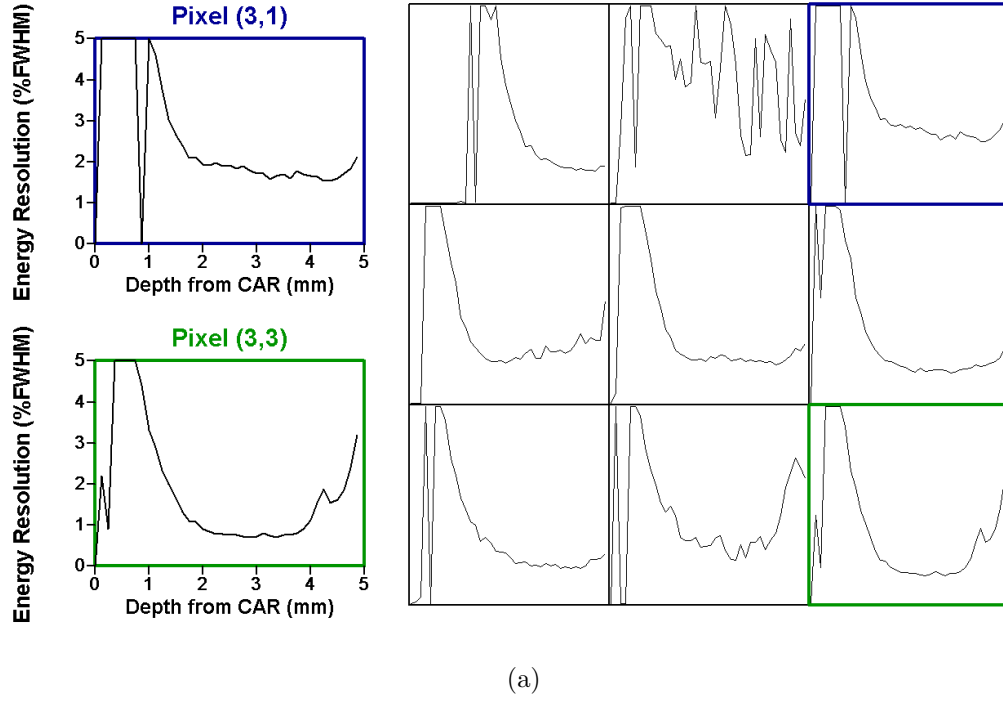


Figure 4.9: (a) The energy resolution as a function of depth is relatively uniform for the best-performing pixels in detector 935-16B1L, indicating uniform electron trapping. (b) The weighting potential and uniform bulk trapping effect is apparent in the photopeak centroid channel as a function of depth plot. The CAR was overestimated in pixel 1 as a result of the signal crosstalk described in section 3.2.1.1.

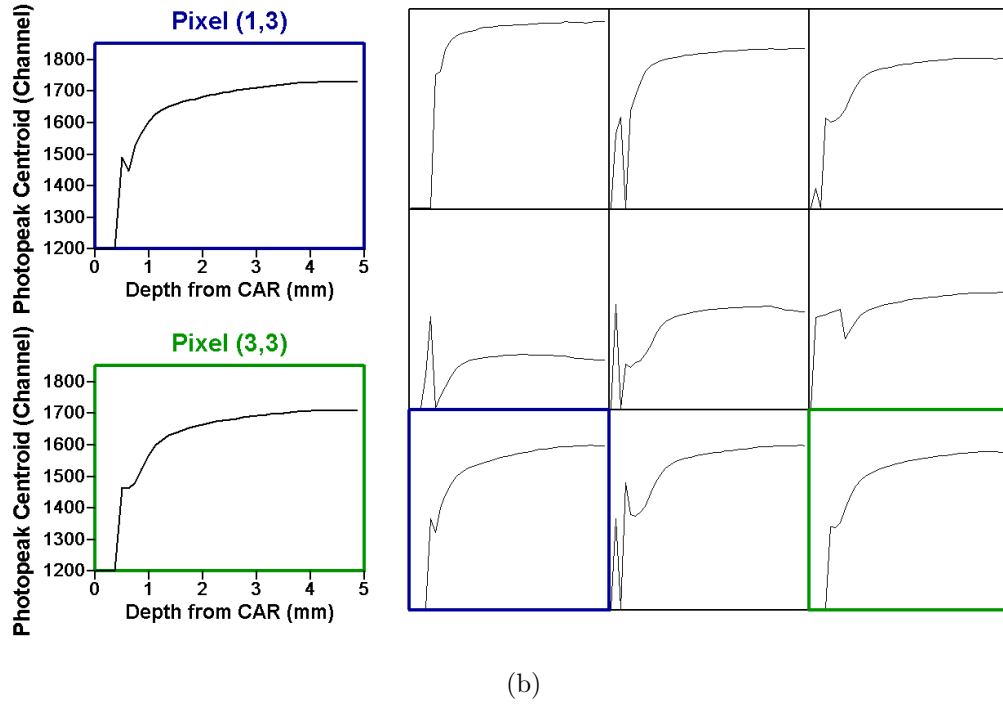
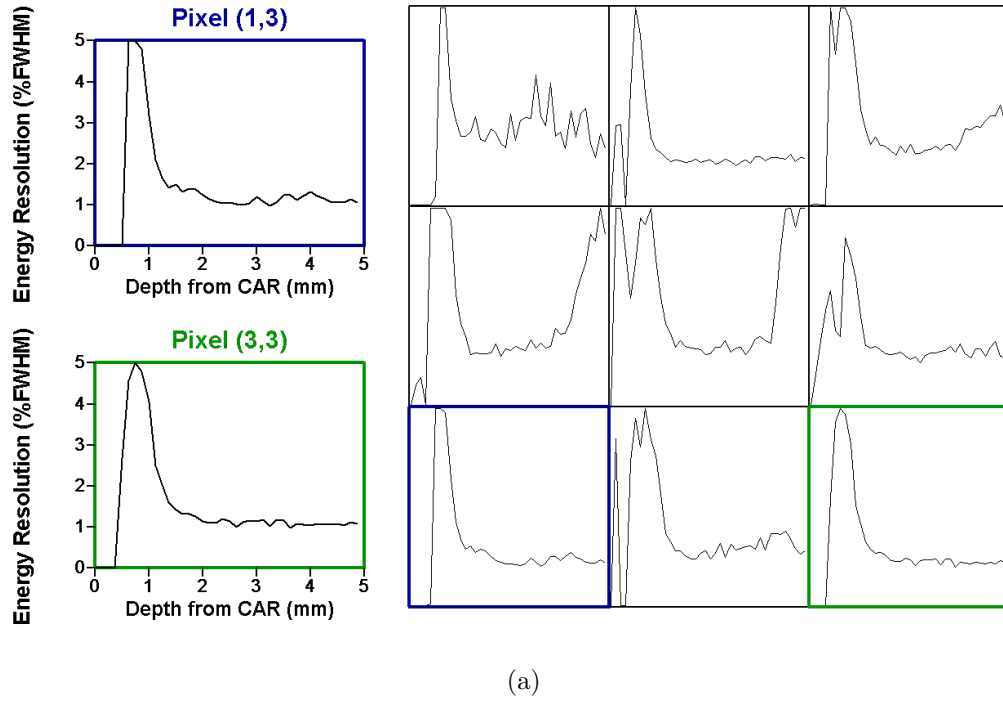
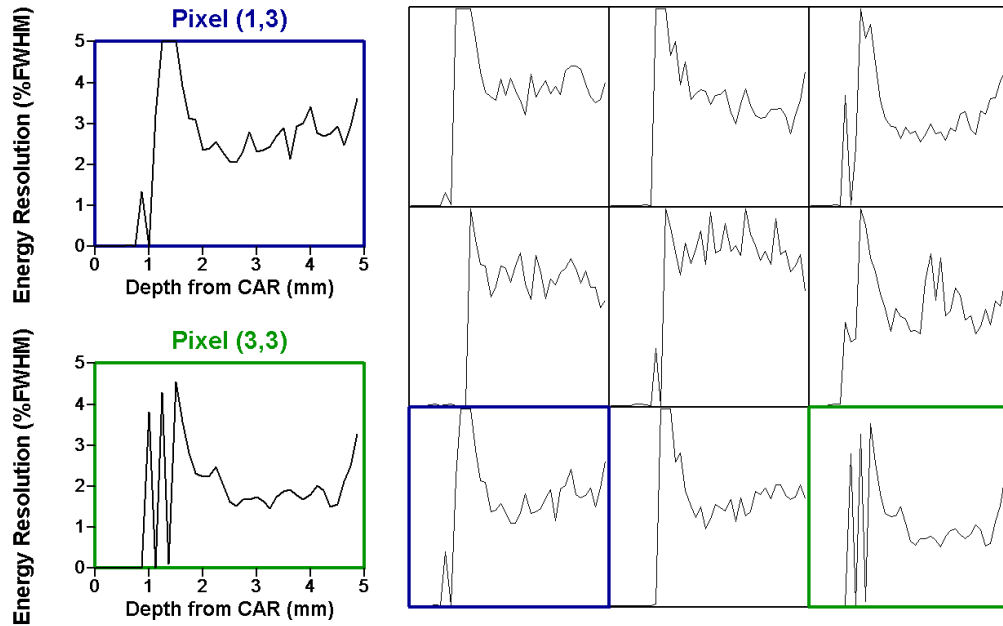
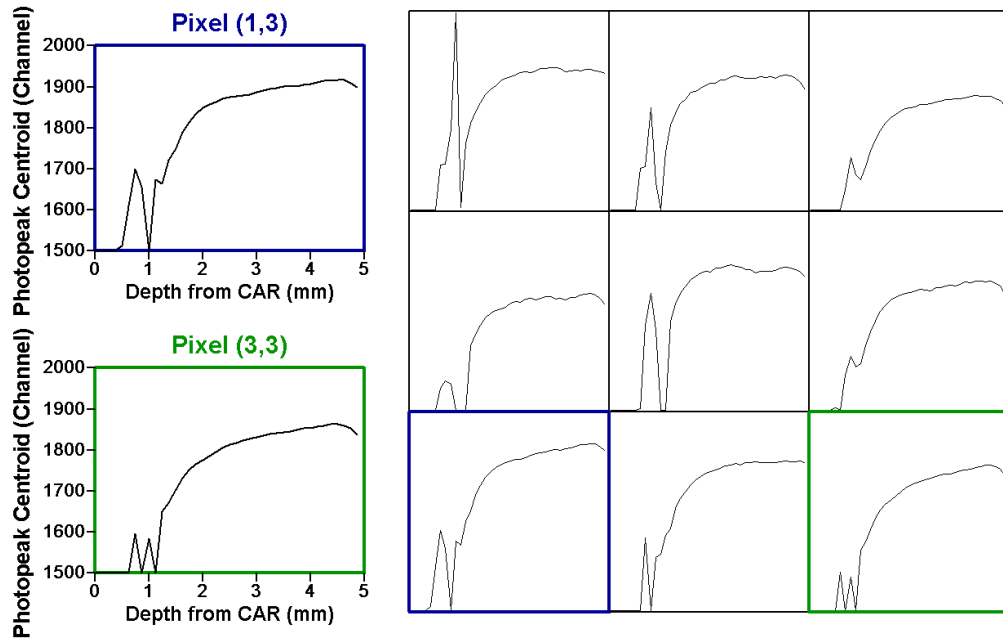


Figure 4.10: (a) The energy resolution as a function of depth is relatively uniform for the best-performing pixels in detector 70BA1R, indicating low electron trapping. (b) The weighting potential effect is apparent in the photopeak centroid channel as a function of depth plot, but this detector is less affected by charge trapping than detector 935-16B1R.



(a)



(b)

Figure 4.11: (a) The energy resolution for detector 44B2L is overall worse than the other detectors; however, the energy resolution as a function of depth is relatively uniform. (b) The weighting potential as well as the effect from electron trapping is apparent in the photopeak centroid channel as a function of depth plot.

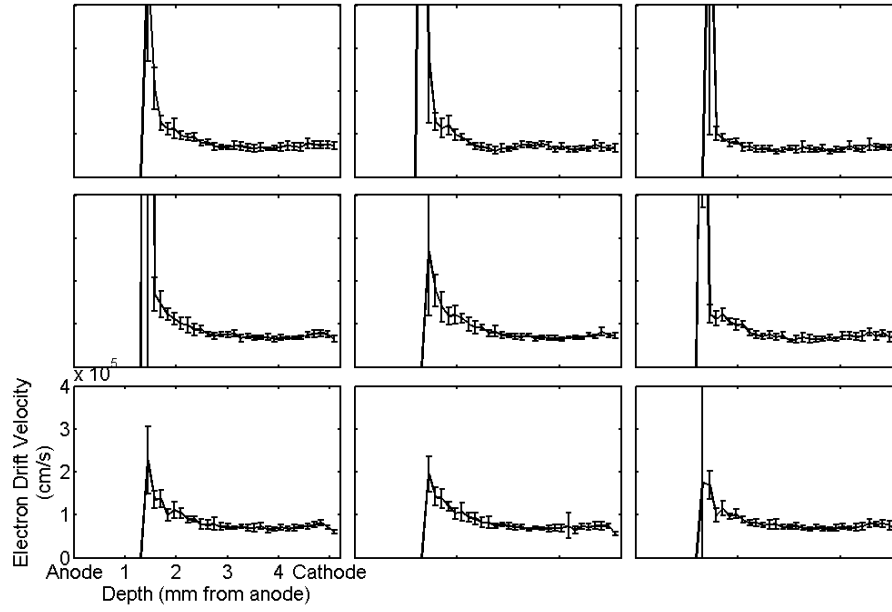


Figure 4.12: Detector 935-16B1R electron drift velocity calculated from Cs-137 photopeak events. The depth was calculated from the CAR, so the lack of data near the anode side is due to imperfect calculation of the CAR. The error bars represent experimental error, and the large error near the anode is due to poor counting statistics. The electron drift velocity is otherwise relatively uniform and approximately 10^5 cm/s in most depths.

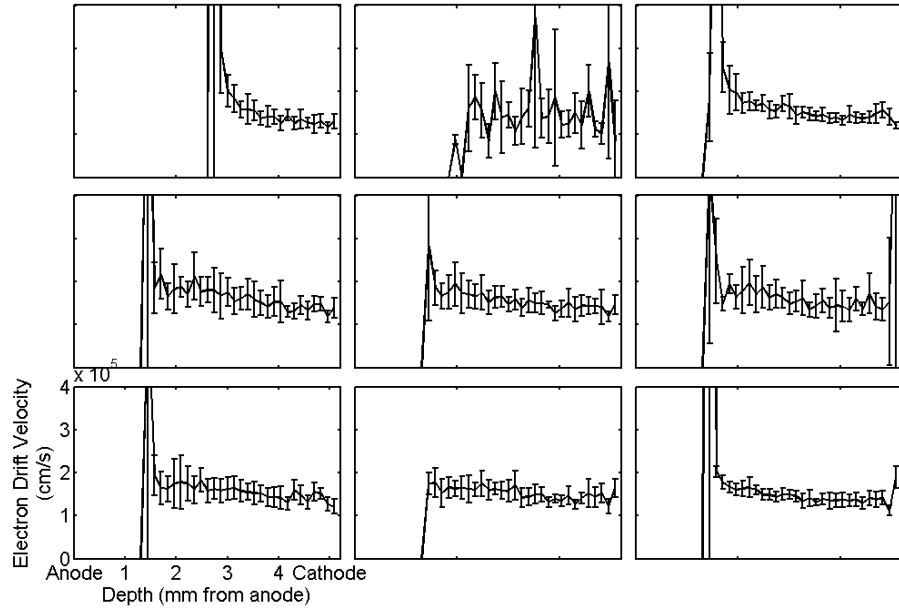


Figure 4.13: Detector 935-16B1L electron drift velocity calculated from ^{137}Cs photopeak events. The depth was calculated from the CAR, so the lack of data near the anode side is due to imperfect calculation of the CAR. The error bars represent experimental error, and the large error near the anode is due to poor counting statistics. The electron drift velocity is otherwise relatively uniform and approximately 2×10^5 cm/s in most depths.

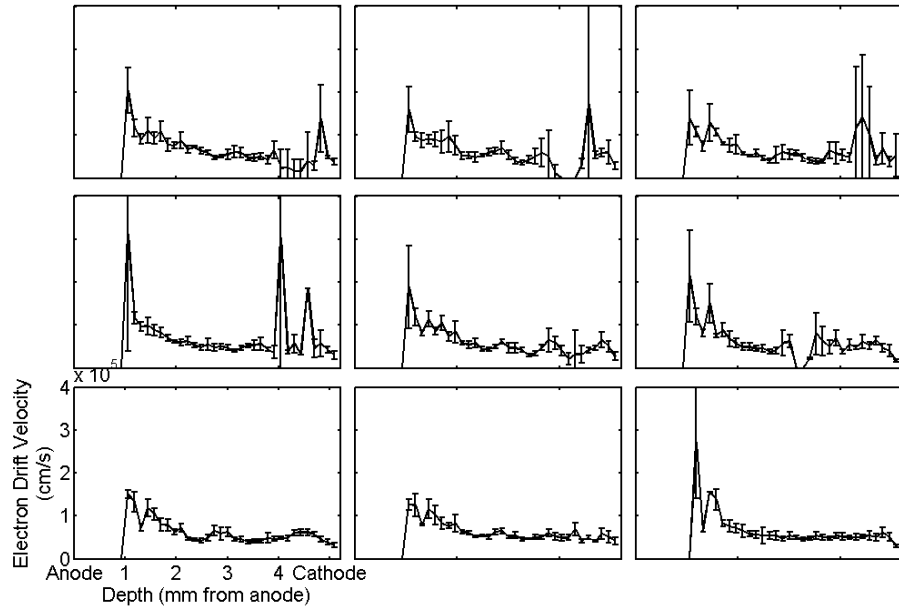


Figure 4.14: Detector 44B2L electron drift velocity calculated from Cs-137 photopeak events. The depth was calculated from the CAR, so the lack of data near the anode side is due to imperfect calculation of the CAR. Many depths have poor counting statistics, but the electron drift velocity in most depths is approximately 10^5 cm/s.

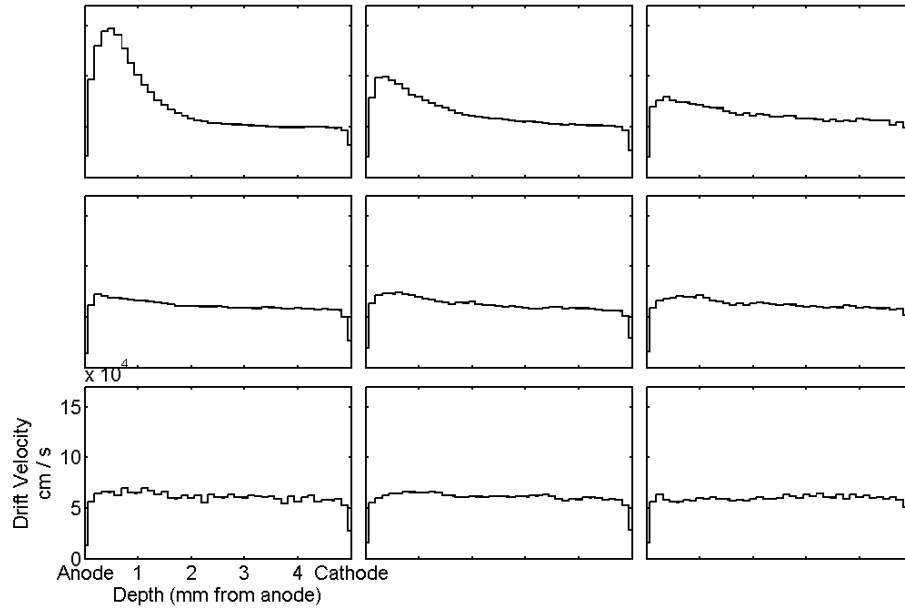


Figure 4.15: Detector 70BA1R electron drift velocity calculated from ^{241}Am alpha particle cathode-side irradiation. The electron drift velocity is uniform in most pixels except pixel (1,1) where the drift velocity at the anode side is more than double that of the cathode side.

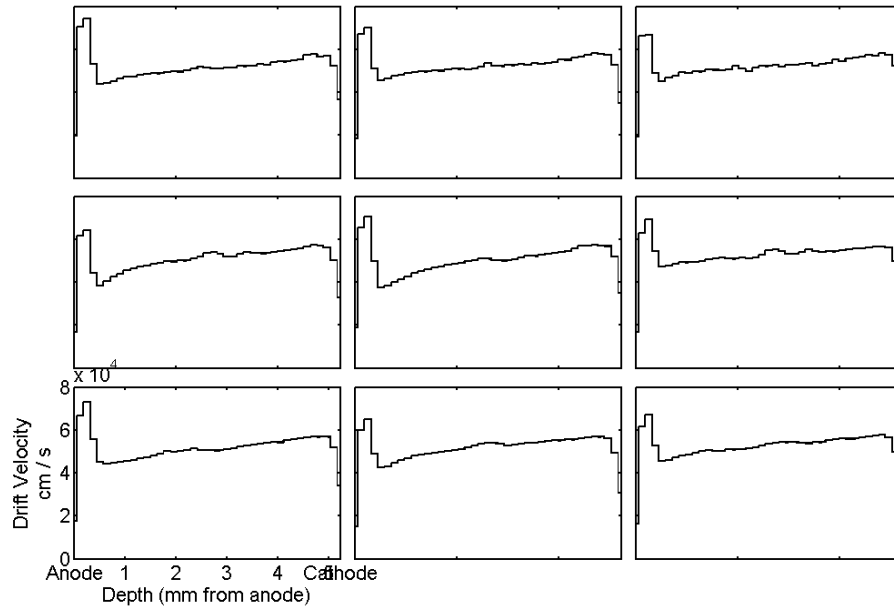


Figure 4.16: Detector 70BA1L electron drift velocity calculated from ^{241}Am cathode-side irradiation. The drift velocity is not uniform with respect to detector depth; however, each pixel shares a similar drift velocity profile, having higher drift velocities near both electrodes.

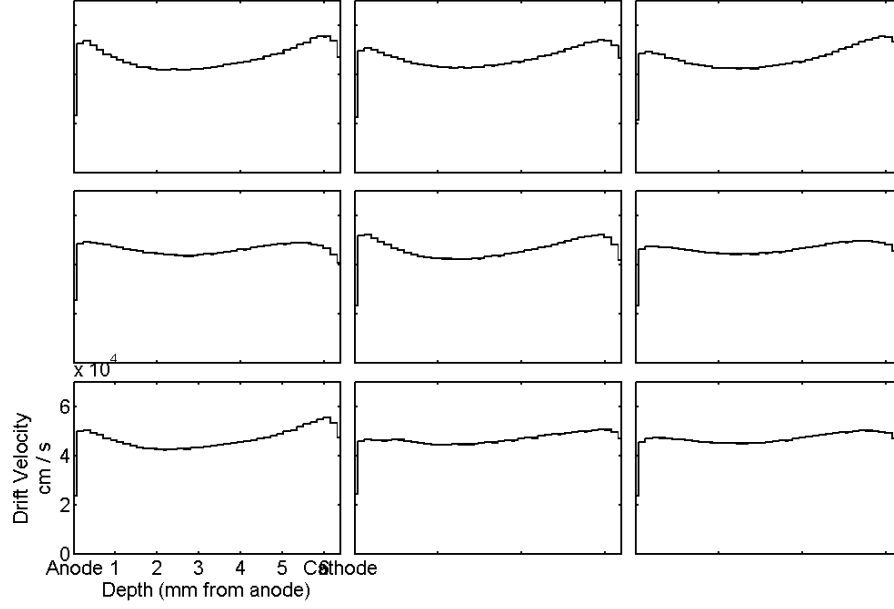


Figure 4.17: Detector 47AR(R) electron drift velocity calculated from ^{241}Am cathode side irradiation. Similar to detector 70BA1R, the drift velocities are higher near both electrodes.

and 935-16B1R demonstrated the best spectroscopic performance of all the detectors tested yet was zone refined with only 100 passes. Furthermore, detectors 935-16B1L and 935-16B1R demonstrated relatively low $\mu_h\tau_h$, but were zone refined with a comparable number of passes as detector 44B2L which had a high $\mu_h\tau_h$. Nevertheless, the depth-dependent gamma ray data show the material quality is consistently good between samples. Given that the detector and electrode geometry, fabrication techniques, data acquisition, and data processing have room for significant improvement, these spectroscopic results and material characteristics are promising.

CHAPTER V

Characterization of the Conditioning Phase

Similar to HgI_2 detectors [70], some TlBr detectors must complete a conditioning phase prior to stable operation. Immediately following the first cathode bias application, TlBr detectors generally demonstrate poor spectroscopic performance. The spectroscopic performance of most TlBr detectors tested in this work improved as the electron drift velocity and signal gain changed during operation at -20°C . The duration of this transient behavior is detector-dependent, but generally stabilization occurs after one or two weeks at -1000 V cathode bias operating and at -20°C .

This chapter characterizes the conditioning phase for multiple detectors and demonstrates that not all detectors necessarily require conditioning prior to stable operation. Gamma-ray data reveal how the spectroscopic performance changes while alpha particle data show how the electron drift velocity changes during this initial transition phase. Due to geometry constraints, alpha particle irradiation was not physically possible for detectors 935-16B1R, 935-16B1L, and 44B2L. The electron drift velocity may be estimated with gamma-ray data after stabilization, but photopeak drift time data were not statistically significant prior to stabilization making the electron drift velocity impossible to calculate.

5.1 Results

Detector 935-16B1R demonstrated the most dramatic spectroscopic improvement after conditioning (4.32% to 0.97% FWHM at 662 keV for the overall corrected spectrum shown in figure 5.1) and the best overall performance of all the detectors that were tested. The ^{137}Cs spectrum in figure 5.2 shows both the photopeak counts and signal amplitude increased as the detector stabilized. The 3D spectrum in figure 5.2(b) shows the photopeak is initially present in depths near the anode only and presents itself in all depths after the detector stabilized. If the electron drift velocity increased during this conditioning period (similar to detectors 70BA1R and 70BA1L), the amount of charge sharing would have decreased as the detector stabilized, which is reflected in multiple-pixel event classification shown in figure 5.3. Furthermore, events near the anode would not suffer as much from diffusion or charge trapping which is demonstrated in the 3D spectrum. The change in each pixel's contribution to single-pixel events shown in figure 5.3(b) also indicates non-uniformity initially present in the internal electric field which then becomes uniform as the detector stabilizes, which is also reflected in figure 4.13.

The overall single-pixel energy resolution for detector 935-16B1L improved from 6.13% to 1.04% FWHM at 662 keV, shown in figure 5.4. Similar to detector 935-16B1R, detector 935-16B1L experienced a gain shift as well as increased photopeak in most depths, shown in figure 5.5. As more events cross the trigger threshold and the post-processing amplitude threshold, the total events increased. The fraction of single pixel events increased by approximately 10% as the fraction of multiple pixel events decreased. The fractional contribution of each pixel also changed until the detector stabilized, but there is no obvious relationship between a pixel's single pixel event contribution (figure 5.6) and its spectroscopic performance. The poor efficiency observed in pixel 2 is likely due to field non-uniformity, causing pixel 3 to collect events occurring under pixel 2.

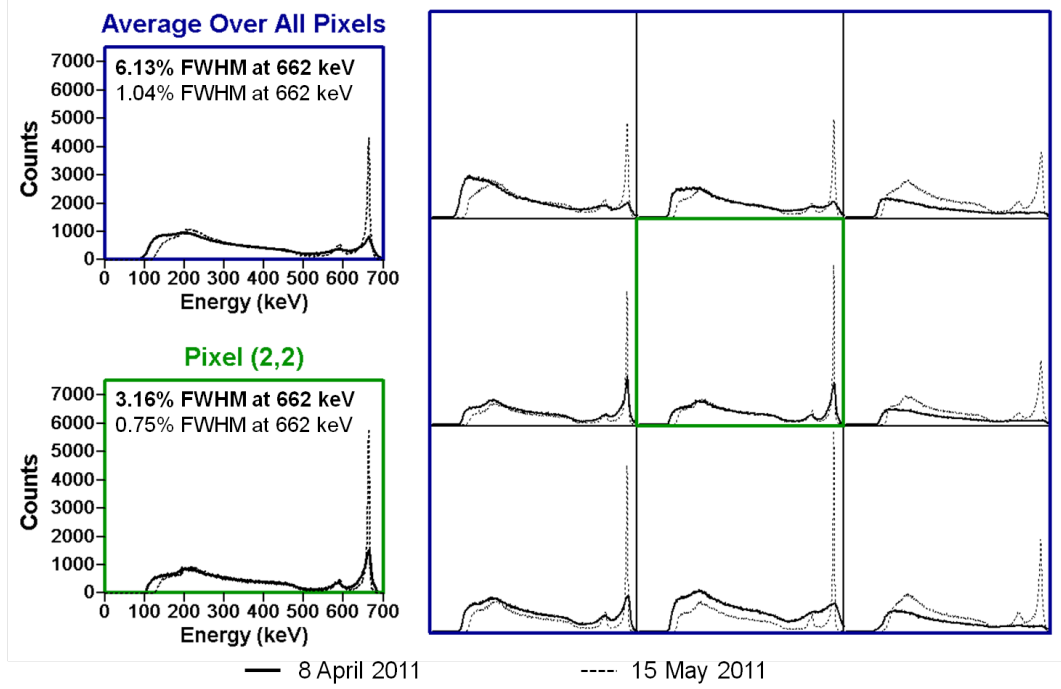
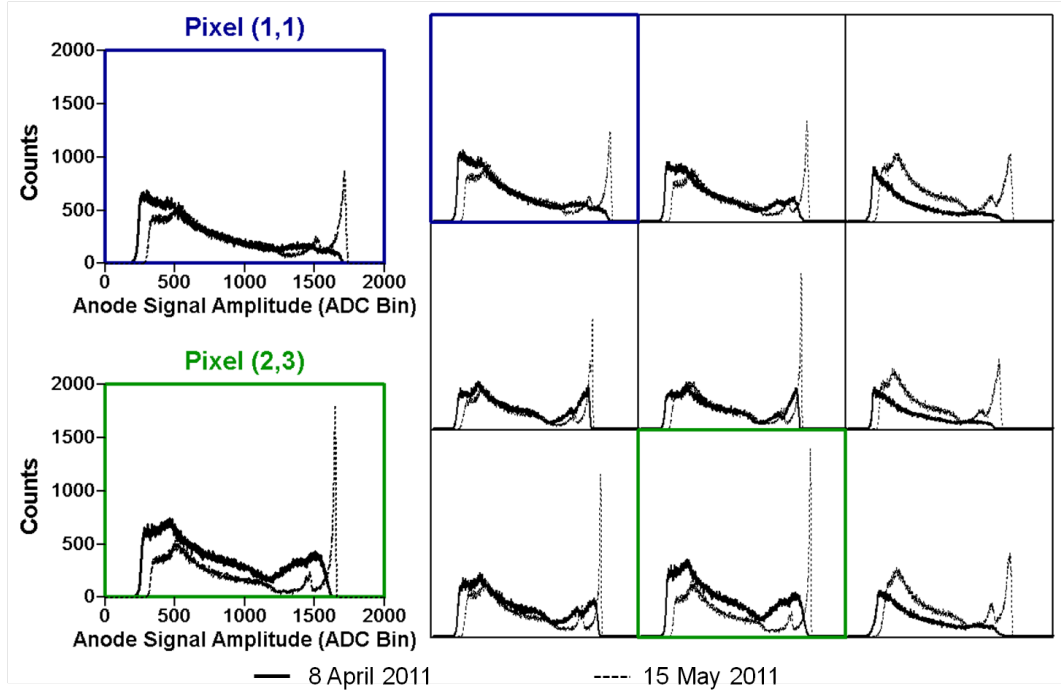


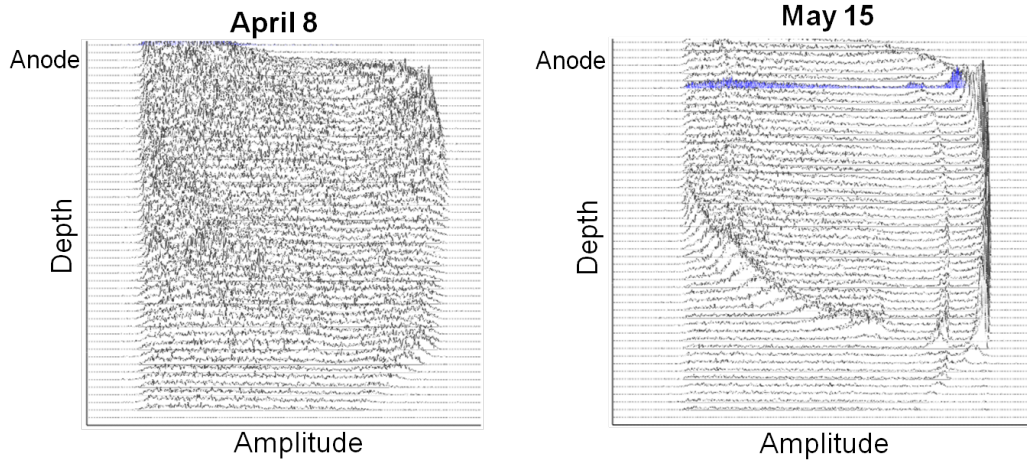
Figure 5.1: The overall corrected energy resolution improved significantly for detector 935-16B1R. Significant improvement was observed in all pixels.

Despite its different origin, detector 44B2L also experience similar characteristics during this initial transition phase. The same increased gain and photopeak counts in the 3D spectrum were observed in figure 5.8, and the corrected spectrum improved significantly. The fraction of single pixel events also increased by approximately 10%, and the collecting pixel distribution in figure 5.9 shows the field became more uniform as the detector stabilized.

The gamma-ray data in figure 5.10 show the spectroscopic performance for detector 70BA1R did not change appreciably. Figure 5.10(b) shows the photopeak centroid slightly increased, but behaved similarly in both measurements. As expected from the relatively stable spectroscopic performance, figure 5.11 shows little change in event classification. Figure 5.12(a) shows the drift velocity increased in the central region of the detector, and generally became more uniform as the detector stabilized. The average electron drift velocity in figure 5.12(b) also increased as a function of time, as did the fraction of classified single pixel events in figure 5.11(a).

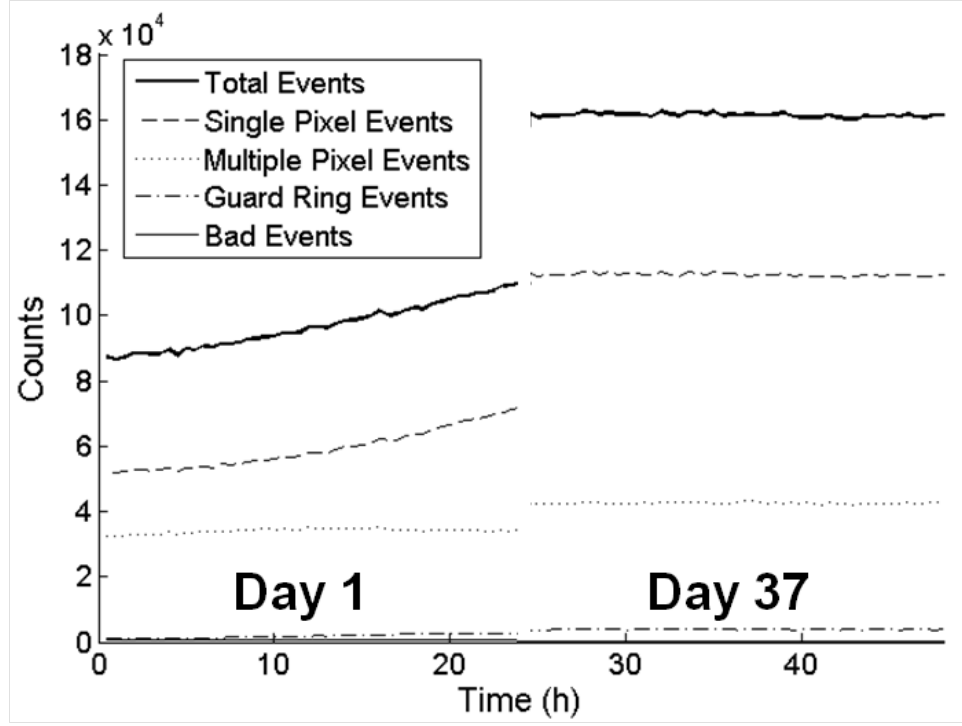


(a)

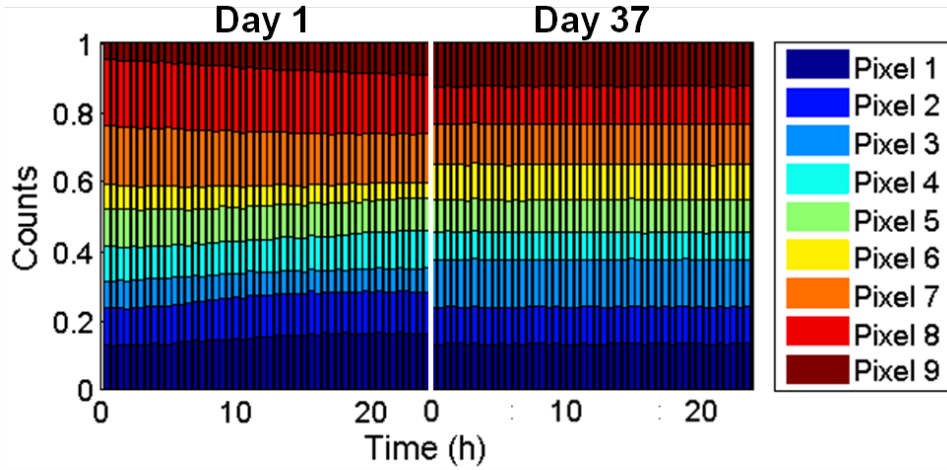


(b)

Figure 5.2: (a) The signal amplitude and photopeak efficiency increased as detector 935-16B1R stabilized. (b) The photopeak is initially not present in most depths in pixel 8. Similar poor performance at depths away from the anode was observed in all pixels. Both measurement times are the same for comparison.



(a)



(b)

Figure 5.3: Event classification for the first 24-hour measurement and a 24-hour measurement after detector 935-16B1R stabilized shown together on the same plots. (a) As the signal gain increases, more events cross the trigger threshold and more events pass the amplitude threshold in post-processing. The fraction of single-pixel events increases from approximately 60% of the total events initially to approximately 70% of the total events as the fraction of multiple pixel events decreases from 35% to 25%. (b) The contribution of each pixel to single-pixel events becomes relatively constant and more uniform in the detector's stable state.

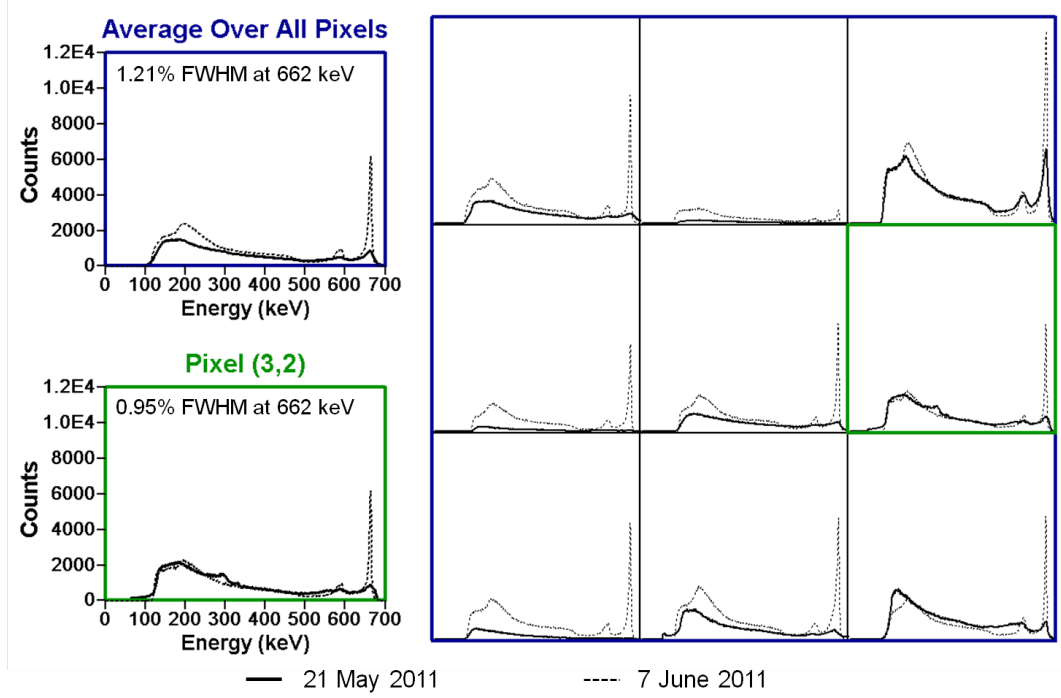


Figure 5.4: The overall corrected energy resolution was not measurable in the first measurement and improved significantly by the second measurement for detector 935-16B1L.

Figure 5.13 shows detector 70BA1L experienced improvement in energy resolution, and the photopeak centroid increased in most pixels. However, this detector demonstrated enigmatic behavior. The efficiency degraded in every pixel, and the photopeak disappeared in pixel 7. Figure 5.14 shows the total number of counts decreased between the measurements, and the detector suffered from some instability during the second measurement. However, the alpha data in figure 5.15 are still reliable and show the average drift velocity increased and became more uniform as a function of detector depth.

The detector in figure 5.16 showed insignificant changes in both spectroscopic performance and drift velocity possibly indicating not all TlBr detectors necessitate dramatic conditioning before achieving stable operation. Detector 47AR(R) is different from the other detectors in that it was re-fabricated from detector 47AR.

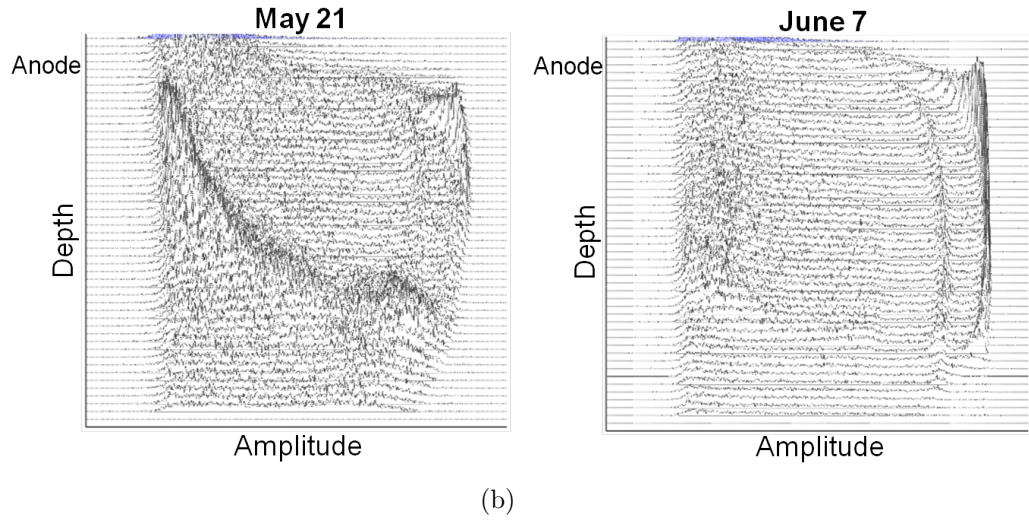
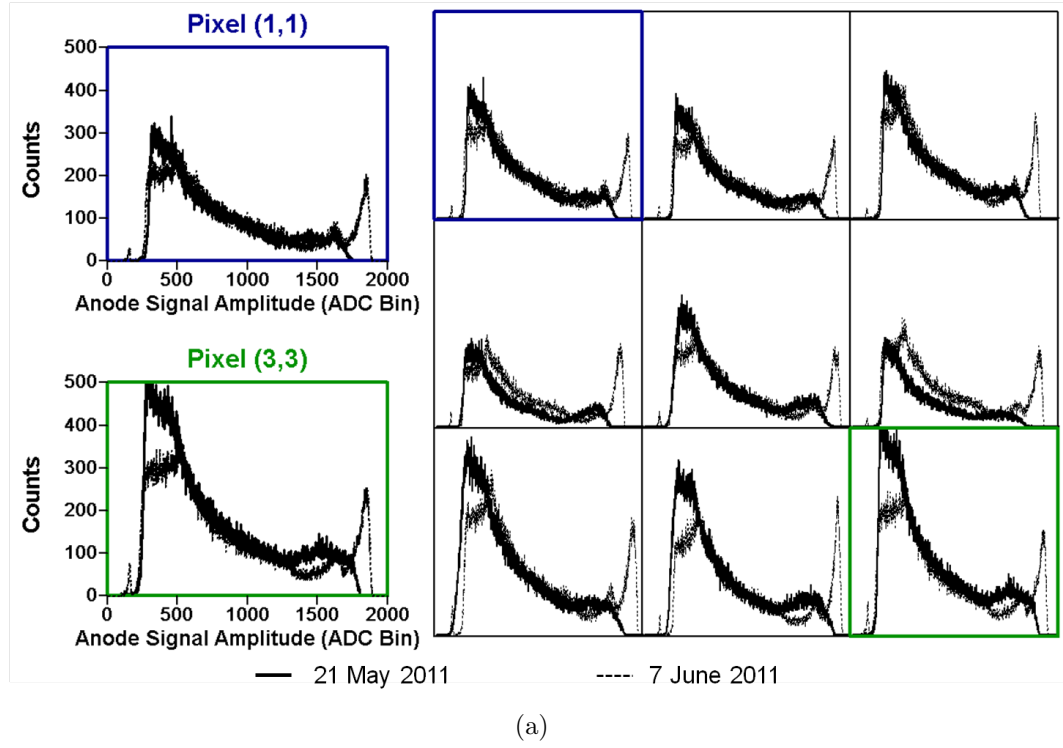
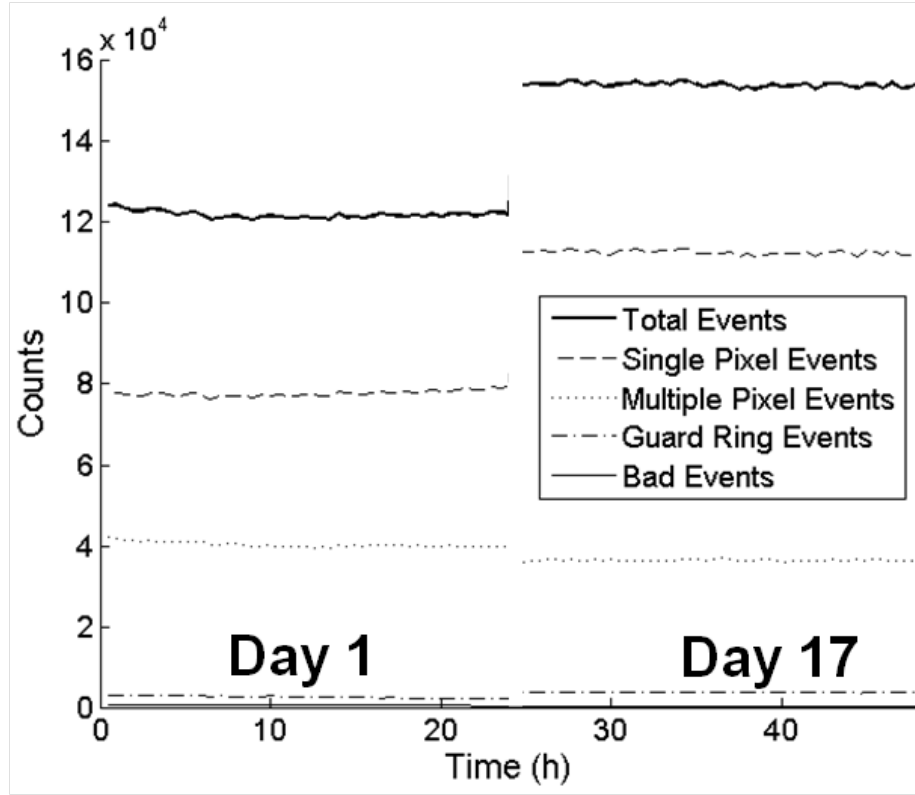
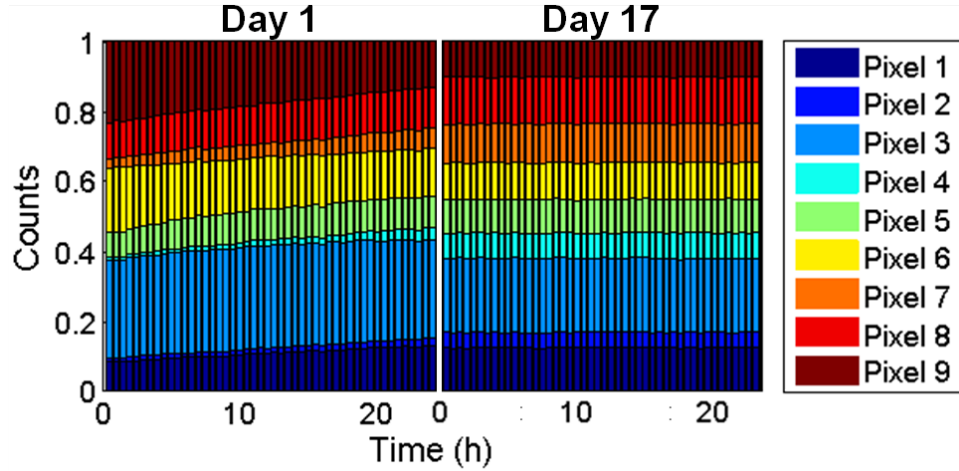


Figure 5.5: (a) The signal amplitude and photopeak efficiency increased as detector 935-16B1L stabilized. (b) The 3D spectrum for the best performing pixel, pixel 8, shows the spectrum changes most near the cathode side. Similar poor performance at depths away from the anode was observed in all pixels. Both measurement times are the same for comparison.



(a)



(b)

Figure 5.6: Event classification for the first 24-hour measurement and a 24-hour measurement after detector 935-16B1L stabilized shown together on the same plots. (a) Between the two measurements, the total number of events as well as the single-pixel events increase while the number of multiple pixel events decreases. (b) The contribution of each pixel to single-pixel events becomes relatively constant in the detector's stable state.

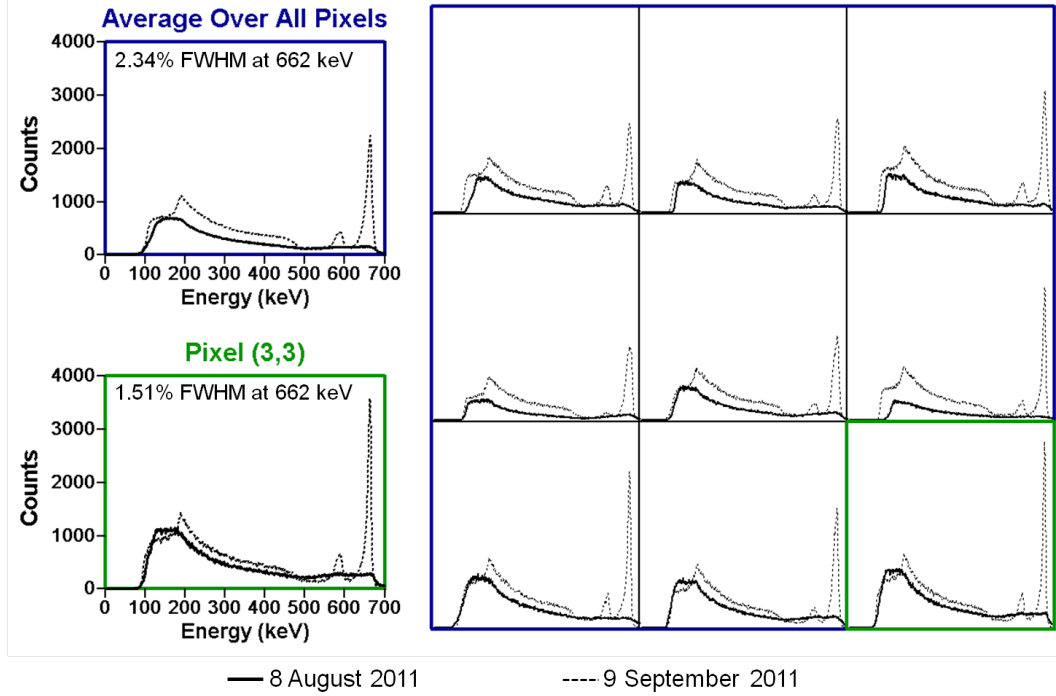


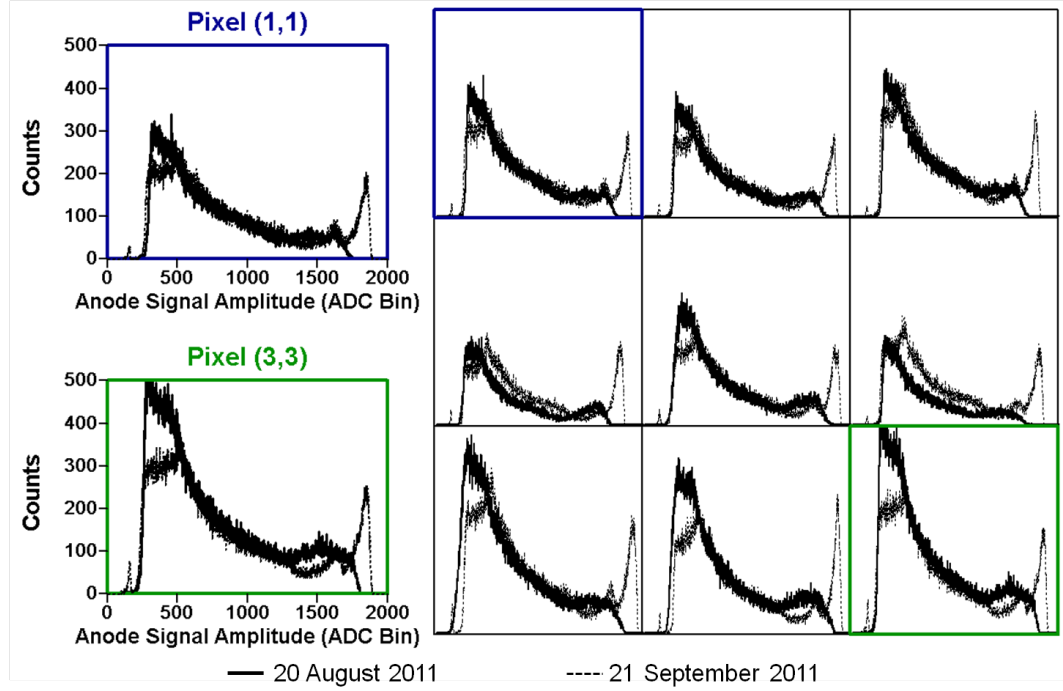
Figure 5.7: In the first measurement, the energy resolution was not measurable and improved significantly by the second measurement for detector 44B2L. Both measurement times are the same for comparison.

5.2 Discussion

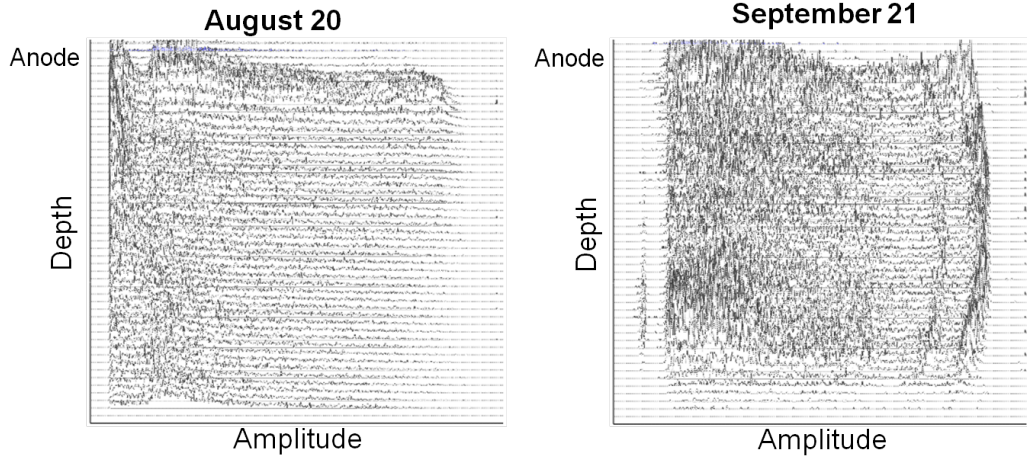
Vacancies exist in TlBr and are formed either by Schottky pairs or by compensating the impurity concentration to maintain charge neutrality. From the relationship in equation 2.14 and reference [65] and [62], the ionic conductivity at -20°C is non-zero. Therefore, it is possible to have some initial distribution of vacancies that will conduct to electrodes under the influence of an applied electric field.

Assuming a constant mobility*, the depth-dependent electric field may be estimated from the electron drift velocity. From equation 5.1, the charge density may then be estimated from the derivative of the electric field. Figures 5.17(a) and 5.17(b) show negative charge building up near both electrodes in detectors 70BA1L and 70BA1R. The high concentration of negative charge on the cathode side could be due to the creation of a p-n junction. Negatively charged thallium vacancies will conduct to the

*Published electron mobility values range from $20\text{ cm}^2/\text{Vs}$ to $40\text{ cm}^2/\text{Vs}$ [14, 71, 72].

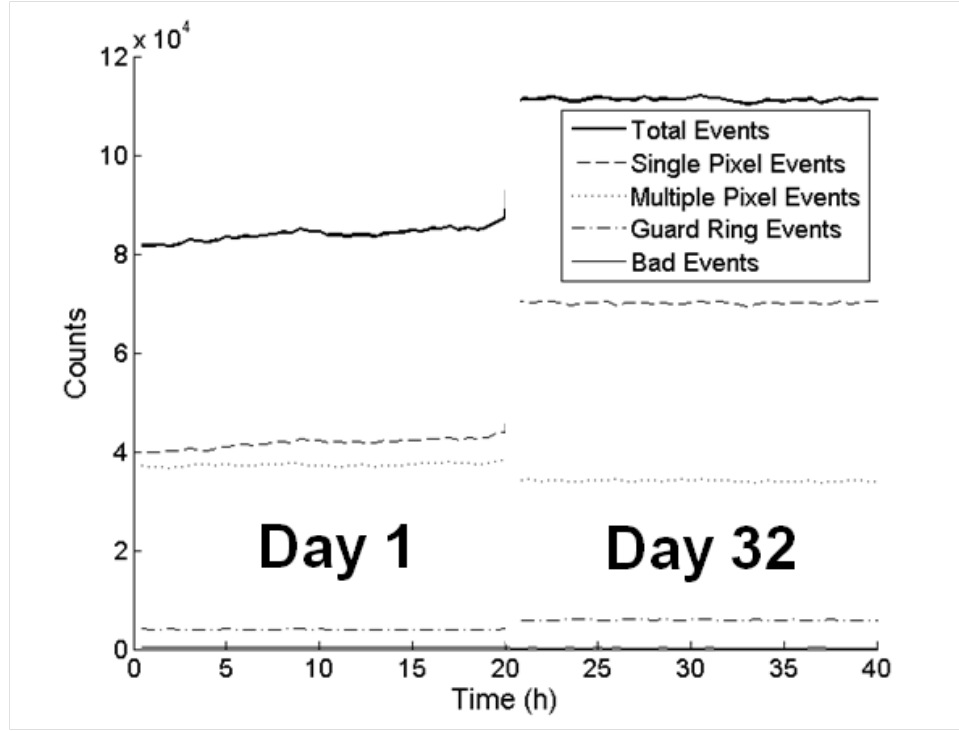


(a)

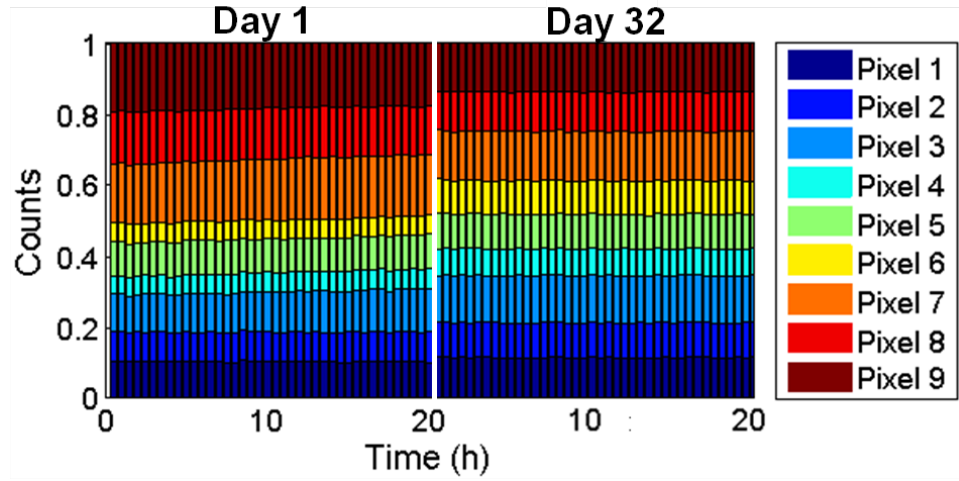


(b)

Figure 5.8: (a) The signal amplitude and photopeak efficiency increased as detector 44B2L stabilized. (b) The photopeak is not initially present in most depths, but is clearly present in all depths after the detector stabilizes. Similar poor performance at depths away from the anode was observed in all pixels.

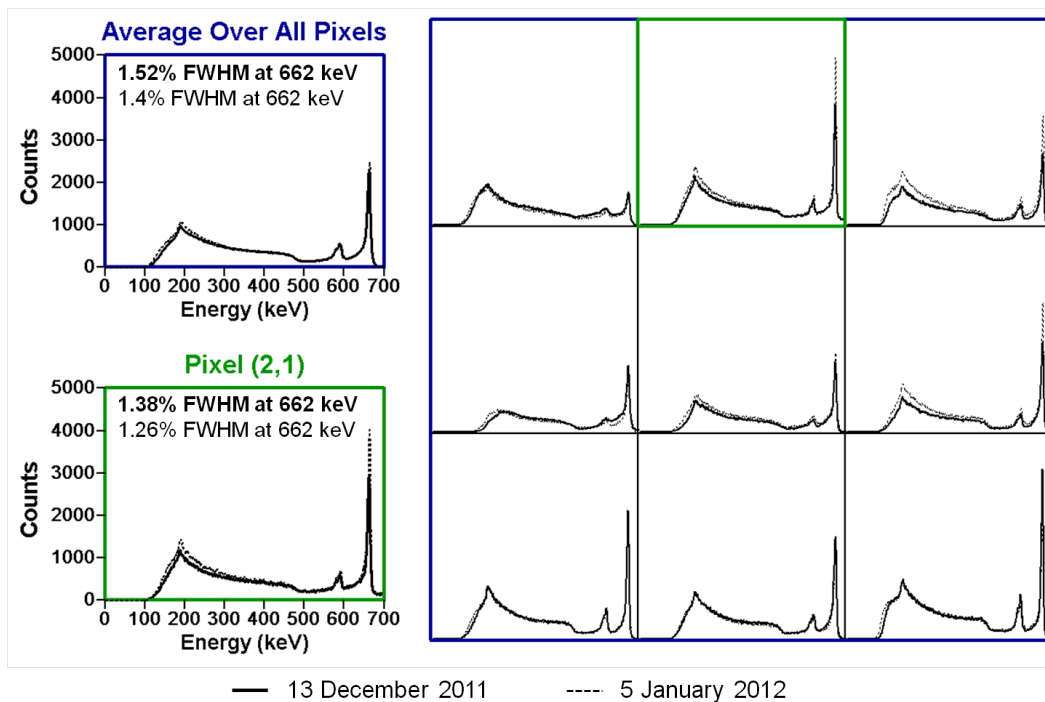


(a)

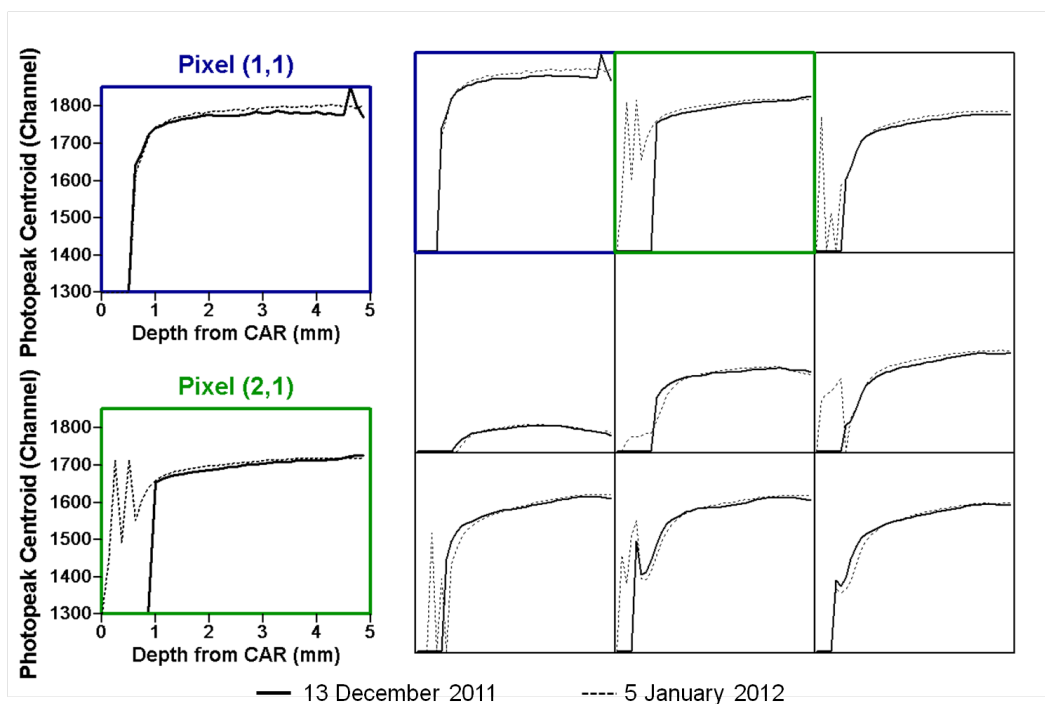


(b)

Figure 5.9: Event classification for the first 20-hour measurement and an 20-hour measurement after detector 44B2L stabilized. (a) The total events increased as the signal gain also increased. The fraction of single pixel events increased by approximately 15% of the total counts while the fraction of multiple pixel events decreased by approximately 15%. (b) The contribution of each pixel to processed single-pixel events becomes more uniform and constant, but shows less change during this transition phase than other detectors tested.

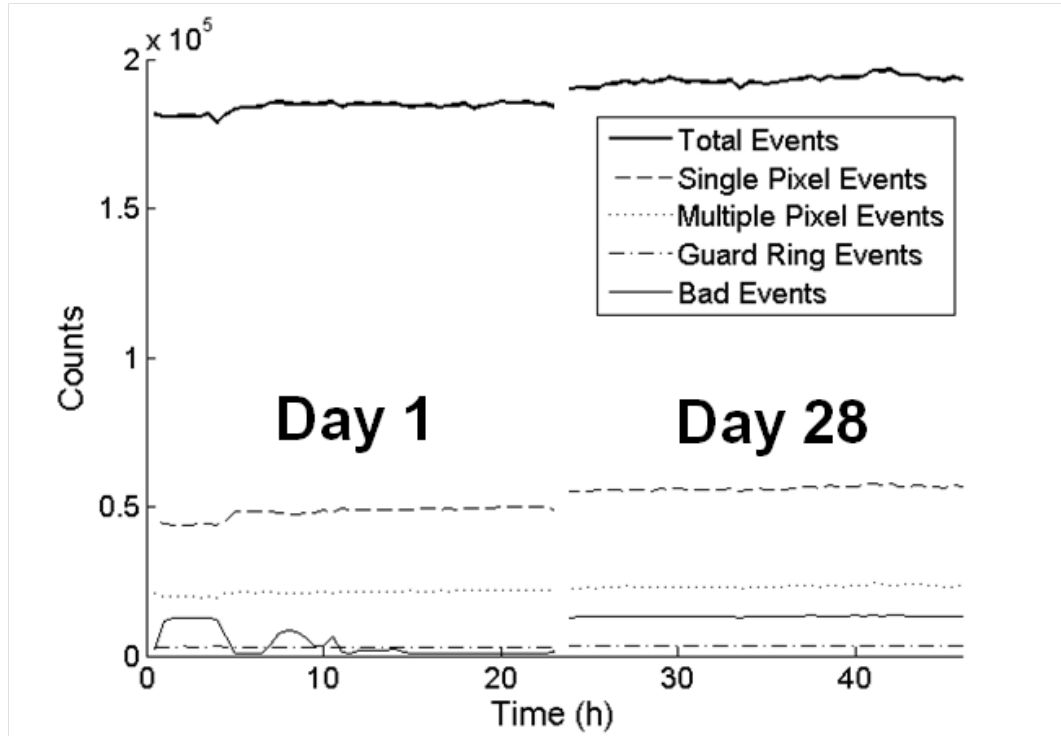


(a)

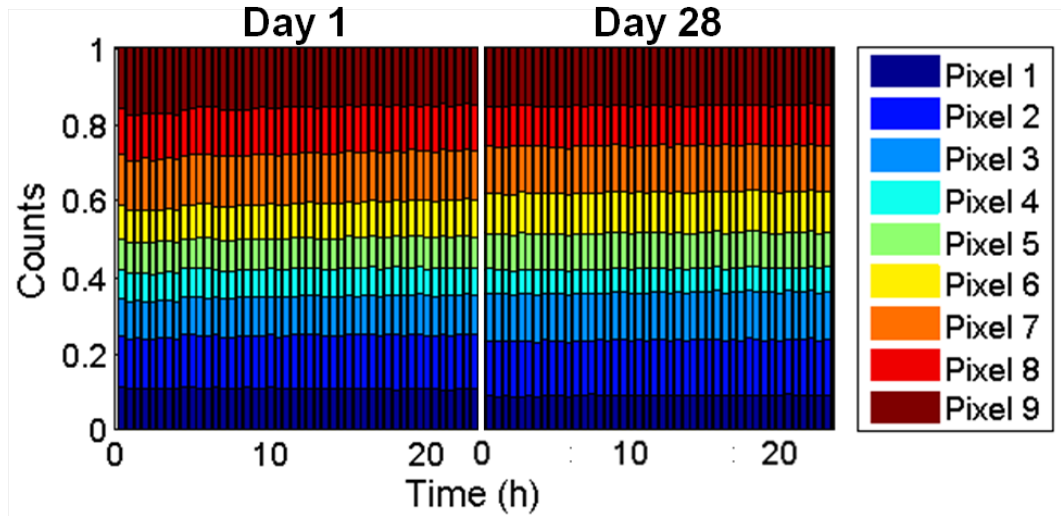


(b)

Figure 5.10: (a) The spectroscopic performance for detector 70BA1R did not show a significant change. (b) Because the spectroscopic performance was good in both measurements, the depth-dependent photopeak data are useful for comparison. The photopeak centroid increased slightly after the detector stabilized.



(a)



(b)

Figure 5.11: (a) The total counts and change in event classification for detector 70BA1R remained relatively constant after almost one month of normal operation. (b) The distribution of the single-pixel contribution by pixel also shows little change.

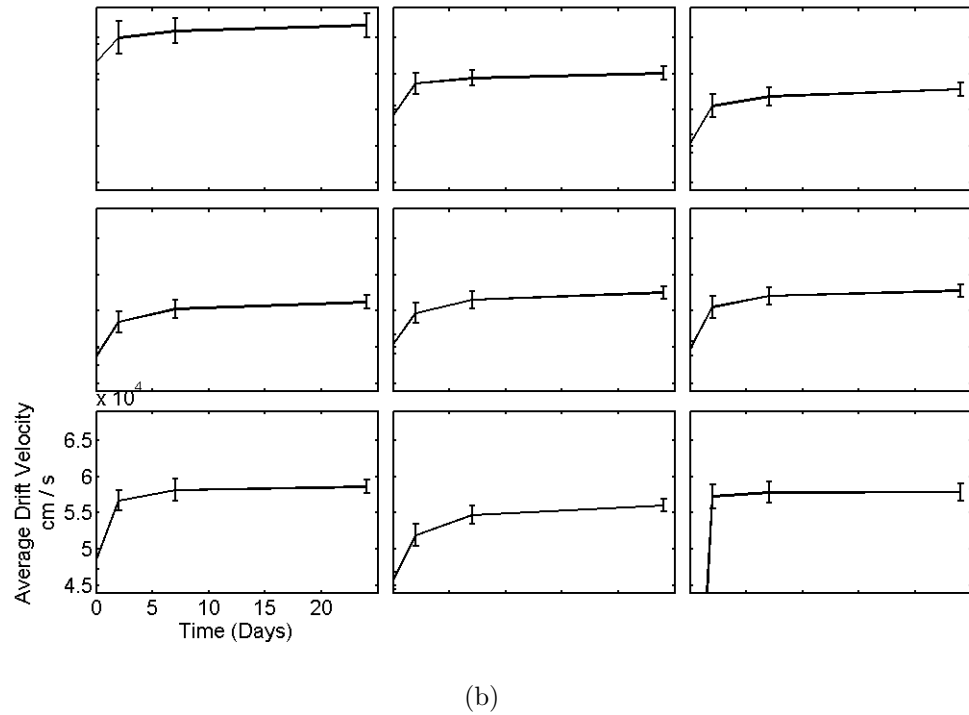
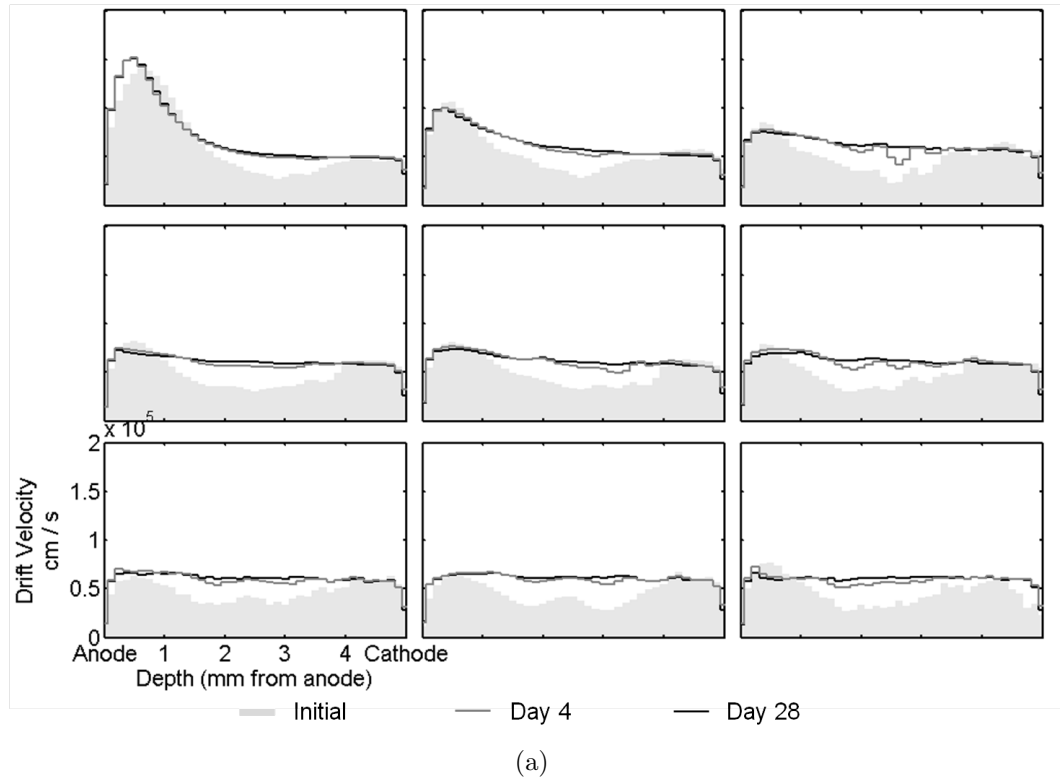


Figure 5.12: (a) Detector 70BA1R experienced a less drastic change in electron drift velocity than detector 70BA1L; however, the electron drift velocity also became more uniform as the detector stabilized. (b) The average drift velocity also increased similar to detector 70BA1L.

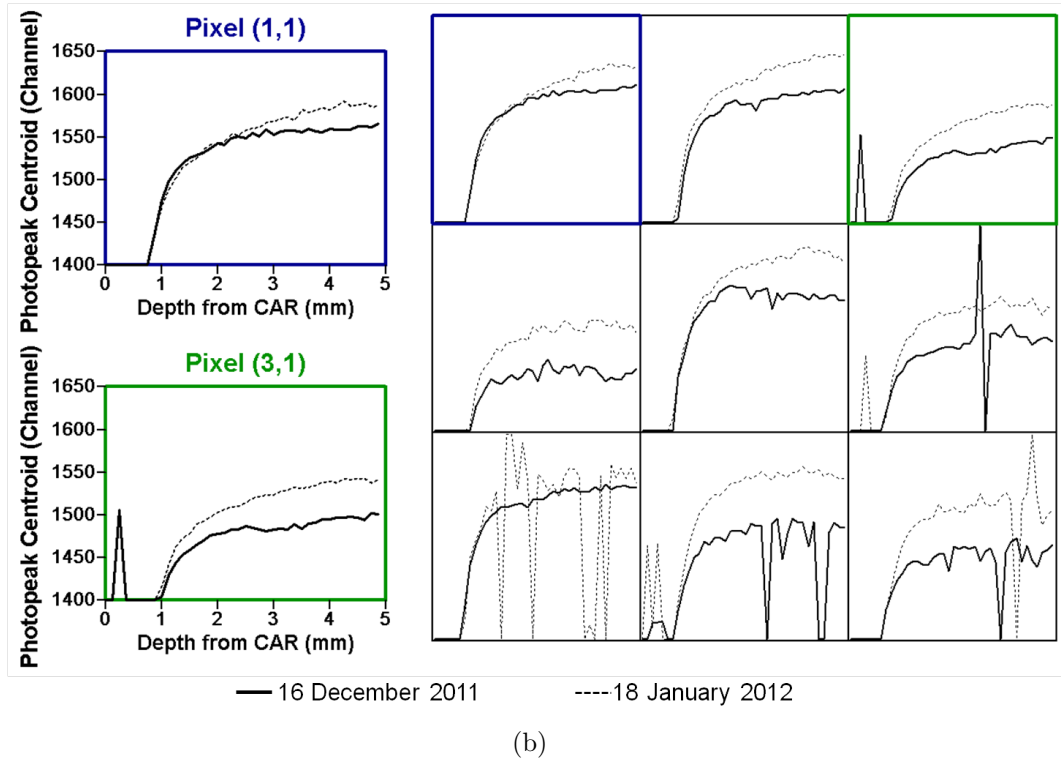
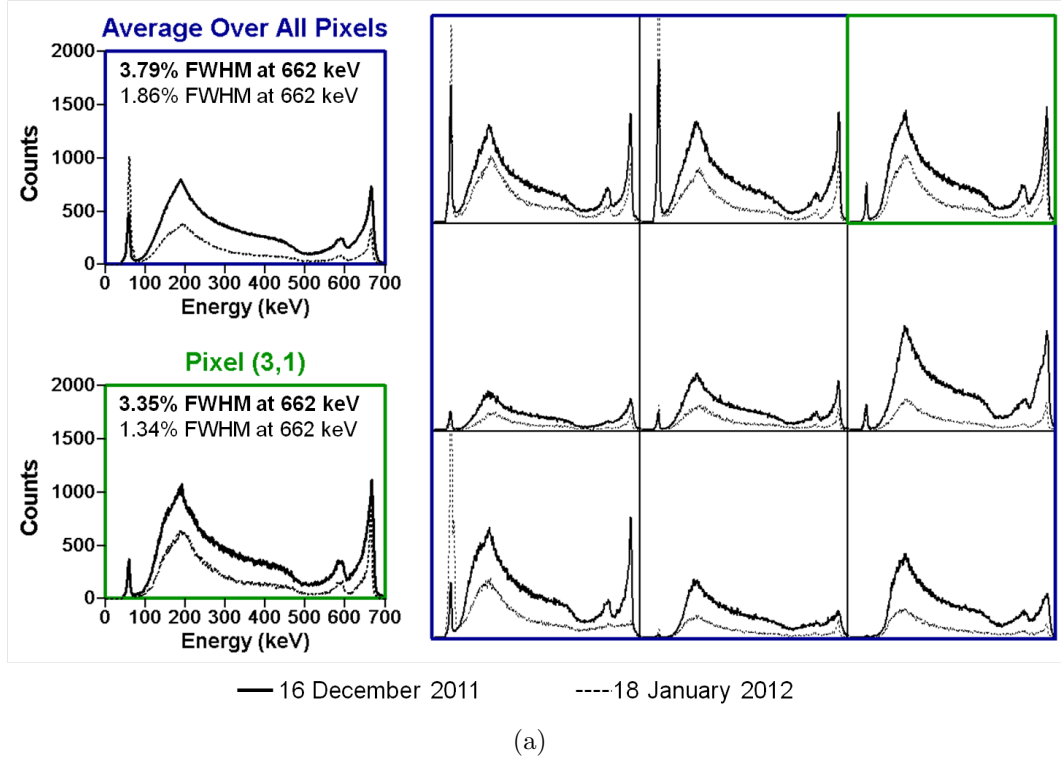
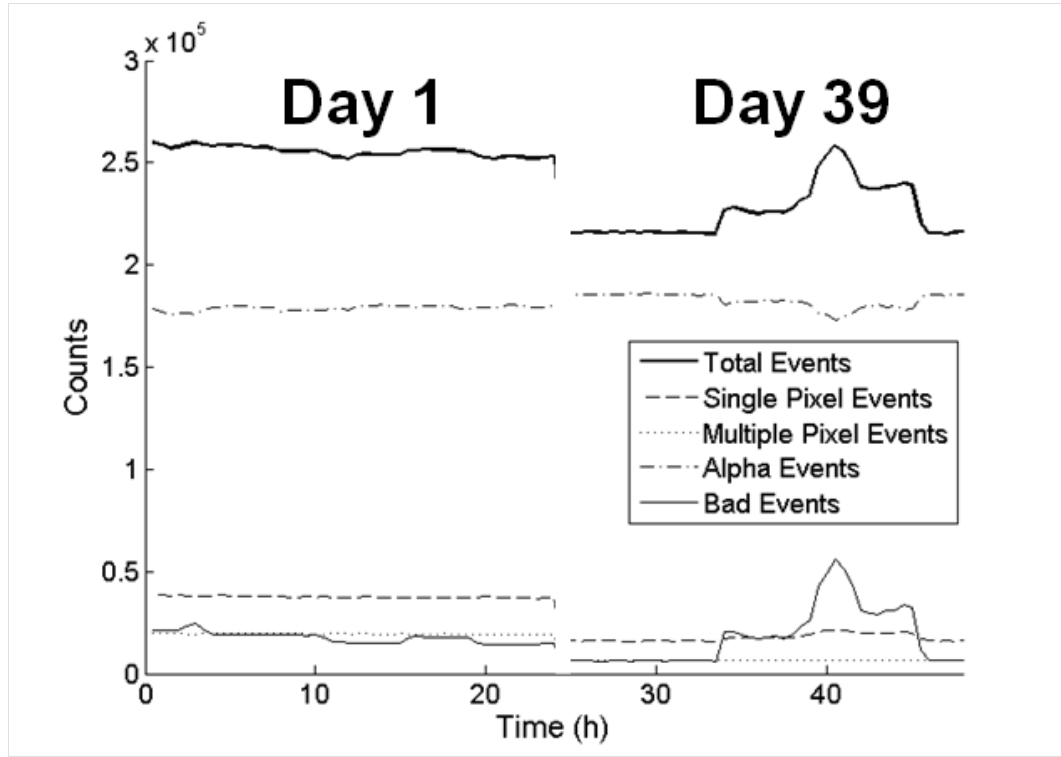
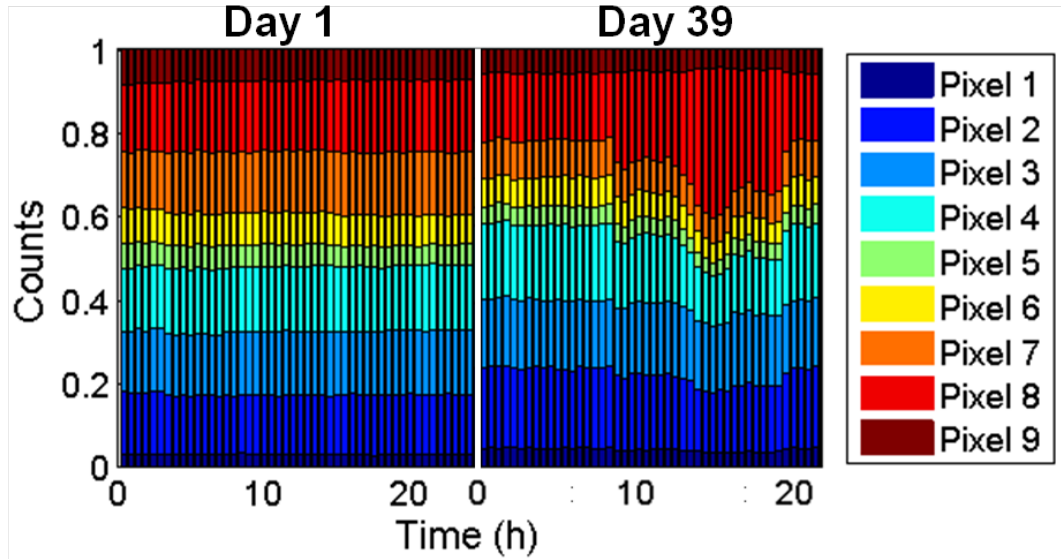


Figure 5.13: (a) The energy resolution improved on the best pixel and overall for detector 70BA1L, but the efficiency appears to degrade, possibly due to an accidental change in source geometry. (b) The photopeak centroid increased in every pixel between measurements.

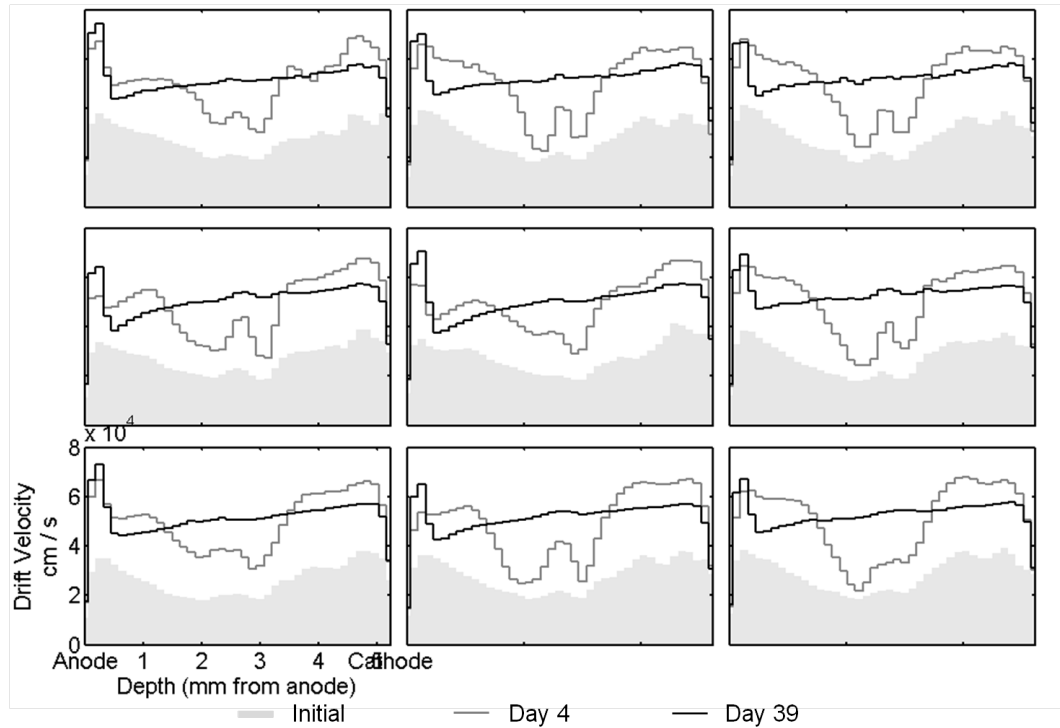


(a)

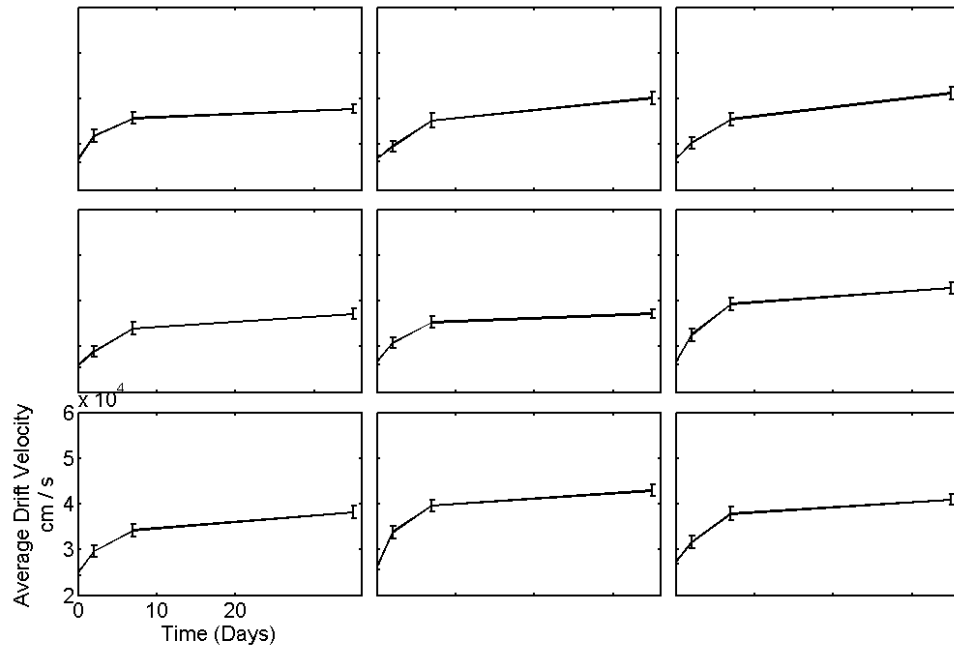


(b)

Figure 5.14: (a) The total counts decreased in the later measurement for detector 70BA1L. The instability is likely due to changes in the electronic noise during the measurement. (b) The distribution of the single-pixel event contribution by pixel also shows pixel 8 received a large portion of the counts during the unstable period.

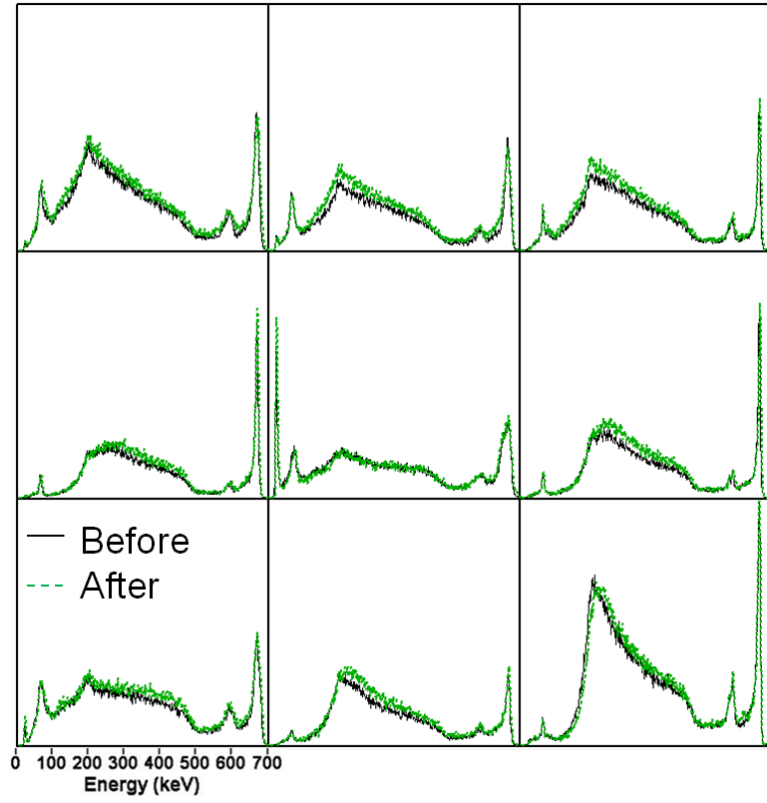


(a)

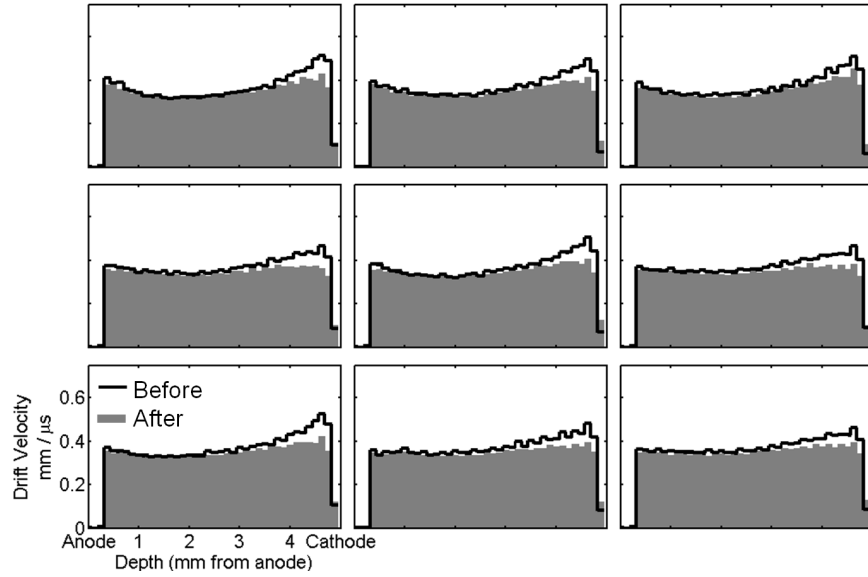


(b)

Figure 5.15: (a) Weaker drift velocity is initially observed in the central depths of detector 70BA1L. During the conditioning phase, the drift velocity increases in the central depths and eventually becomes more uniform over all depths. (b) The average drift velocity increases as the detector stabilizes.



(a)



(b)

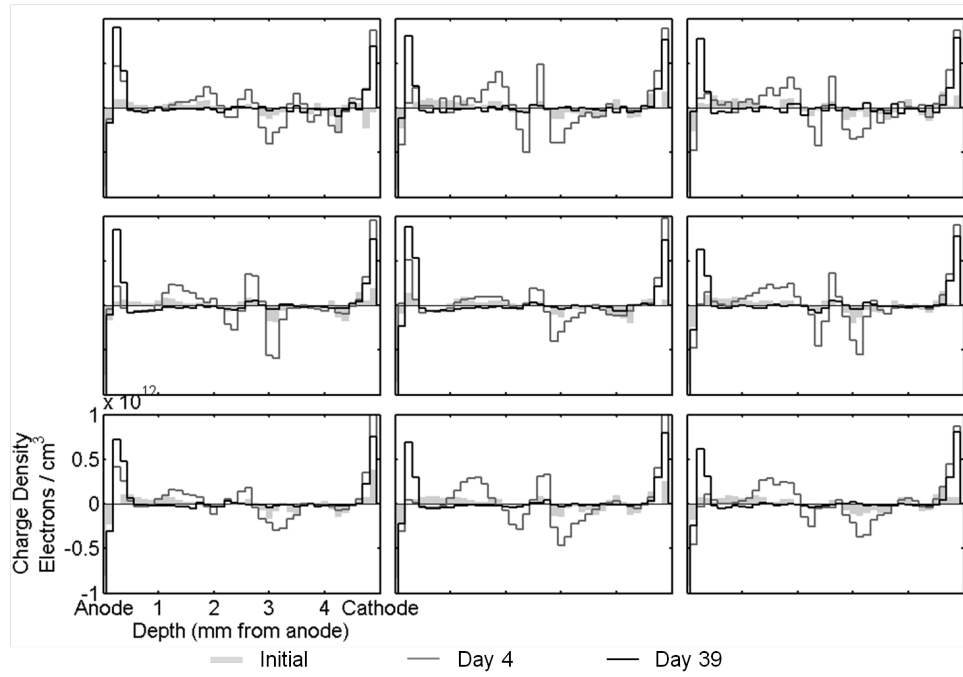
Figure 5.16: (a) The spectrum characteristics remained relatively constant for detector 47AR(R). The overall corrected energy resolution degraded slightly from 1.75% to 1.89% FWHM at 662 keV. (b) The drift velocity remained relatively uniform throughout the duration of the measurement.

anode which would create a high concentration of negative charge on the anode side.

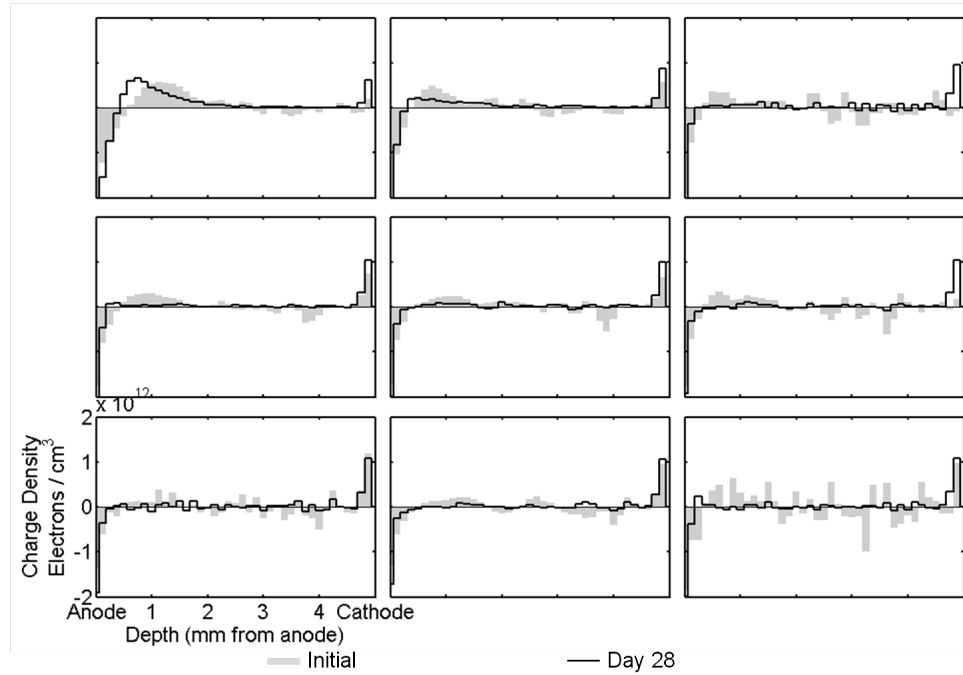
$$\frac{d^2\phi}{dx^2} = -\frac{\rho(x)}{\epsilon} \quad (5.1)$$

5.3 Summary

Transient behavior was observed in some TlBr detectors immediately following bias, but one TlBr detector tested in this work demonstrated stable behavior for the duration of its operation. Three detectors demonstrated a significant improvement in spectroscopic performance and shared similar conditioning behavior. The remaining two detectors did not experience dramatic changes in their spectroscopic performances. However, the depth profiles of their electron drift velocities did exhibit similar changes and increased on average over time. These observations show both the current need to condition some TlBr detectors before stable operation is possible and the potential to ultimately fabricate devices in way that eliminates the initial transient behavior.



(a)



(b)

Figure 5.17: Charge density as a function of detector depth for detectors (a) 70BA1L and (b) 70BA1R. The y-axis represents electrons per unit volume such that positive values represent negative charge. As the detectors stabilize, negative charge becomes more concentrated at the electrodes.

CHAPTER VI

Characterization of Room Temperature Operation

Polarization as it relates to radiation detectors is generally defined as any time-dependent change in performance, but is a ubiquitous term which takes on various meanings depending upon the detector material. In CdTe and HgI₂, polarization describes reversible degradation in detection efficiency and energy resolution [73, 74]. For TlBr, however, polarization implies performance degradation and eventually complete irreversible failure that occurs during normal detector operation at room temperature. The contents of this chapter describe the characteristic behavior of polarization in TlBr and discusses the possible physical processes which could cause polarization.

6.1 Methods

Both alpha and gamma-ray measurements were taken at room temperature in order to characterize the polarization process. The experimental setup is described in Chapter III. Data acquisition for each detector began immediately following application of -1000 V cathode bias at room temperature. A 100 μ Ci ¹³⁷Cs gamma-ray source was measured to evaluate the change in spectroscopic performance and detector efficiency. Alpha particle data show how the electron drift velocity changes as the detector polarizes. During data post-processing, events above a cathode signal amplitude threshold were written to a separate file for alpha-particle waveform anal-

ysis. The threshold was detector-dependent and was determined from the alpha peak location in the cathode spectrum. Alpha waveforms were analyzed using the methods described in section 3.3.3.

6.2 Results

Because each detector behaved differently during polarization, the results are presented on a case-by-case basis. Due to their short time to failure after cathode bias application, detectors 70BA1R and 70BA1L have limited gamma ray data. The gamma-ray data are plentiful for detector 47AR(R) which failed after three months at cathode bias. Alpha data were sufficient for all detectors.

6.2.1 Detector 70BA1R

A 100 μCi ^{137}Cs source flood irradiated the detector during room temperature operation. Stable data measured at -20°C prior to room temperature operation were used to calibrate one-hour measurements of the room temperature data shown in Figure 6.1. For reference, stable characteristics for this detector are described in Chapter IV.

The total number of single-pixel events shown in figure 6.1 decreased by $38.1 \pm 0.2\%$ after 20 hours and by $82.0 \pm 0.1\%$ after 24 hours. Figure 6.2 shows the total counts decrease uniformly as a function of depth. During the data processing procedure described in section 3.3.1, events are filtered such that only single pixel events are processed. Between hour zero and hour 21, the total number of events recorded is roughly constant, while the number of single pixel events is slowly replaced by multiple pixel events and events in which zero pixels passed the interaction threshold (figure 6.3). The number of events passing the alpha event threshold also decreases due to the increase in classified multiple pixel events and bad events*. After hour

*Events caused by noise triggers rather than radiation interactions are classified as bad events.

21, the total number of events increases dramatically as the detector becomes more unstable.

The gradual increase in multiple pixel events can be explained by the decreasing electron drift velocity in figure 6.4. These data from the alpha particle irradiation reveal how the drift velocity uniformly decreases in most depths as the detector polarizes, causing the overall average drift velocity to decrease as shown in figure 6.5. As the electron drift velocity decreases, the charge cloud size increases as a result of diffusion according to the relationship in equation 6.1, where σ is the standard deviation of the charge arrival position, k_B is Boltzmann's constant, T is the absolute temperature, x represents the drift distance, e is the elementary charge, and \mathcal{E} is the electric field magnitude. The electric field magnitude is also defined by equation 2.7; therefore, the size of the charge cloud may be estimated from the average electron drift velocity shown in figure 6.5 (equation 6.2).

$$\sigma = \sqrt{\frac{2k_B T x}{e\mathcal{E}}} \quad (6.1)$$

$$\sigma = \sqrt{\frac{2k_B T x \mu_e}{e v_e}} \quad (6.2)$$

According to the relationship in equation 2.7, the changing drift velocity could be caused by a changing electric field or a change in the electron mobility. Assuming the mobility remains constant, the electron drift velocity is proportional to the electric field. Data from the detector's stable condition (described in section 4.3.1) and the relationship in equation 3.4 provide an estimate of 30 cm²/Vs for the electron mobility[†]. From this mobility estimate, the electron cloud size is estimated in figure 6.6. The increase in charge cloud size increases the number of charge sharing events, which are classified as multiple pixel events and discarded.

[†]Published electron mobility values range from 20 cm²/Vs to 40 cm²/Vs [14, 71, 72].

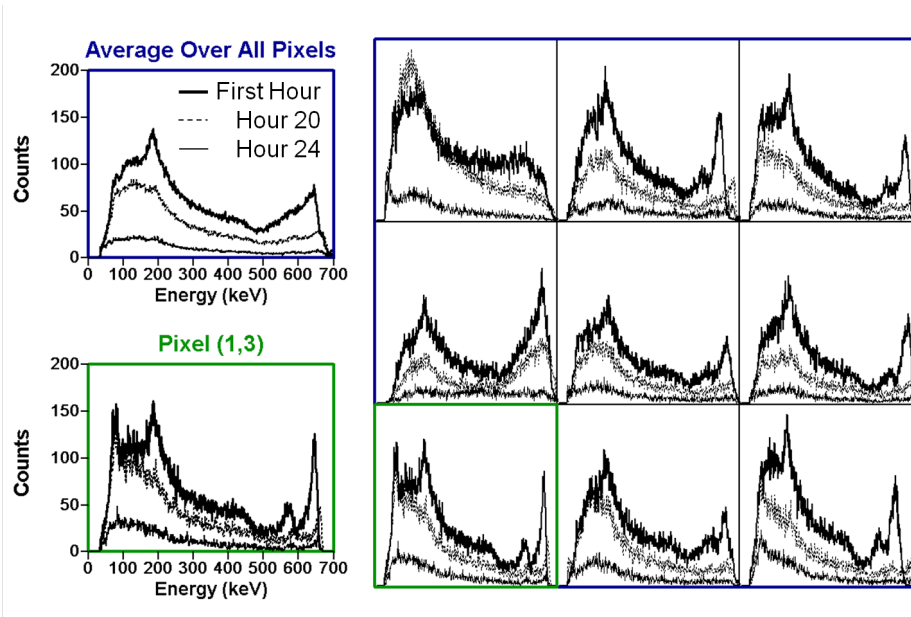


Figure 6.1: Depth-corrected Cs^{137} spectra for the first hour of room temperature operation compared to hours 20 and 24. Data measured at -20°C prior to the room temperature measurement were used to calibrate these data.

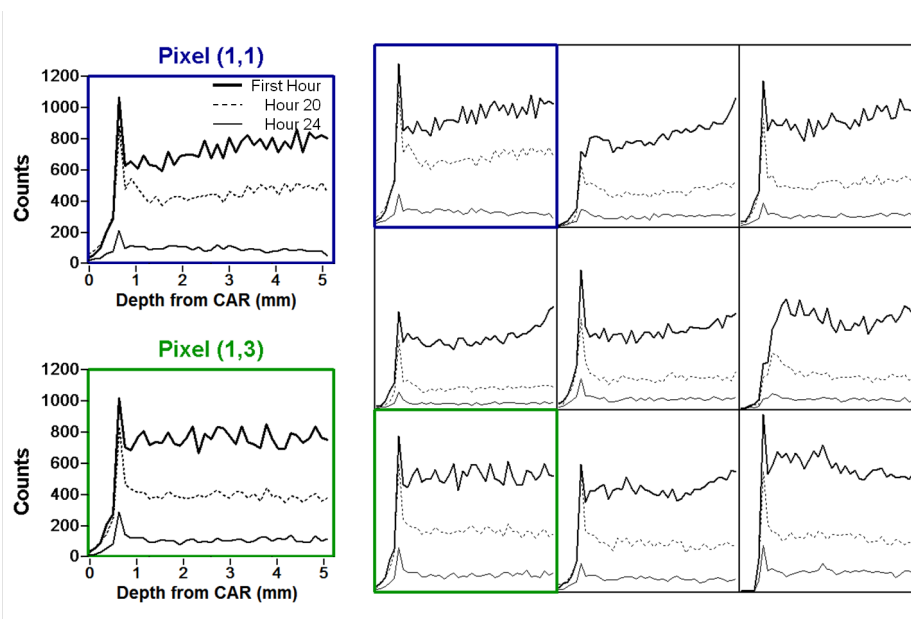


Figure 6.2: Total counts as a function of depth for the first hour of room temperature operation compared to hours 20 and 24. Data measured at -20°C prior to the room temperature measurement were used to calibrate these data.

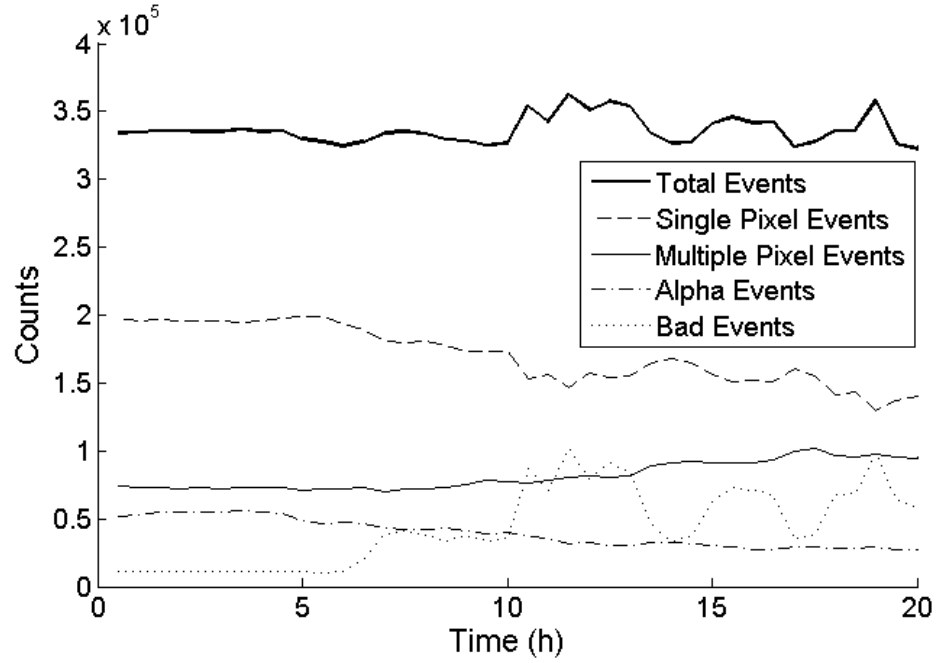


Figure 6.3: Change in event classification as a function of time for detector 70BA1R.

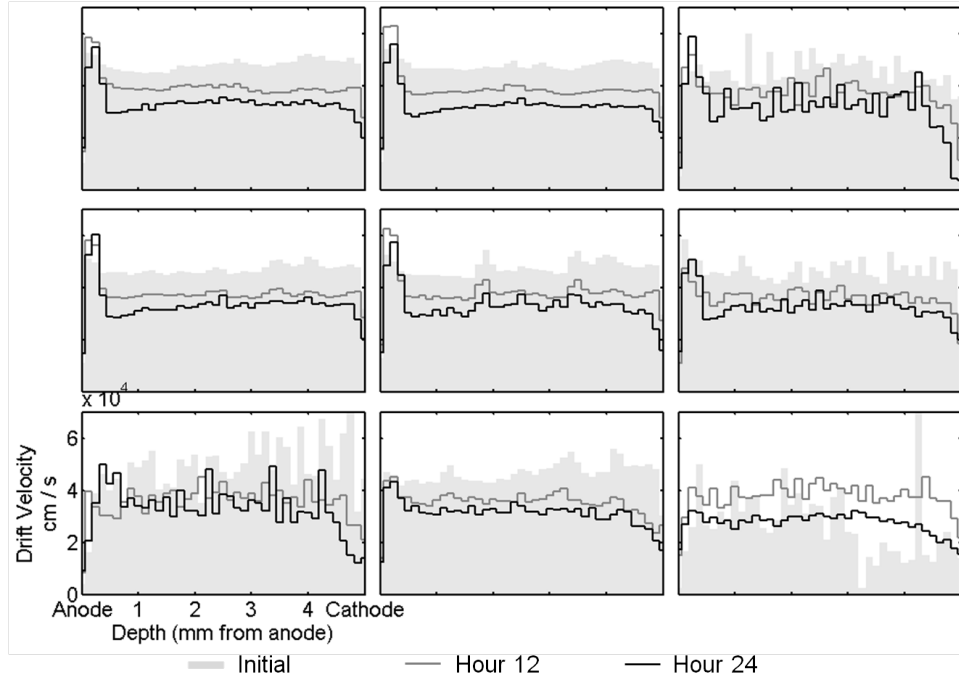


Figure 6.4: Drift velocity as a function of depth calculated from ^{241}Am alpha particle waveforms. The drift velocity uniformly decreases in most depths as the detector polarizes. The drift velocity increases near the anode side as the detector polarizes, possibly indicating a build up of bromine vacancies. Due to geometric constraints, pixels 1, 2, 4, and 5 are the only pixels with statistically significant alpha data.

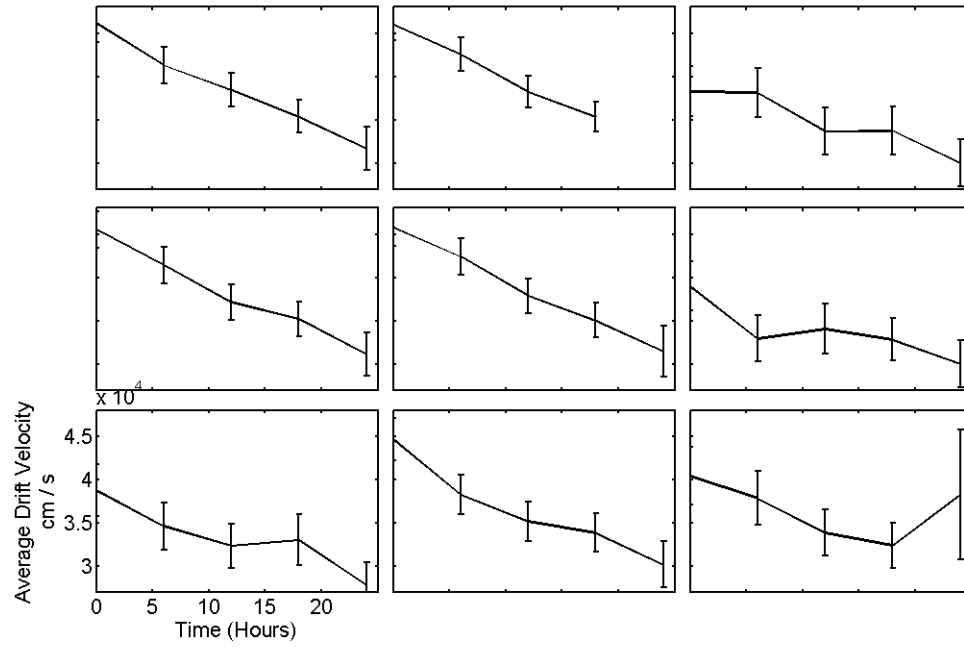


Figure 6.5: The drift velocity was averaged over all depths at each measurement time for detector 70BA1R. The average drift velocity decreased by approximately 10% from the beginning of the room temperature measurement as the detector polarized.

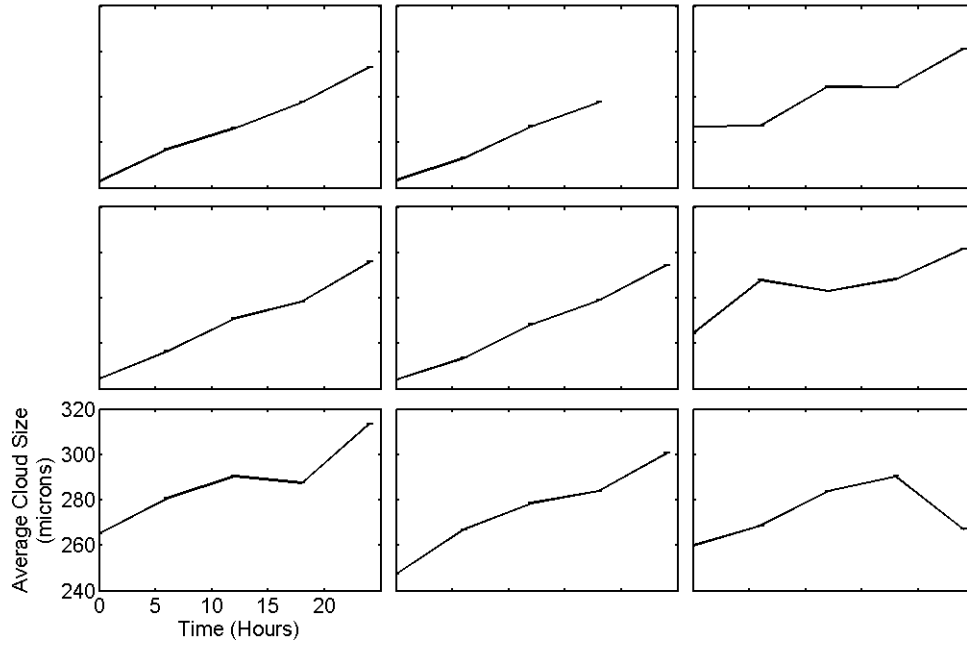


Figure 6.6: Three standard deviations of the charge arrival position calculated from cathode-side alpha events for detector 70BA1R, which includes 97% of the total charge cloud.

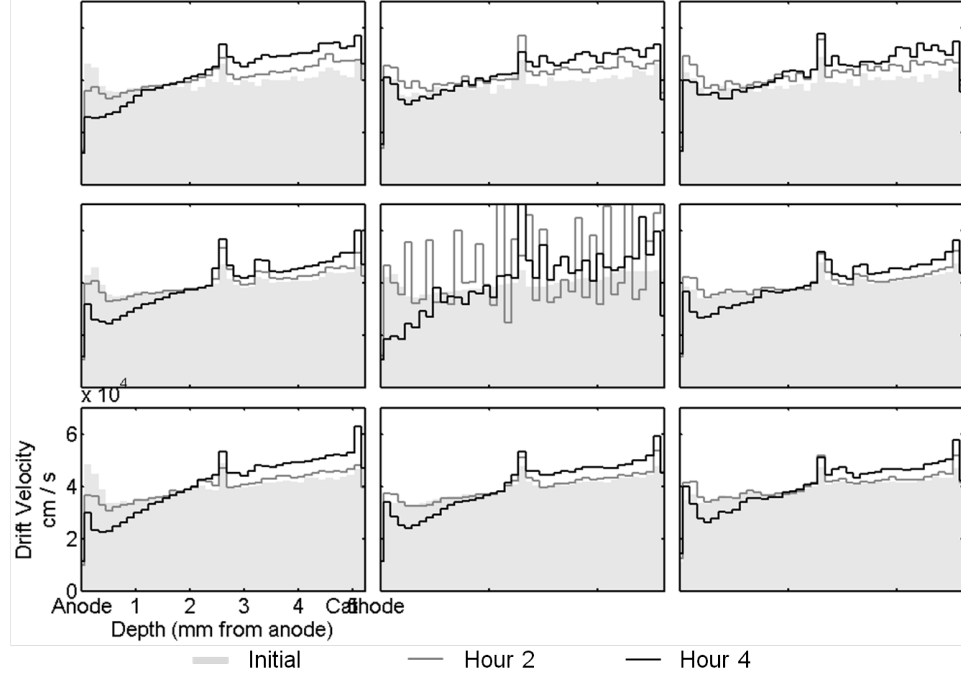


Figure 6.7: Drift velocity as a function of depth calculated from ^{241}Am alpha particle waveforms for detector 70BA1L. The drift velocity uniformly decreases in most depths as the detector polarizes. The drift velocity gradually decreases near the anode side as it increases near the cathode side. The central pixel became count starved as the detector failed.

6.2.2 Detector 70BA1L

Detectors 70BA1L and 70BA1R originated from the same location of the same ingot; however, 70BA1L failed after operating for only four hours at room temperature. Due to its relatively short duration of stable operation, the gamma data were insufficient for spectroscopic analysis. Data from the alpha particle irradiation reveal the electron drift velocity steadily increases near the cathode side as it decreases near the anode side, shown in figure 6.7, which is possibly due to a buildup of negative space charge near the anode and the cathode. Figure 6.8 shows the overall average drift velocity remains relatively constant due to the decrease in drift velocity near the anode side offsetting the increase near the cathode side. Figure 6.9 shows the total number of counts sharply increases and far fewer single pixel events are identified after breakdown occurs at four hours.

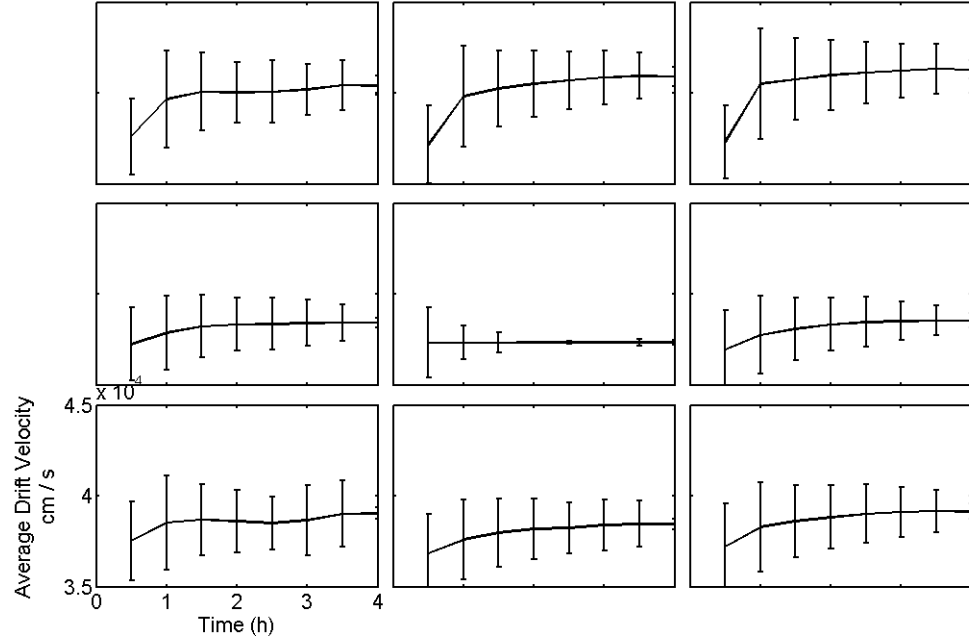


Figure 6.8: The drift velocity was averaged over all depths at each measurement time for detector 70BA1L. The overall average drift velocity initially increases in most pixels (as much as 10% in Pixel 1), and remains relatively constant throughout remainder of the measurement.

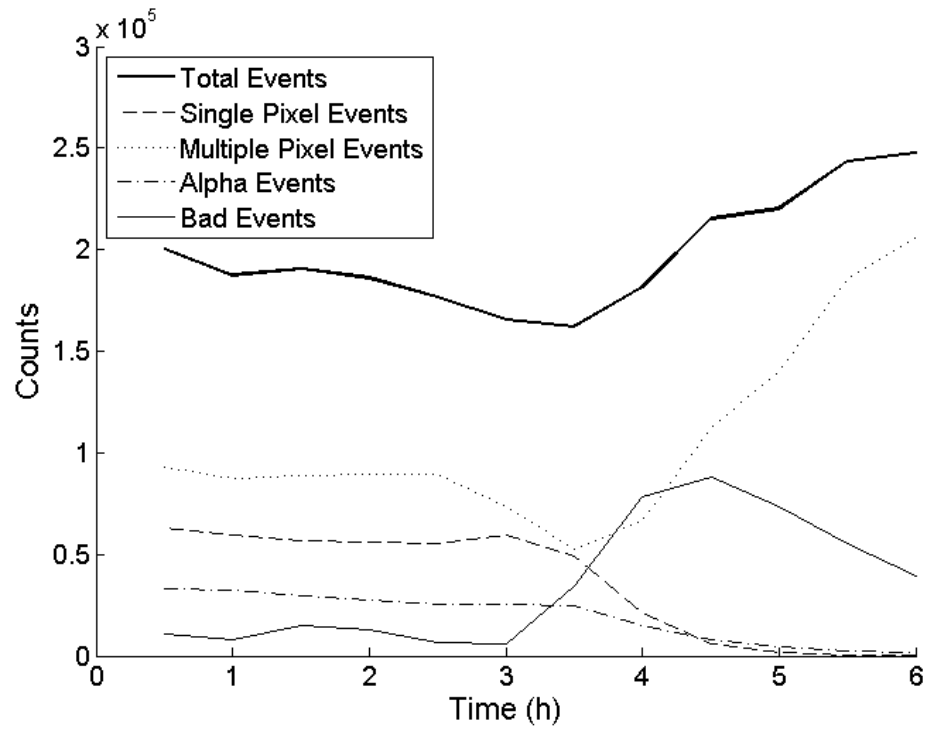


Figure 6.9: Change in event classification as a function of time for detector 70BA1L.

6.2.3 Detector 47AR(R)

Detector 47AR(R) finally failed after 87 days operating under -1000 V cathode bias at room temperature. The depth-corrected spectra in figure 6.10(a) show the detector was still useful as a spectrometer even in the final day before failure. Figure 6.12 shows a relatively large signal gain decrease in the first two weeks of room-temperature operation, and figure 6.11(a) shows the photopeak position uniformly decreased over all depths in the remaining functional pixels (pixels 2, 4, and 7). The three-dimensional spectra in 6.14(i) shows performance degradation occurring uniformly in all depths. The uniformity in amplitude shift and performance degradation indicates the anode signal loss occurred very near the anode electrode rather than the detector bulk.

A decrease in efficiency is also observed in figures 6.10, 6.11(b), and 6.16. The total counts in figure 6.16 decreased due to fewer events passing the trigger threshold as the signal amplitude decreased. The number of single-pixel events mirrored the number of multiple-pixel events in figure 6.16, so the photopeak efficiency in figure 6.11(b) decreased possibly as a result of increased classified multiple-pixel events.

The absolute value of the drift velocity would be overestimated if a dead layer formed at either the anode or cathode electrode (or both); however, the relative shape of the drift velocity as a function of depth is accurate. The electron drift velocity in figure 6.15 increased near the anode side as it decreased near the cathode side, but the overall average drift velocity decreased over time. The fraction of classified multiple-pixel events could have increased as a result of the decreased electron drift velocity.

Figures 6.10, 6.12, and 6.13 reveal signals generated on the cathode side experienced a greater signal deficit than signals produced in the bulk as the detector failed. The alpha peak in both the anode and cathode spectrum decreased similarly by approximately 40%, whereas the gamma-ray data experienced a less-significant amplitude decrease (approximately 1%). Because the gamma-rays irradiated all depths,

the insignificant change in the anode spectrum indicates the failure mechanism does not occur in the crystal bulk. Furthermore, the depth-separated spectra degraded uniformly rather than at specific depths which indicates performance degradation occurred at the anode electrode. Therefore, the alpha-particle spectrum degradation occurred at the cathode electrode.

6.3 Discussion

Figures 6.18 and 6.19 show detectors 70BA1L and 47AR(R) experienced significant physical change at the anode contact, while figure 6.17 shows detector 70BA1R's anode experienced less significant physical change after failure. Gamma-ray data for detector 47AR(R) show the degree of performance degradation corresponds with the physical change observed on the anode. A similar physical change might have occurred on the cathode, however the cathode was inaccessible. The observed physical change supports the hypothesis that thallium chemically reacts with gold contacts, catalyzing the failure process. Furthermore, the data presented in this chapter show performance degradation occurring at the electrodes rather than within the crystal bulk.

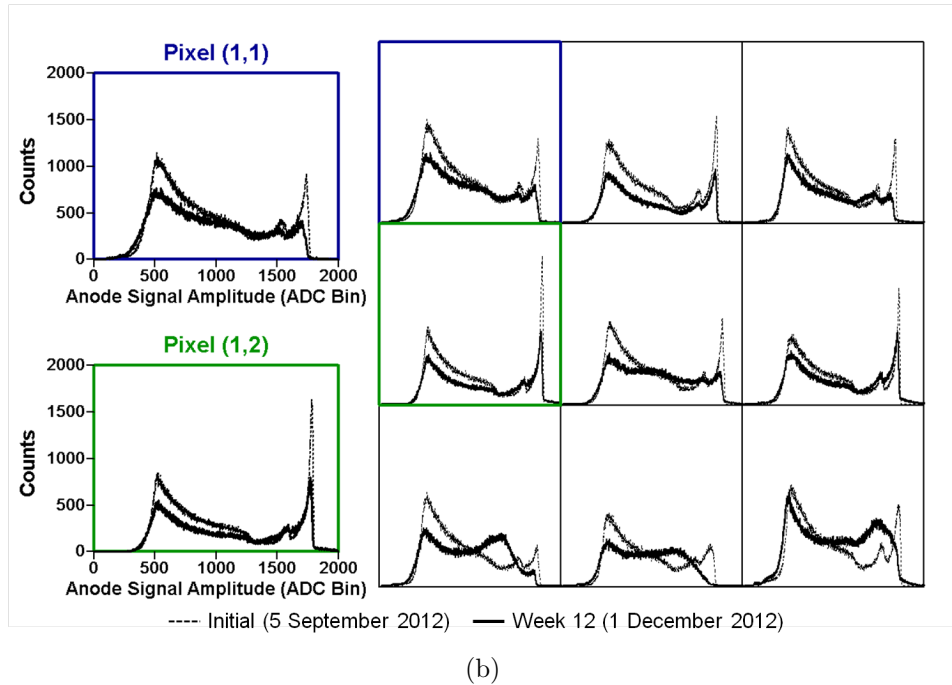
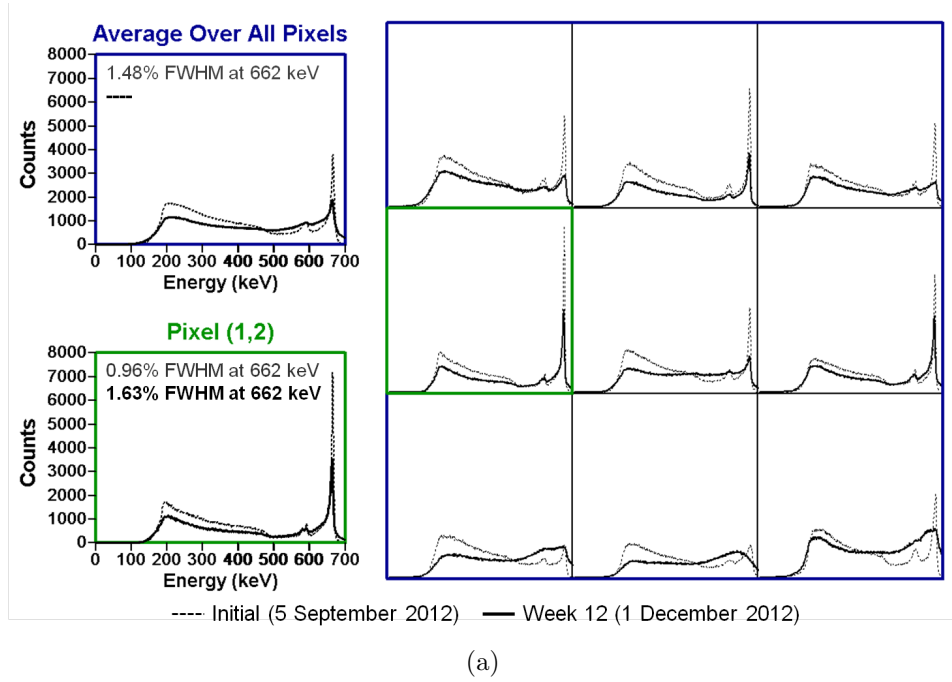


Figure 6.10: (a) Detector 47AR(R) depth-corrected spectra for the initial 24-hour measurement compared to the last 24-hour measurement. (b) The gain decreases slightly in the raw spectrum between the first and the last 24-hour measurements.

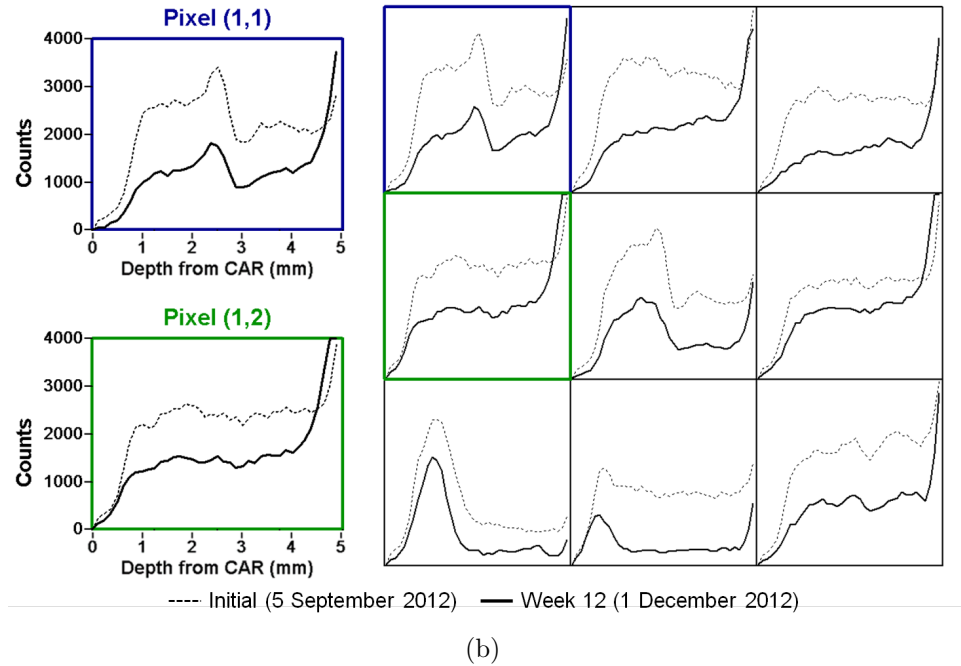
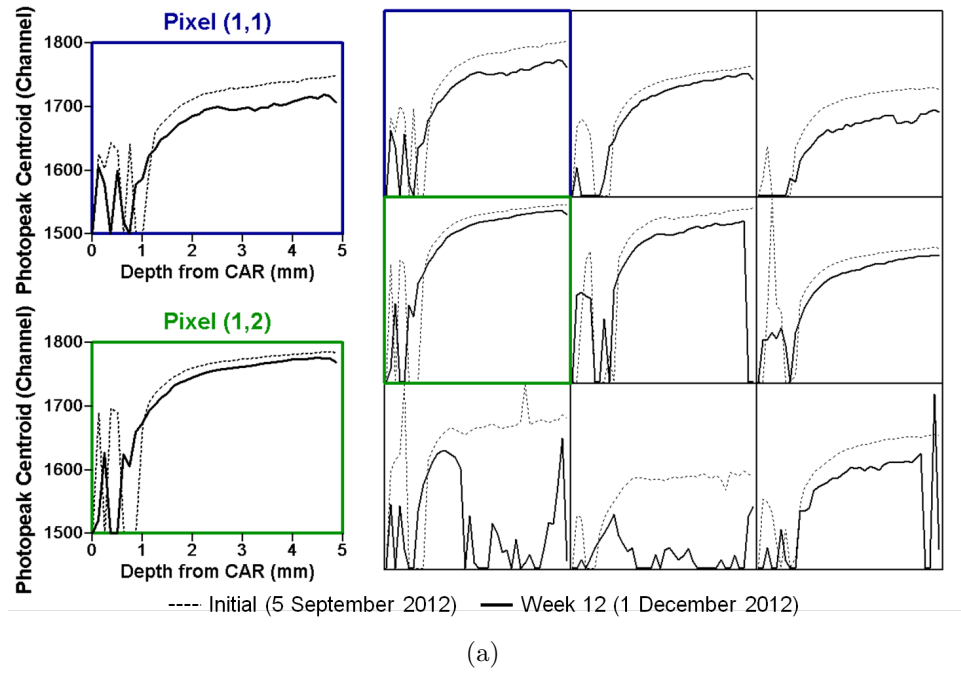


Figure 6.11: (a) The photopeak position decreases uniformly in pixels where the photopeak is still present. (b) The peak counts also decrease nearly uniformly in all depths except very near the cathode of every pixel.

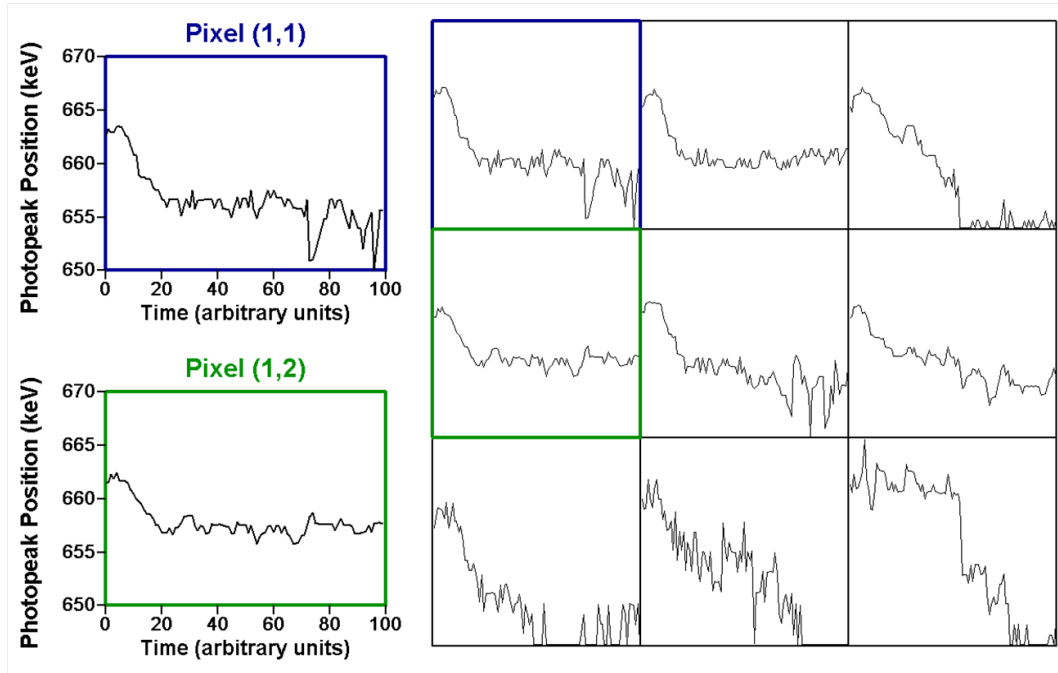
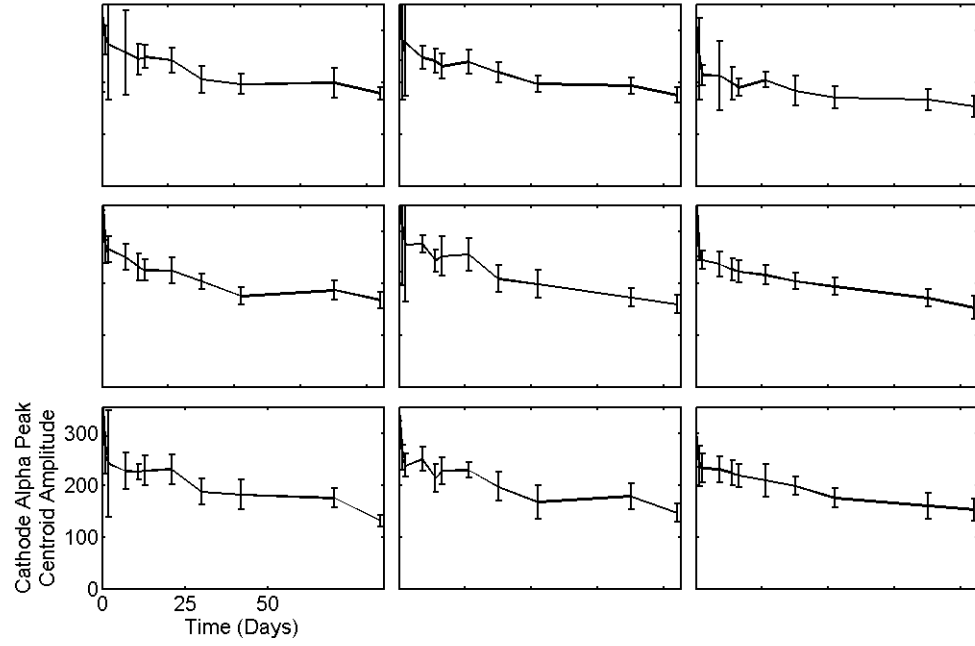
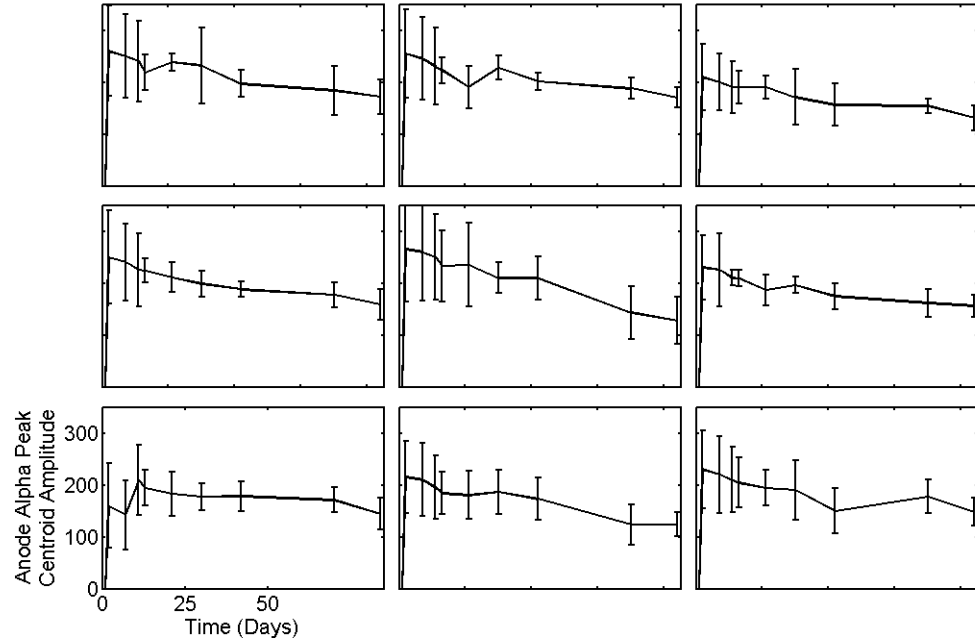


Figure 6.12: The energy-corrected photopeak position is plotted as a function of time with the 87 measurement days separated into 100 bins. The photopeak position decreased by approximately 5 keV (1%) after two weeks of room-temperature operation and remained relatively stable in the pixels with a detectable photopeak.

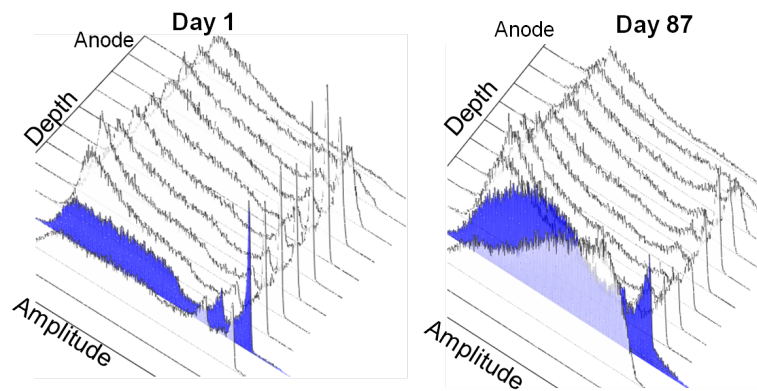


(a)

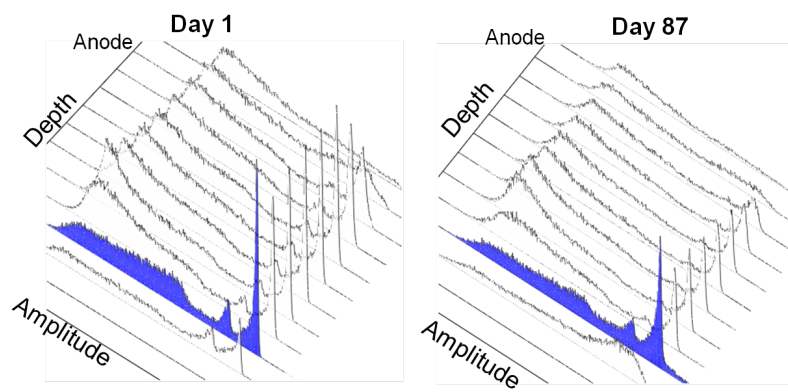


(b)

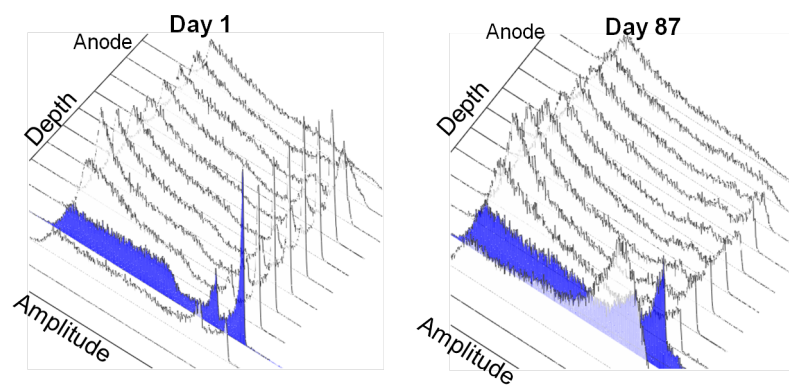
Figure 6.13: The alpha peak centroids in the (a) cathode spectrum and (b) anode spectrum similar trend with the peak position decreasing by approximately 50% by the end of the measurement.



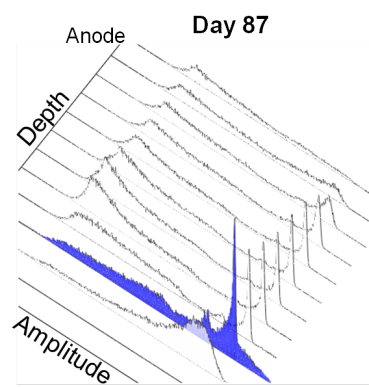
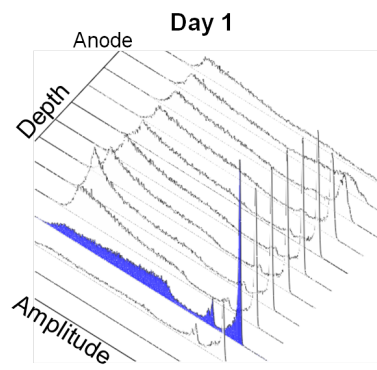
(a)



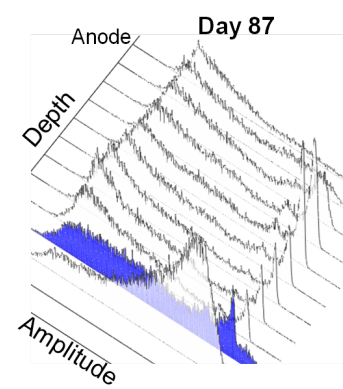
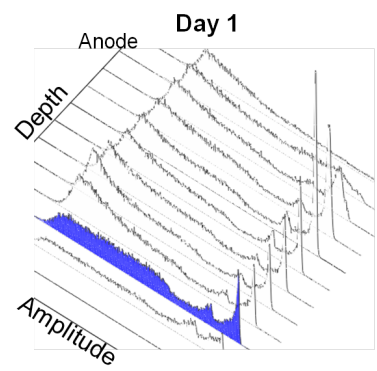
(b)



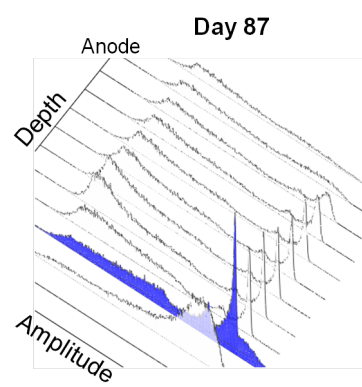
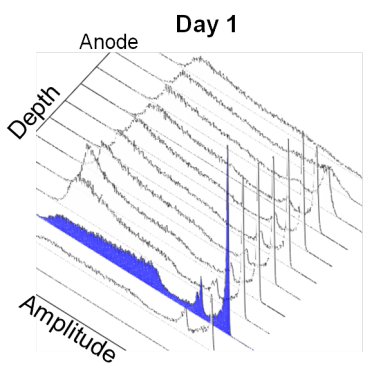
(c)



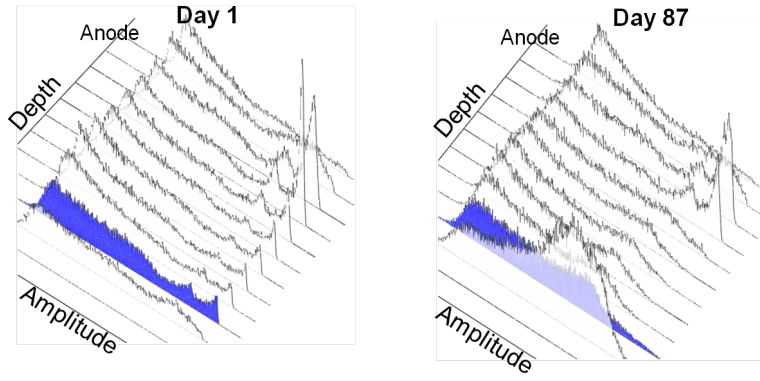
(d)



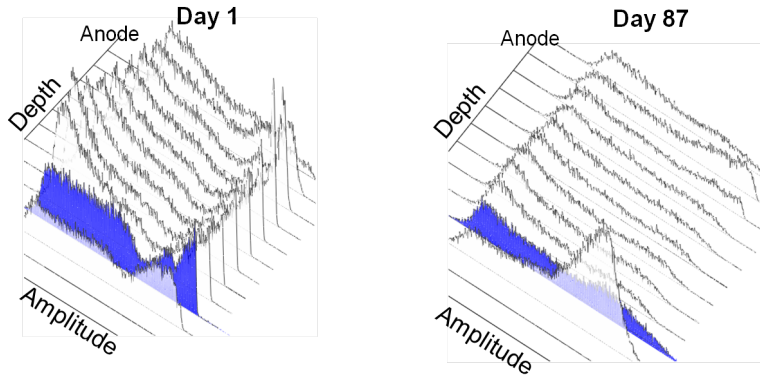
(e)



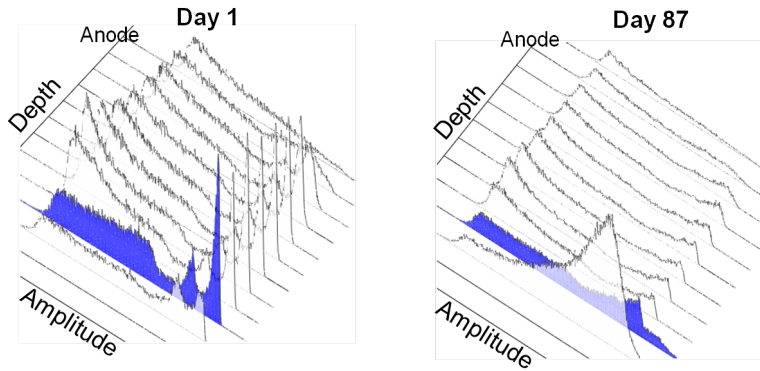
(f)



(g)

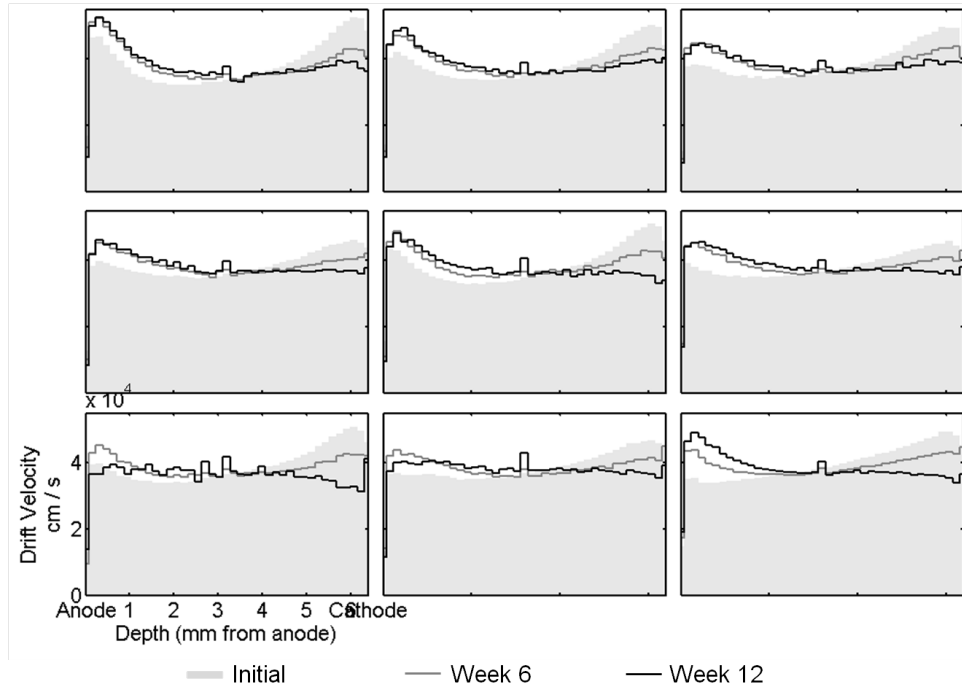


(h)

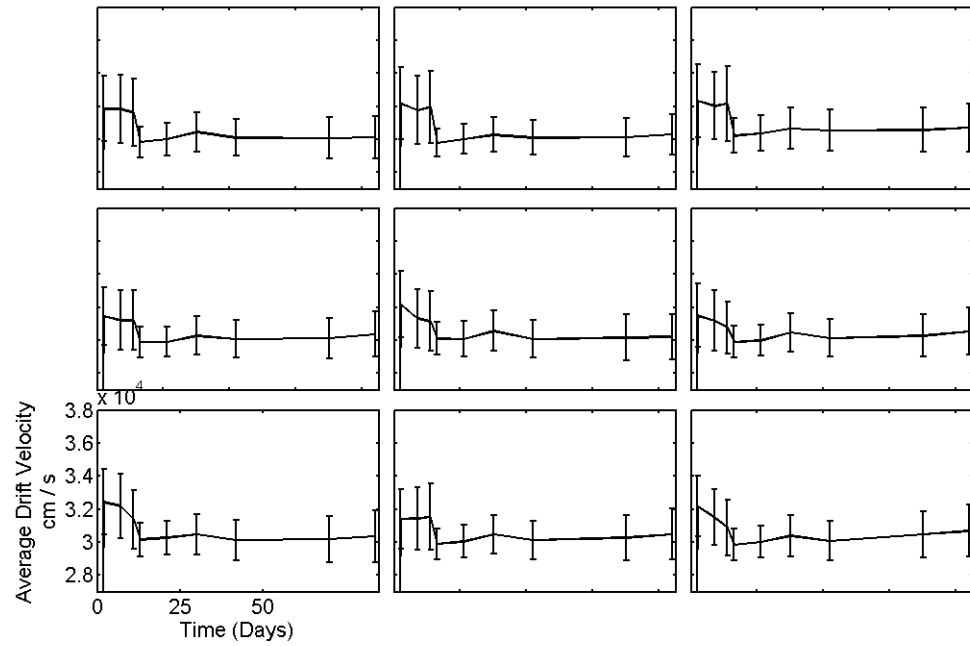


(i)

Figure 6.14: Initial and final three-dimensional spectra for all nine pixels. The pixels are shown in ascending order with figure (a) corresponding to pixel 1. These data show performance degradation occurring at all depths.



(a)



(b)

Figure 6.15: (a) Detector 47AR(R) drift velocity as a function of depth calculated from ^{241}Am alpha particle waveforms and (b) the overall average drift velocity as a function of time. Because the average drift velocity would be overestimated, the average drift velocity plot is a conservative estimate.

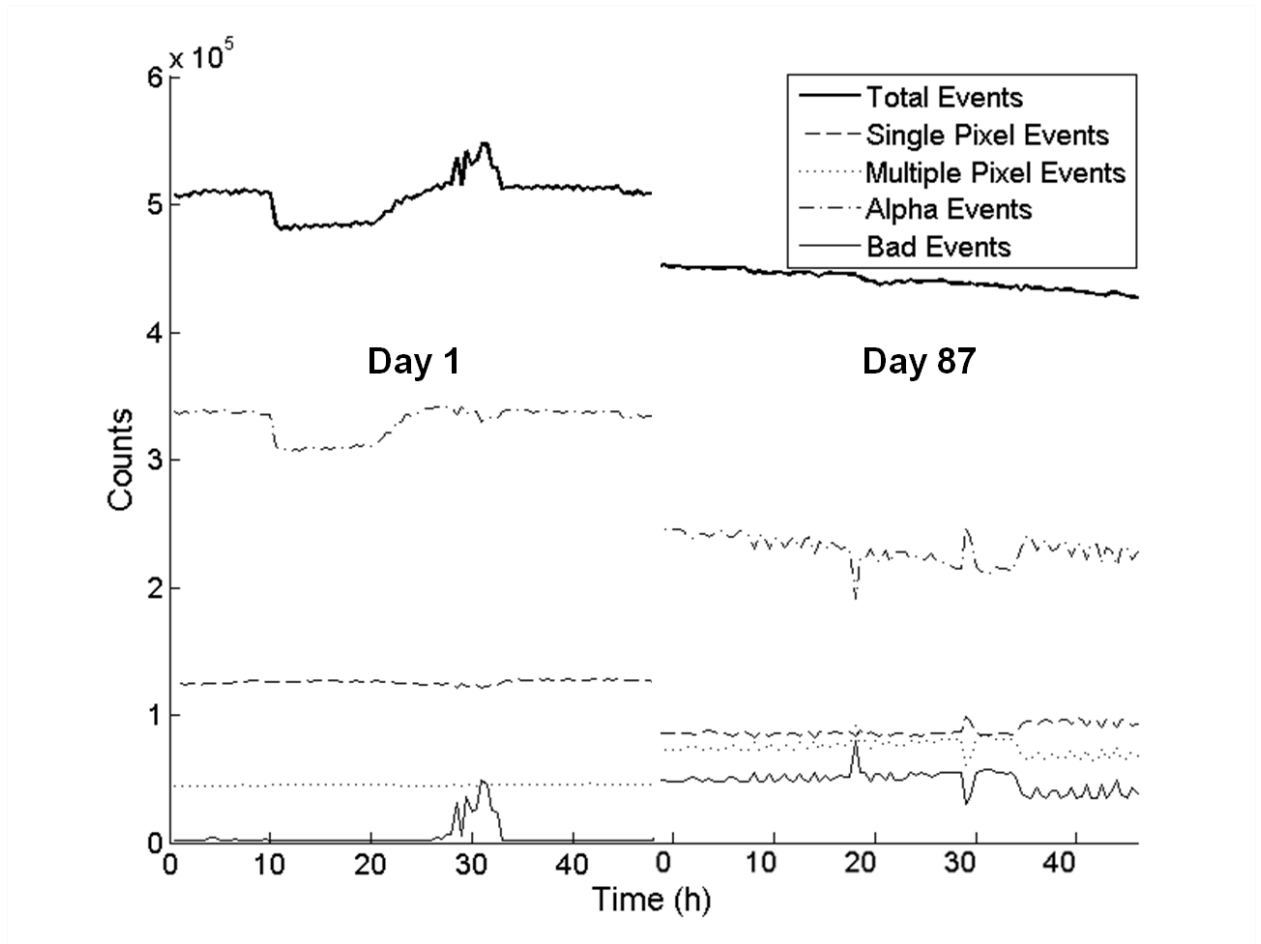


Figure 6.16: Event classification for the first 48 hour-measurement compared to the last 48 hours on the same plot for detector 47AR(R).



Figure 6.17: Optical microscope images of the anode of detectors 70BA1R after failure. The top row and left column of pixels comprise the guard ring, and the anode pixels are oriented such that pixels 1, 2, and 3 are in the top row. Any physical damage to the contact is not visually obvious.



Figure 6.18: Optical microscope images of the anode of detectors 70BA1L after failure. The bottom row and right column of pixels are connected and serve as a guard ring. The anode pixels are oriented such that pixels 1, 2, and 3 are in the top row. Large portions of the gold contact are missing in this detector

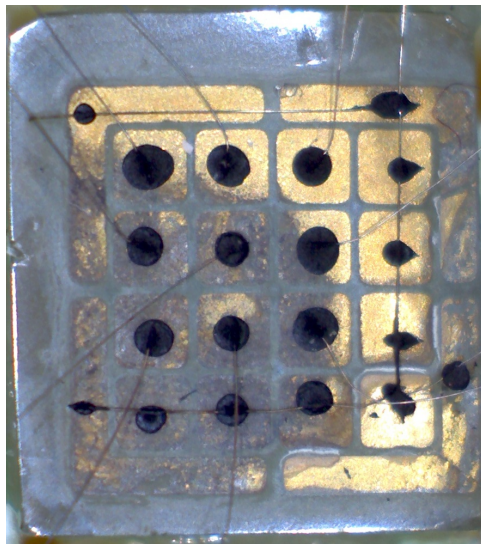


Figure 6.19: Optical microscope images of the anode of detectors 47AR(R) after failure. The bottom row and right column of pixels are connected and serve as a guard ring, and the anode pixels are oriented such that pixels 1, 2, and 3 are in the top row. Pixels 7, 8, and 9 suffered the most damage and also demonstrated the worst spectroscopic performance.

CHAPTER VII

Investigation of Other Alternative Wide-Band-Gap Materials

In the interest of diversifying the available options for room-temperature semiconductor radiation detectors, RMD, Inc. is also investigating mercuric-sulfide (HgS) and mercuric-oxide (HgO). These materials also have favorable properties compared to the materials listed in table 7.1.

7.1 Mercuric-sulfide

7.1.1 RMD, Inc. Detectors

RMD has fabricated and tested HgS detectors from lab-grown crystals as well as the naturally occurring mineral, cinnabar [76]. The detectors fabricated from lab-

Table 7.1: Properties of Semiconductor Materials

Material	Atomic Number	Density (g/cm ³)	Band Gap (eV)	Ionization Energy (eV/e-h pair)	Resistivity Ω -cm
Ge	32	5.33	0.72	3.61	
HgI ₂	80, 53	6.4	2.13	4.2	10 ¹² -10 ¹³ [4]
CdTe	48, 52	6.1	1.5	4.4	10 ⁸ -10 ⁹ [5]
CdZnTe	48, 30, 52	6.1	1.7	4.7	10 ¹⁰ -10 ¹¹ [6]
TlBr	81, 35	7.6	2.7	6.5	10 ¹¹ [7]
HgS	80, 16	8.2	2.1	—	10 ¹² [75]
HgO	80, 8	11.14	2.2	—	10 ⁹

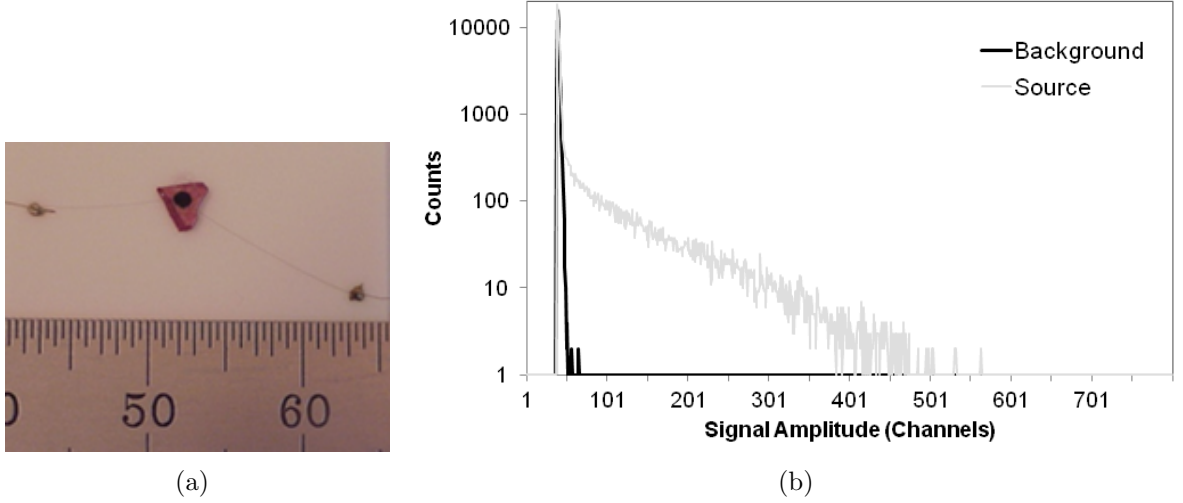


Figure 7.1: (a) Detector Cinn1 was fabricated from naturally occurring cinnabar and was 0.55 mm thick. The black dot is a conductive carbon paste used to make the 1-mm diameter electrodes. (b) Detector Cinn1 response to ^{137}Cs compared to a measurement with no source present. Both spectra were measured in 30 minutes at -300 V with a 2 μs shaping time.

created HgS showed no response to radiation while the detectors fabricated from naturally occurring cinnabar responded to both alpha-particle and gamma-ray sources. Responses to ^{137}Cs compared to similar background measurements for two different detectors are shown in figures 7.1 and 7.2.

The electron mobility-lifetime product may be estimated using the ^{137}Cs spectra in figure 7.3. From the Hecht relation described in section 2.1, it is known that the induced charge Q is proportional to

$$Q \propto \mu_e \tau_e \left(\frac{V}{D} \right) \left(1 - \exp \left[-\frac{D^2}{\mu_e \tau_e V} \right] \right) \quad (7.1)$$

where V and D are the bias voltage and the detector thickness respectively. Assuming the induced charge is due only to the movement of electrons, the induced charge at two different voltages follows equations 7.2 and 7.3 where C is a proportionality constant.

$$Q_1 = C \mu_e \tau_e \left(\frac{V_1}{D} \right) \left(1 - \exp \left[-\frac{D^2}{\mu_e \tau_e V_1} \right] \right) \quad (7.2)$$

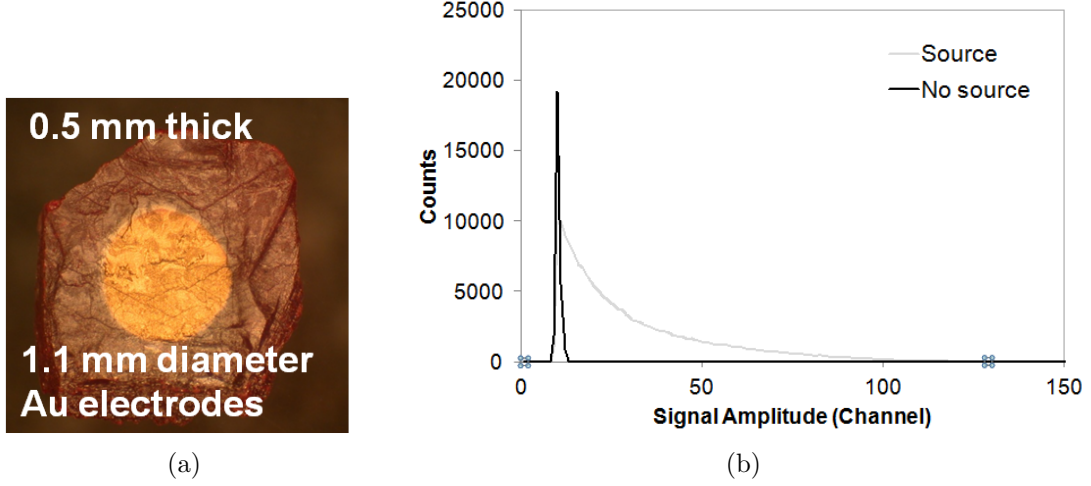


Figure 7.2: (a) Detector HgS-1 was fabricated from naturally occurring cinnabar and was 0.5 mm thick. Gold was evaporated onto the surfaces to create 1.1-mm diameter electrodes. (b) Detector HgS-1 response to ^{137}Cs compared to a measurement with no source present. Both spectra were measured in 4 hours at -500 V with a 1 μs shaping time.

$$Q_2 = C\mu_e\tau_e \left(\frac{V_2}{D} \right) \left(1 - \exp \left[-\frac{D^2}{\mu_e\tau_e V_2} \right] \right) \quad (7.3)$$

Dividing equations 7.2 and 7.3 and rearranging terms provides equation 7.4.

$$Q_1 V_2 - Q_2 V_1 = Q_1 V_2 \exp \left[-\frac{D^2}{\mu_e\tau_e V_2} \right] - Q_2 V_1 \exp \left[-\frac{D^2}{\mu_e\tau_e V_1} \right] \quad (7.4)$$

Setting $V_2 = 2V_1$ and $x = \exp \left[-\frac{D^2}{\mu_e\tau_e V_2} \right]$ leaves the quadratic equation:

$$Q_1 V_2 - Q_2 V_1 = Q_1 V_2 x - Q_2 V_1 x^2 \quad (7.5)$$

Assuming the holes are immobile relative to the electrons and the edge of the spectrum ^{137}Cs corresponds to cathode-side events, the electron mobility-lifetime product was estimated from the data in figure 7.3. The electron mobility-lifetime product may also be estimated by fitting equation 2.3 to the measured induced charge as a function of bias voltage. Calculated $\mu_e\tau_e$ values are summarized in table 7.2 and are on the order of 10^{-5} - 10^{-6} $\text{cm}^2/\text{V}\cdot\text{s}$.

Table 7.2: Calculated $\mu_e\tau_e$ Values for Detector HgS-1

Method	$\mu_e\tau_e$ ($\text{cm}^2/\text{V} \cdot \text{s}$)
$V_1 = 100 \text{ V}, V_2 = 200 \text{ V}$	9.9E-6
$V_1 = 200 \text{ V}, V_2 = 400 \text{ V}$	5.9E-6
Least Squares Fit	1.7E-6

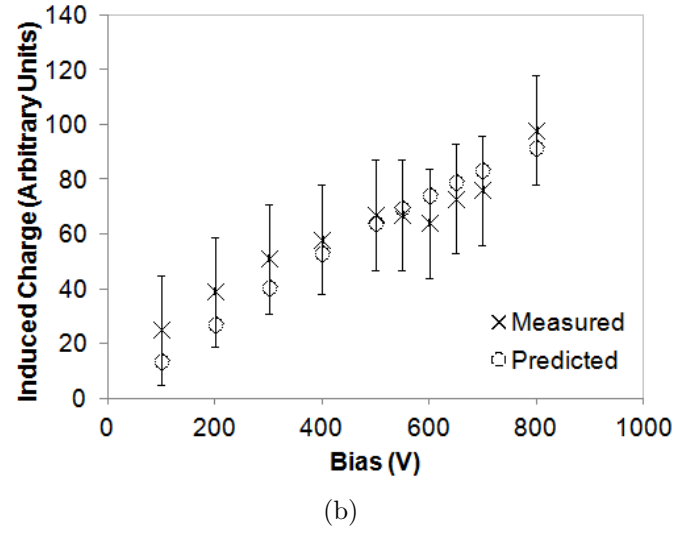
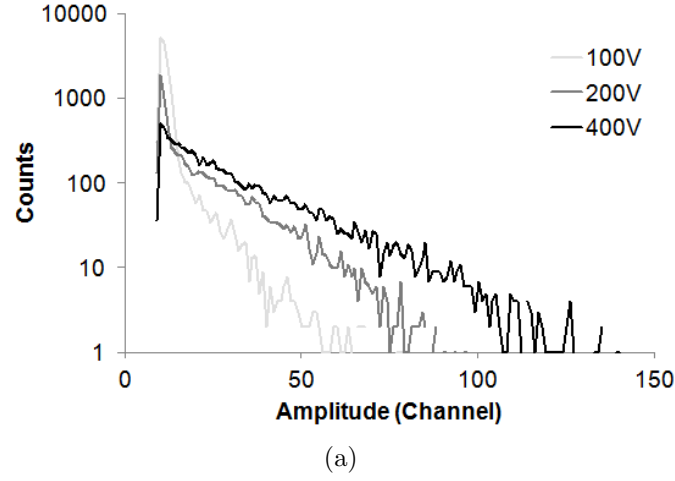


Figure 7.3: (a) ^{137}Cs spectra taken at the bias voltages used to calculate the electron mobility-lifetime product from equation 7.5. (b) The measured induced charge and the predicted induced charge calculated from a nonlinear least squares fit of equation 2.3 to the data while varying $\mu_e\tau_e$ and eN_o . The corresponding spectra are not shown in (a) for visual purposes.

7.1.2 University of Michigan Detectors

Using cinnabar purchased from a rock shop, an attempt was made to fabricate a detector at the University of Michigan. After cutting a 1-mm thick portion of the crystal in figure 7.4(a) with a diamond wafering blade, the surfaces were polished with 5 μm , 3 μm , then 2 μm alumina paper. Using an evaporator in the Lurie Nanofabrication clean room facility, 200-nm-thick gold electrodes were applied to the surfaces. Finally, contacts were applied to the electrodes using a silver conductive epoxy, shown in 7.4(b).

Prior to depositing electrodes onto the surfaces of this crystal, the crystal quality was examined using x-ray diffraction. First, by comparing the measured powder diffraction spectrum to the expected powder diffraction spectrum*, it was determined that no contaminants were present. Figure 7.5 shows the single crystal spectrum compared to the powder diffraction spectrum. While the powder diffraction spectrum produces Bragg peaks from all possible crystal orientations, the single crystal spectrum shows two Bragg peaks which correspond to Miller indices (006) and (003). Since diffraction occurs for planes of atoms that are parallel to the surface of the crystal, the orientation in figure 7.6 is known with reasonable certainty.

7.1.2.1 Radiation Response

Radiation measurements were made using the setup in figure 7.7. All sources irradiated the cathode side of the detector. Figure 7.8 an ^{241}Am alpha spectrum compared with a background spectrum measured for 22 hours and 16 hours respectively. Figure 7.9 shows the detector's response ^{57}Co gamma rays. Due to their lower energy, the ^{57}Co gamma rays have a higher probability of full energy deposition than ^{137}Cs . No clear photopeak was observed, which could be a result of crystal inhomogeneity

*In order to find the expected powder XRD spectrum the structure (trigonal hexagonal), lattice parameters ($a=4.149$, $c=9.495$), and the space group (P3121 and P3221) must be known.

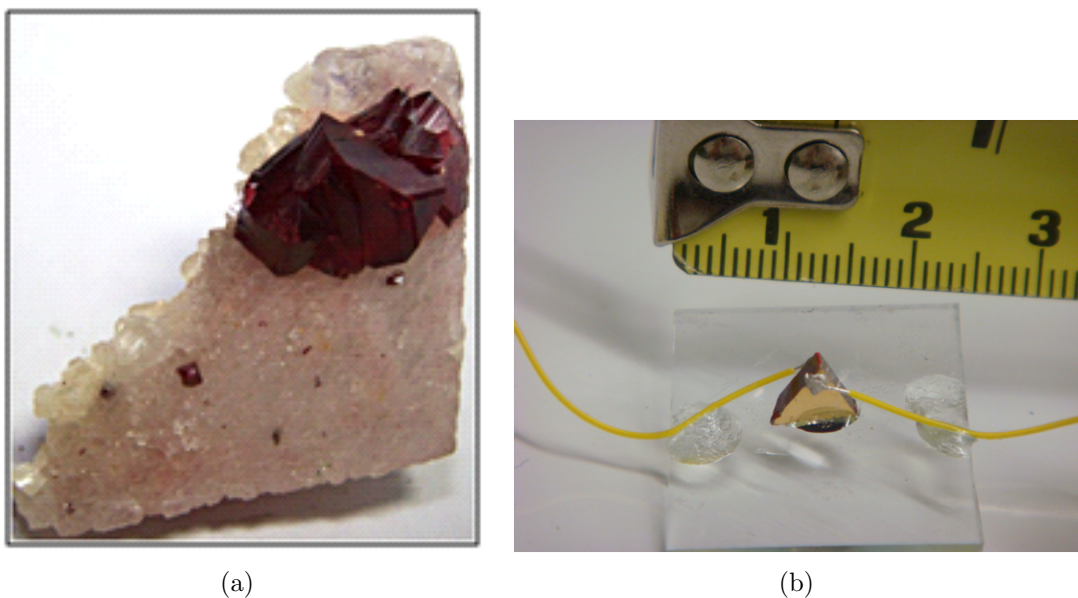


Figure 7.4: (a) The crystal as it was received from the rock shop. (b) The resulting detector.

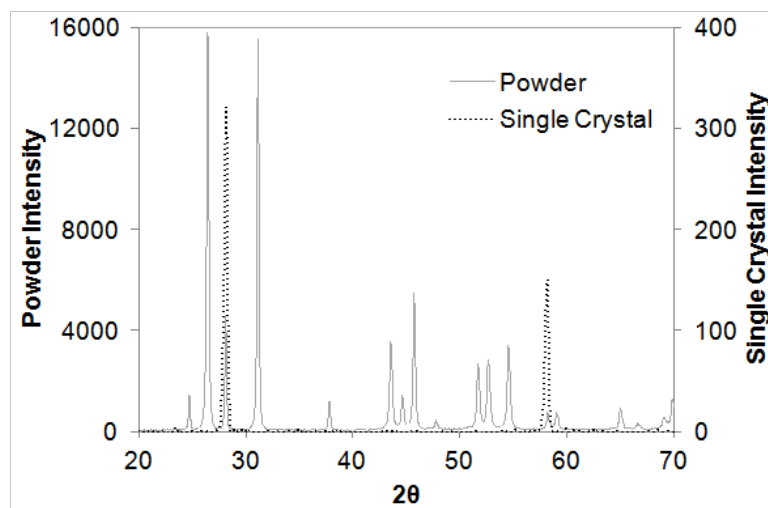


Figure 7.5: Single crystal and powder XRD spectra for the HgS detector fabrication at the University of Michigan. The powder diffraction spectrum reveals there are no contaminants. The single crystal diffraction spectrum indicates that this is a single crystal.

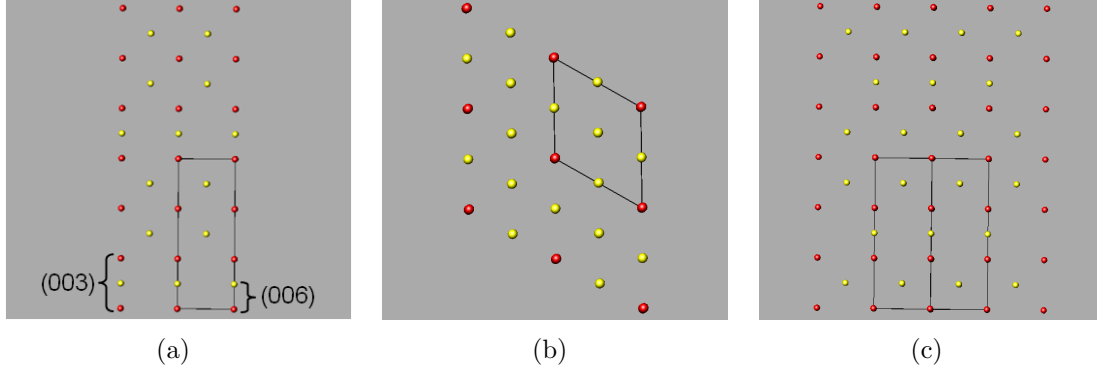


Figure 7.6: (a) The orientation of the crystal lattice. Additional aspects of the lattice are shown in (b) and (c). In all of these images, mercury atoms are visualized with large spheres, and the sulfur atoms are the smaller spheres.

and/or poor charge creation and transport.

The ^{137}Cs gamma ray spectra in figure 7.10 show the signal amplitude increased as the operating voltage increased. Using the methods described in section 7.1.1 and the data in figure 7.10, the calculated value for $\mu_e\tau_e$ is on the order of $10^{-5} \text{ cm}^2/\text{V}\cdot\text{s}$.

7.1.2.2 I-V Characterization

Current-voltage (I-V) data were measured using the Keithley 4200 semiconductor characterization system and Alessi probe station shown in figure 7.11. The resulting I-V characteristic in figure 7.12 indicates some hysteresis caused by polarization[†]. Because the device is non-Ohmic, the I-V curve is nonlinear.

7.2 Mecuric-oxide

One HgO detector was tested in this work. Using the setup in figure 7.11, the I-V characteristic was measured and is shown in figure 7.13. The detector's response to radiation was measured using the setup in figure 7.7 and is shown in figure 7.14.

[†]Polarization in this context refers to the measure of separation between positive and negative charges in the crystal.

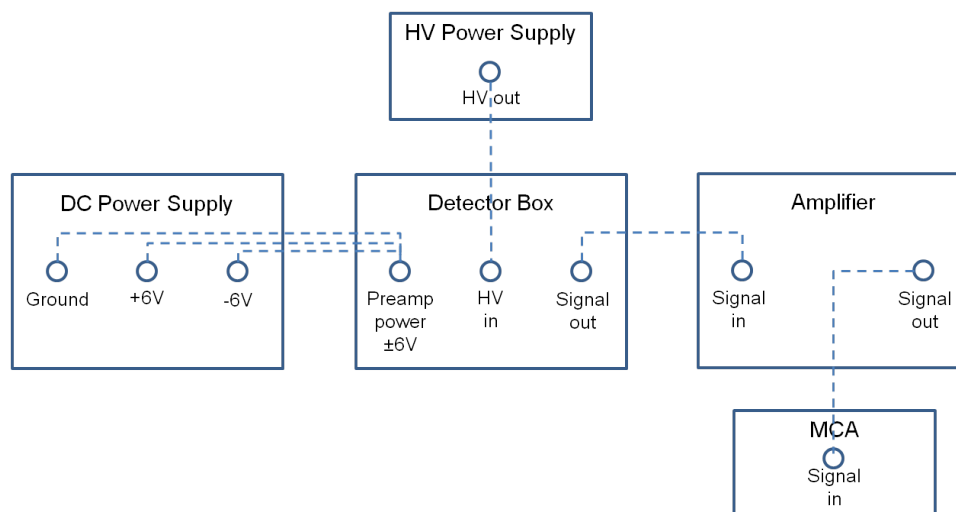


Figure 7.7: Measurement setup for HgS and HgO experiments. The preamplifier signals were connected to a Canberra model 2026 amplifier. The amplified signals were connected to an Ortec multichannel analyzer with 2048 channels.

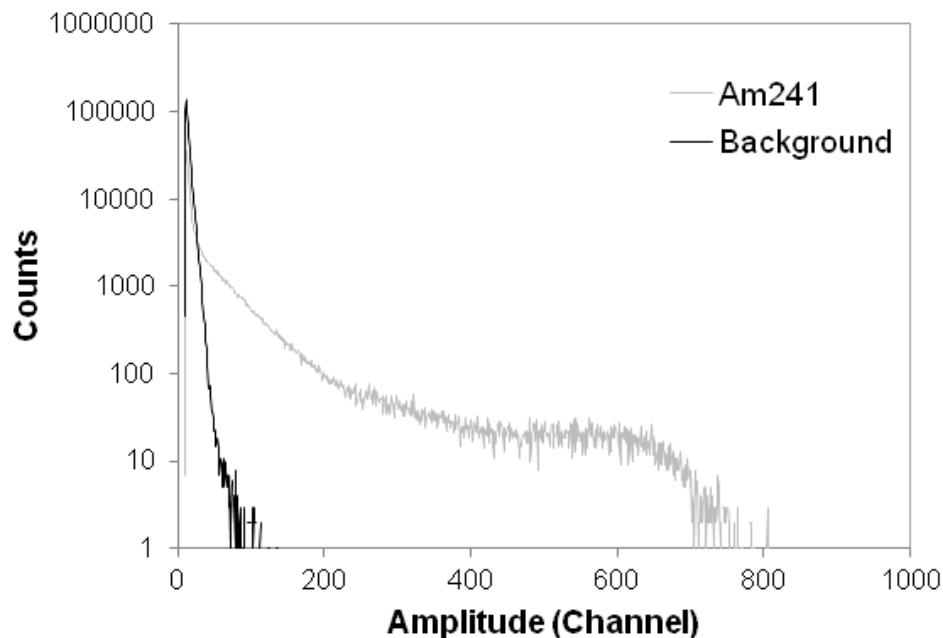


Figure 7.8: An ^{241}Am alpha spectrum measured for 22 hours compared with a background spectrum measured for 16 hours with -200 V applied bias. The shaping time was $12\ \mu\text{s}$, and the same gain setting was used for both measurements.

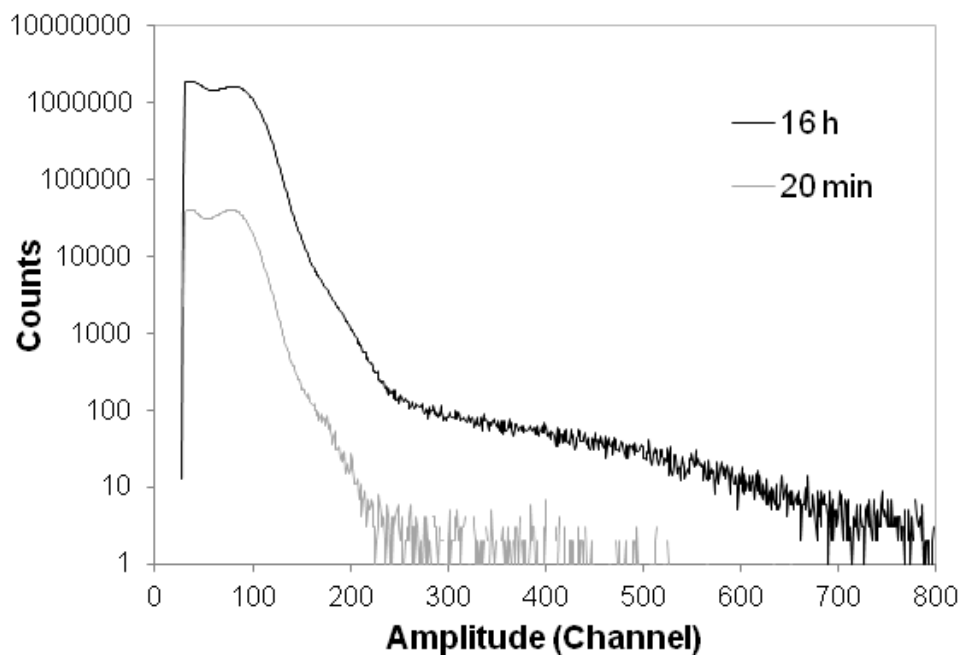


Figure 7.9: ^{57}Co spectrum measured for 20 minutes compared to a spectrum measured for 16 hours using -200 V bias. A $2\ \mu\text{s}$ shaping time was used for each measurement. Due to a lower signal amplitudes from the gamma rays, a higher gain setting was used for these measurements than what was used for the alpha measurement.

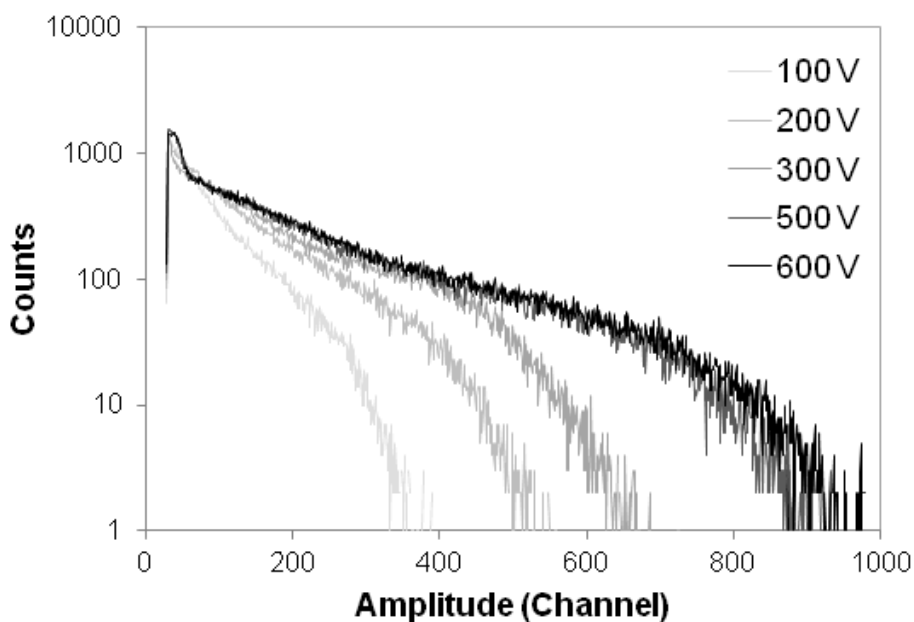
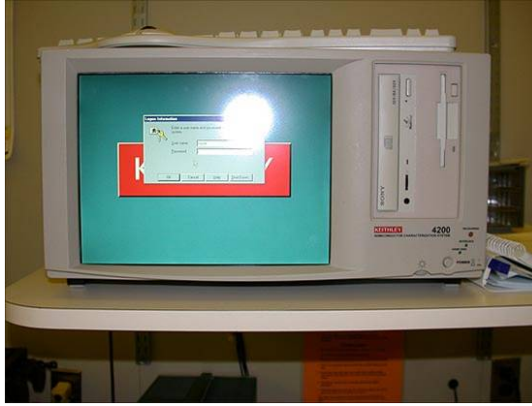
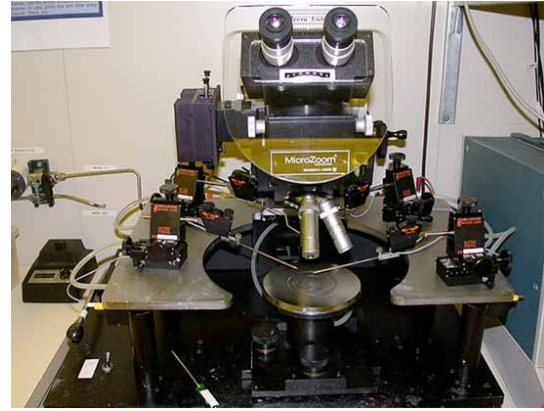


Figure 7.10: ^{137}Cs spectra measured for 20 minutes at different operating voltages. A $2\ \mu\text{s}$ shaping time was used for each measurement. The same shaping time and gain setting were used for the ^{137}Cs and ^{57}Co measurements.



(a)



(b)

Figure 7.11: (a) Keithley 4200 semiconductor characterization system and (b) the Alessi probe station used to measure HgS I-V characteristics. The device being tested was placed on the probe station stage, and the probes were put in contact with the electrodes. Then the probe station is connected to the Keithley which controls the voltage and measures the characteristics.

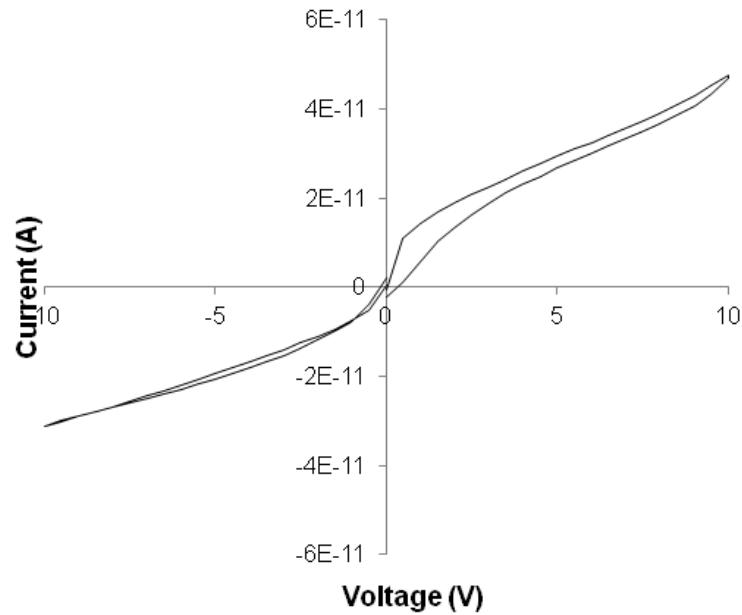


Figure 7.12: The I-V curve was generated by changing the voltage from zero to ten volts then from ten to zero volts in 0.5 V increments with no delay between measurements. The I-V curve for negative voltages was generated in the same way. The estimated resistivity from these data is $10^{11} \Omega\text{-cm}$.

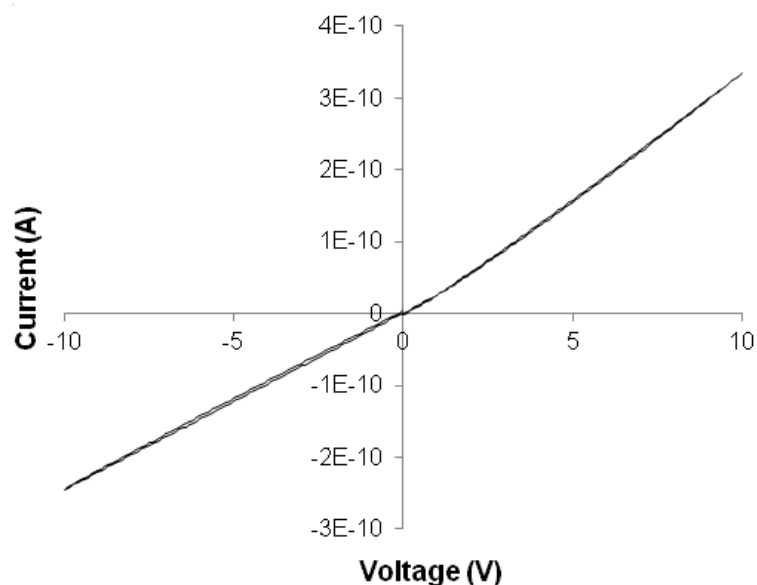


Figure 7.13: The I-V curve was generated by changing the voltage from zero to ten volts then from ten to zero volts in 0.5 V increments with no delay between measurements. The I-V curve for negative voltages was generated in the same way. The linearity of the I-V curve indicates the HgO detector is Ohmic. The resistivity was estimated from the slope of this curve to be $5\text{E}9 \Omega\text{-cm}$ and is reported in table 7.1.

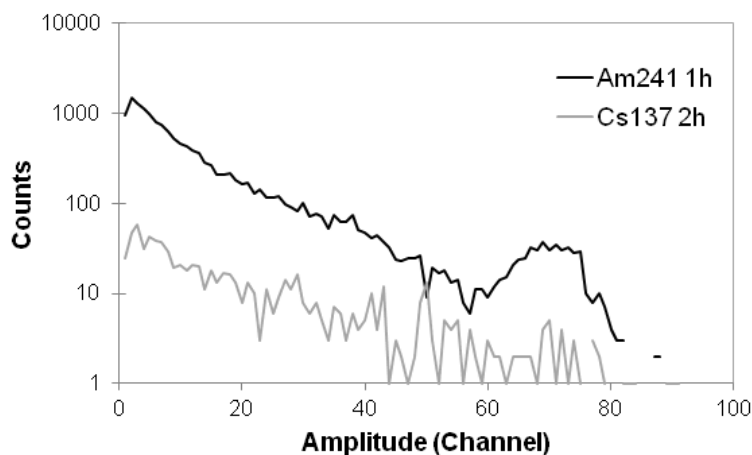


Figure 7.14: HgO response to a $0.1 \mu\text{Ci } ^{241}\text{Am}$ alpha source measured for one hour and a $100 \mu\text{Ci } ^{137}\text{Cs}$ source measured for two hours. A two-hour background measurement yielded zero counts and is not shown on the plot. The spectra were measured at an operating voltage of -350 V using a $12 \mu\text{s}$ shaping time. The detector is 0.5 mm thick with 0.6 mm diameter carbon paste electrodes

7.3 Summary

HgS and HgO detectors are in the exploratory phase, but the initial results show these detectors respond to both alpha particle and gamma ray radiation. RMD, Inc. showed similar radiation response in HgS detectors fabricated from natural crystals as well as lab-grown crystals [76]. These materials require a lot of development before they will be useful for practical applications, but their material properties are favorable for room-temperature radiation detection.

CHAPTER VIII

Conclusions and Future Work

8.1 Conclusions

From the limited number of samples, no definitive conclusions may be drawn with respect to how the manufacturing process relates to detector performance during the conditioning phase, stable operation, or the room-temperature failure process. Multiple samples achieved good spectroscopic performance during stable operation, and the depth-dependent gamma-ray data showed the material quality was consistently good between samples. Overall energy resolution of 1.01% FWHM at 662 keV and 0.78% at 662 keV on a single pixel was demonstrated.

Transient behavior was observed in some TlBr detectors immediately following bias. The initial distribution of vacancy impurities weakened the electron drift velocity, which resulted in poor spectroscopic performance. As the vacancies drifted from the detector bulk and concentrated near the electrodes, the electron drift velocity became more uniform and the spectroscopic performance improved. The re-fabricated TlBr detector tested in this work demonstrated stable behavior for the duration of its operation, which is likely due to the transition phase occurring in the test prior to re-fabrication.

As TlBr detectors failed during room-temperature operation, the electron drift velocity decreased and the spectroscopic performance degraded. Signal gain changes

from both electrodes indicate charge loss occurring near both electrodes. Research has shown that surface preparation and contact quality impact detector performance [38, 39, 77]. Furthermore, the observed physical change on the anode electrodes supports the hypothesis that thallium chemically reacts with gold contacts, catalyzing the failure process. The chemical reaction would change the crystal stoichiometry, and as a result the defect concentration would change to maintain overall charge neutrality, perpetuating ionic conduction.

8.2 Future Work

This work has shown variability in detector performance characteristics during the initial transition phase, stable operation, and the room-temperature failure process. Few detectors were tested in this work, and in order to better understand the relationship between detector performance (during all phases of operation) and fabrication, a statistically significant number of samples should be tested.

Current TlBr detectors have not demonstrated repeatable stable behavior, which is possibly due to poor storage. Once detectors demonstrate repeatable stable performance, the necessity for multiple conditioning phases should be tested. If impurity-compensating vacancies collect beneath the electrodes while the detector operates at bias, the random thermal motion of these defects occurring while the detector rests in storage could necessitate a conditioning phase each time the detector is biased.

Because the electron drift velocity calculated from alpha waveforms assumes the entire detector is fully active, the average electron drift velocity will be underestimated if there exists a dead region. Alpha particle irradiation is the ideal method to capture the electron drift velocity as a function of detector depth, but the average electron drift velocity may be verified with two collimated gamma-ray beams, preferably near the electrodes, at a known separation distance.

Leakage current measurements may provide more useful evidence. At low tem-

peratures, the leakage current due to thermally generated charge carriers should be insignificant compared to the contribution of ionic conduction to the leakage current. An upper limit for leakage current from thermally generated charge carriers may be estimated from equations 8.1, 8.2, 8.3, 8.4, and 8.5. By assuming the effective electron and hole masses, m_e and m_h , are equal to the electron rest mass and the Fermi level ϵ_f is at the middle of the band gap, the current due to thermally generated charge carriers at -20°C would be on the order of 10^{-23} Amperes and 10^{-19} at 20°C . Any measurable leakage current would be attributed to ionic conduction. Furthermore, because ionic conduction is a function of temperature, the initial transient behavior and failure behavior may also be studied as a function of temperature.

$$I = Ae \frac{V}{t} (n_h \mu_h + n_e \mu_e) \quad (8.1)$$

$$n = N_C \exp \left(\frac{E_g - \epsilon_f}{k_B T} \right) \quad (8.2)$$

$$p = N_V \exp \left(\frac{-\epsilon_f}{k_B T} \right) \quad (8.3)$$

$$N_C = 2 \left(2\pi m_e k_B T / h^2 \right)^{3/2} \quad (8.4)$$

$$N_V = 2 \left(2\pi m_h k_B T / h^2 \right)^{3/2} \quad (8.5)$$

Either with the development of a cooled application specific integrated circuit (ASIC), or with the existing experimental setup, better event classification should be implemented. Currently, TlBr detectors are characterized using single-pixel events only, but information on multiple-pixel events may prove useful for initial transient behavior and failure analysis. Furthermore, TlBr could be evaluated as a Compton

imaging device with non-material specific Compton imaging software that has already been implemented [78, 79, 80].

BIBLIOGRAPHY

BIBLIOGRAPHY

- [1] C. L. Thrall, W. R. Kaye, Z. He, H. Kim, L. Cirignano, and K. Shah. Transient behavior in TlBr gamma-ray detectors and its analysis using 3-d position sensing. *Nuclear Science, IEEE Transactions on*, PP:1, 2012.
- [2] Will Koehler, Crystal Thrall, Zhong He, Hadong Kim, Leonard Cirignano, and Kanai Shah. Spectroscopic performance of recent TlBr detectors. *presented at IEEE Nuclear Science Symposium*, 2012.
- [3] Feng Zhang, C. Herman, Zhong He, G. De Geronimo, E. Vernon, and J. Fried. Characterization of the H3D ASIC readout system and 6.0 cm 3-D position sensitive CdZnTe detectors. *Nuclear Science, IEEE Transactions on*, 59:236–242, 2012.
- [4] M. Cuzin. Some new developments in the field of high atomic number materials. *Nuclear Instruments and Methods in Physics Research Section A: Accelerators, Spectrometers, Detectors and Associated Equipment*, 253(4):407–417, 1987.
- [5] J. Baciak. *Development of pixelated HgI₂ radiation detectors for room-temperature gamma-ray spectroscopy*. PhD thesis, University of Michigan, 2004.
- [6] Y. Eisen. Current state-of-the-art industrial and research applications using room-temperature CdTe and CdZnTe solid state detectors. *Nuclear Instruments and Methods in Physics Research Section A: Accelerators, Spectrometers, Detectors and Associated Equipment*, 428:372–378, 1999.
- [7] A.V. Churilov, G. Ciampi, Hadong Kim, L.J. Cirignano, W.M. Higgins, F. Olschner, and K.S. Shah. Thallium bromide nuclear radiation detector development. *Nuclear Science, IEEE Transactions on*, 56:1875–1881, 2009.
- [8] Robert Hofstadter. The detection of gamma-rays with thallium-activated sodium iodide crystals. *Phys. Rev.*, 75:796–810, 1949.
- [9] Ijaz-Ur-Rahman, W.A. Fisher, R. Hofstadter, and Shen Jing. Behavior of thallium bromide conduction counters. *Nuclear Instruments and Methods in Physics Research Section A: Accelerators, Spectrometers, Detectors and Associated Equipment*, 261:427 – 439, 1987.
- [10] K.S. Shah, J.C. Lund, F. Olschner, L. Moy, and M.R. Squillante. Thallium bromide radiation detectors. *Nuclear Science, IEEE Transactions on*, 36:199–202, 1989.

- [11] K.S. Shah, F. Olschner, L.P. Moy, J.C. Lund, and M.R. Squillante. Characterization of thallium bromide nuclear detectors. *Nuclear Instruments and Methods in Physics Research Section A: Accelerators, Spectrometers, Detectors and Associated Equipment*, 299:57 – 59, 1990.
- [12] F. Olschner, K.S. Shah, J.C. Lund, J. Zhang, K. Daley, S. Medrick, and M.R. Squillante. Thallium bromide semiconductor X-ray and γ -ray detectors. *Nuclear Instruments and Methods in Physics Research Section A: Accelerators, Spectrometers, Detectors and Associated Equipment*, 322:504 – 508, 1992.
- [13] K. Hitomi, T. Murayama, T. Shoji, T. Suehiro, and Y. Hiratate. Improved spectrometric characteristics of thallium bromide nuclear radiation detectors. *Nuclear Instruments and Methods in Physics Research Section A: Accelerators, Spectrometers, Detectors and Associated Equipment*, 428:372 – 378, 1999.
- [14] K Hitomi, M Matsumoto, O Muroi, T Shoji, and Y Hiratate. Characterization of thallium bromide crystals for radiation detector applications. *Journal of Crystal Growth*, 225:129 – 133, 2001.
- [15] K. Hitomi, O. Muroi, A. Matsumoto, T. Shoji, and Y. Hiratate. Large-volume thallium bromide detectors for gamma-ray spectroscopy. *Nuclear Science, IEEE Transactions on*, 48:2313 – 2316, 2001.
- [16] K Hitomi, O Muroi, T Shoji, T Suehiro, and Y Hiratate. Room temperature X- and gamma-ray detectors using thallium bromide crystals. *Nuclear Instruments and Methods in Physics Research Section A: Accelerators, Spectrometers, Detectors and Associated Equipment*, 436:160 – 164, 1999.
- [17] V Gostilo, A Owens, M Bavdaz, I Lisjutin, A Peacock, H Sipila, and S Zatoloka. A comparison of the x-ray performance of tlbr crystals grown by the bridge-manstockbarger and travelling molten zone methods. *Nuclear Instruments and Methods in Physics Research Section A: Accelerators, Spectrometers, Detectors and Associated Equipment*, 509:47 – 51, 2003.
- [18] V. Gostilo, A. Owens, M. Bavdaz, I. Lisjutin, A. Peacock, H. Sipila, and S. Zatoloka. Single detectors and pixel arrays based on tlbr. *Nuclear Science, IEEE Transactions on*, 49:2513 – 2516, 2002.
- [19] Alan Owens, M. Bavdaz, G. Brammertz, V. Gostilo, N. Haack, A. Kozorezov, I. Lisjutin, A. Peacock, and S. Zatoloka. Hard X-ray spectroscopy using a small-format TlBr array. *Nuclear Instruments and Methods in Physics Research Section A: Accelerators, Spectrometers, Detectors and Associated Equipment*, 497:359 – 369, 2003.
- [20] T Onodera, K Hitomi, T Shoji, and Y Hiratate. Pixellated thallium bromide detectors for gamma-ray spectroscopy and imaging. *Nuclear Instruments and Methods in Physics Research Section A: Accelerators, Spectrometers, Detectors and Associated Equipment*, 525:199 – 204, 2004.

- [21] T. Onodera, K. Hitomi, T. Shoji, Y. Hiratate, and H. Kitaguchi. Spectroscopic performance of pixellated thallium bromide detectors. *Nuclear Science, IEEE Transactions on*, 52:1999 – 2002, 2005.
- [22] Keitaro Hitomi, Toshiyuki Onodera, Tadayoshi Shoji, and Zhong He. Pixellated TlBr detectors with the depth sensing technique. *Nuclear Instruments and Methods in Physics Research Section A: Accelerators, Spectrometers, Detectors and Associated Equipment*, 578:235 – 238, 2007.
- [23] K. Hitomi, T. Onodera, T. Shoji, Y. Hiratate, and Zhong He. Tlbr gamma-ray spectrometers using the depth sensitive single polarity charge sensing technique. *Nuclear Science, IEEE Transactions on*, 55:1781 –1784, 2008.
- [24] Keitaro Hitomi, Toshiyuki Onodera, and Tadayoshi Shoji. Influence of zone purification process on TlBr crystals for radiation detector fabrication. *Nuclear Instruments and Methods in Physics Research Section A: Accelerators, Spectrometers, Detectors and Associated Equipment*, 579:153 – 156, 2007.
- [25] Alexei V. Churilov, William H. Higgins, Guido Ciampi, Cirignano Leonard J. Kim, Hadong, Fred Olschnerb, and Kanai S. Shah. Purification, crystal growth and detector performance of TlBr. *presented at SPIE*, 2008.
- [26] H. Kim, L. Cirignano, A. Churilov, G. Ciampi, W. Higgins, F. Olschner, and K. Shah. Developing larger TlBr detectors-detector performance. *Nuclear Science, IEEE Transactions on*, 56:819 –823, 2009.
- [27] Hadong Kim, A. Kargar, L. Cirignano, A. Churilov, G. Ciampi, W. Higgins, F. Olschner, and Kanai Shah. Recent progress in thallium bromide gamma-ray spectrometer development. *Nuclear Science, IEEE Transactions on*, 59:243 –248, 2012.
- [28] Hadong Kim, Leonard Cirignano, Alexei Churilov, Guido Ciampi, Alireza Kargar, William Higgins, Patrick O’Dougherty, Suyoung Kim, Michael R. Squillante, and Kanai Shah. Continued development of room temperature semiconductor nuclear detectors. pages 780604–780604–13, 2010.
- [29] H. Kim, A. Churilov, G. Ciampi, L. Cirignano, W. Higgins, S. Kim, P. ODougherty, F. Olschner, and Kanai Shah. Continued development of thallium bromide and related compounds for gamma-ray spectrometers. *Nuclear Instruments and Methods in Physics Research Section A: Accelerators, Spectrometers, Detectors and Associated Equipment*, 629:192 – 196, 2011.
- [30] V. Kozlov, M. Kemell, M. Vehkamäki, and M. Leskelä. Degradation effects in TlBr single crystals under prolonged bias voltage. *Nuclear Instruments and Methods in Physics Research Section A: Accelerators, Spectrometers, Detectors and Associated Equipment*, 576:10 – 14, 2007.

- [31] Mao-Hua Du. First-principles study of native defects in TlBr: carrier trapping, compensation, and polarization phenomenon. *Journal of Applied Physics*, 108:053506, 2010.
- [32] Burçin Dönmez, Zhong He, Hadong Kim, Leonard J. Cirignano, and Kanai S. Shah. The stability of TlBr detectors at low temperature. *Nuclear Instruments and Methods in Physics Research Section A: Accelerators, Spectrometers, Detectors and Associated Equipment*, 623(3):1024 – 1029, 2010.
- [33] Toshiyuki Onodera, Keitatsu Hitomi, and Tadayoshi Shoji. Spectroscopic performance and long-term stability of thallium bromide radiation detectors. *Nuclear Instruments and Methods in Physics Research Section A: Accelerators, Spectrometers, Detectors and Associated Equipment*, 568:433 – 436, 2006.
- [34] Keitaro Hitomi, Tadayoshi Shoji, and Yoshio Niizeki. A method for suppressing polarization phenomena in TlBr detectors. *Nuclear Instruments and Methods in Physics Research Section A: Accelerators, Spectrometers, Detectors and Associated Equipment*, 585:102 – 104, 2008.
- [35] Keitaro Hitomi, Yohei Kikuchi, Tadayoshi Shoji, and Keizo Ishii. Improvement of energy resolutions in TlBr detectors. *Nuclear Instruments and Methods in Physics Research Section A: Accelerators, Spectrometers, Detectors and Associated Equipment*, 607:112 – 115, 2009.
- [36] K. Hitomi, Y. Kikuchi, T. Shoji, and K. Ishii. Polarization phenomena in TlBr detectors. *IEEE Transactions on Nuclear Science*, 56:1859 – 1862, 2009.
- [37] Keitaro Hitomi, Tadayoshi Shoji, and Keizo Ishii. Advances in tlbr detector development. *Journal of Crystal Growth*, pages –, 2013.
- [38] A. M. Conway, L. F. Voss, A. J. Nelson, P. R. Beck, R. T. Graff, R. J. Nikolic, S. A. Payne, H. Kim, L. J. Cirignano, and K. Shah. Long-term room temperature stability of tlbr gamma detectors. *presented at SPIE*, pages 81420J–81420J–9, 2011.
- [39] L.F. Voss, A.M. Conway, R.T. Graff, P.R. Beck, R.J. Nikolic, A.J. Nelson, S.A. Payne, Hadong Kim, L. Cirignano, and K. Shah. Surface processing of TlBr for improved gamma spectroscopy. In *Nuclear Science Symposium Conference Record (NSS/MIC), 2010 IEEE*, 2010.
- [40] L.F. Voss, A.M. Conway, R.T. Graff, P.R. Beck, R.J. Nikolic, Art J. Nelson, S.A. Payne, Hadong Kim, L. Cirignano, and K. Shah. Surface processing of tlbr for improved gamma spectroscopy. In *Nuclear Science Symposium Conference Record (NSS/MIC), 2010 IEEE*, pages 3746–3748, 2010.
- [41] Jae Cheon Kim, Stephen E. Anderson, Willy Kaye, Feng Zhang, Yuefeng Zhu, Sonal Joshi Kaye, and Zhong He. Charge sharing in common-grid pixelated CdZnTe detectors. *Nuclear Instruments and Methods in Physics Research*

Section A: Accelerators, Spectrometers, Detectors and Associated Equipment, 654:233 – 243, 2011.

- [42] Yuefeng Zhu, S.E. Anderson, and Zhong He. Sub-pixel position sensing for pixelated, 3-d position sensitive, wide band-gap, semiconductor, gamma-ray detectors. *Nuclear Science, IEEE Transactions on*, 58:1400 –1409, 2011.
- [43] Zhong He. Review of the shockley-ramo theorem and its application in semiconductor gamma-ray detectors. *Nuclear Instruments and Methods in Physics Research Section A: Accelerators, Spectrometers, Detectors and Associated Equipment*, 463:250 – 267, 2001.
- [44] Karl Hecht. Zum mechanismus des lichtelektrischen primärstromes in isolierenden kristallen. *Zeitschrift für Physik*, 77:235–245, 1932.
- [45] P.N. Luke. Unipolar charge sensing with coplanar electrodes-application to semiconductor detectors. *Nuclear Science, IEEE Transactions on*, 42:207 –213, 1995.
- [46] Glenn F Knoll. *Radiation Detection and Measurement, fourth edition*. John Wiley & Sons, Inc., 2010.
- [47] O. Frisch. *British Atomic Energy Report*, BR-49, 1944.
- [48] H. H. Barrett, J. D. Eskin, and H. B. Barber. Charge transport in arrays of semiconductor gamma-ray detectors. *Phys. Rev. Lett.*, 75:156–159, 1995.
- [49] Z. He, W. Li, G.F. Knoll, D.K. Wehe, J. Berry, and C.M. Stahle. 3-D position sensitive CdZnTe gamma-ray spectrometers. *Nuclear Instruments and Methods in Physics Research Section A: Accelerators, Spectrometers, Detectors and Associated Equipment*, 422:173 – 178, 1999.
- [50] Feng Zhang, Zhong He, Dan Xu, Glenn F. Knoll, David K. Wehe, and James E. Berry. Improved resolution for 3-D position sensitive CdZnTe spectrometers. *IEEE Transactions on Nuclear Science*, 51:2427, 2004.
- [51] W. Li, Z. He, G.F. Knoll, D.K. Wehe, and C.M. Stahle. Spatial variation of energy resolution in 3-D position sensitive CZT gamma-ray spectrometers. *IEEE Transactions on Nuclear Science*, 46:187, 1999.
- [52] Feng Zhang, Zhong He, and Dan Xu. Analysis of detector response using 3-D position-sensitive CZT gamma-ray spectrometers. *IEEE Transactions on Nu*, 51:3098, 2004.
- [53] Feng Zhang and Zhong He. 3d position sensitive CdZnTe gamma-ray spectrometers - improved performance with new ASICs. 2004.
- [54] Feng Zhang, Zhong He, Glenn F. Knoll, David K. Wehe, and James E. Berry. 3-D position sensitive CdZnTe spectrometer performance using third generation VAS/TAT readout electronics. *IEEE Transactions on Nuclear Science*, 52:2009, 2005.

- [55] Z. He, W. Li, G.F. Knoll, D.K. Wehe, and C.M. Stahle. Measurement of material uniformity using 3-D position sensitive CdZnTe gamma-ray spectrometers. *Nuclear Instruments and Methods in Physics Research Section A: Accelerators, Spectrometers, Detectors and Associated Equipment*, 441:459, 2000.
- [56] Feng Zhang. *Events Reconstruction in 3-D Position Sensitive CdZnTe Gamma-Ray Spectrometers*. PhD thesis, University of Michigan, 2005.
- [57] S.M. Sze and Kwok K. Ng. *Physics and Properties of Semiconductors A Review*, pages 5–75. John Wiley & Sons, Inc., 2006.
- [58] Boone B Owens. Solid state electrolytes: overview of materials and applications during the last third of the twentieth century. *Journal of Power Sources*, 90:2 – 8, 2000.
- [59] Gary S. Was. *Fundamentals of Radiation Materials Science*. Springer-Verlag Berlin Heidelberg, 2007.
- [60] Peter Bruce. *Solid State Electrochemistry*. Cambridge University Press, 1995.
- [61] P. Padma Kumar and S. Yashonath. Ionic conduction in the solid state. *Journal of Chemical Sciences*, 118:135–154, 2006.
- [62] Harry L. Tuller and Sean R. Bishop. Point defects in oxides: Tailoring materials through defect engineering. *Annual Review of Materials Research*, 41:369–398, 2011.
- [63] G. A. Samara. Pressure and temperature dependences of the ionic conductivities of the thallous halides tlcl , tlbr , and tli . *Phys. Rev. B*, 23:575–586, 1981.
- [64] S. R. Bishop, W. Higgins, G. Ciampi, A. Churilov, K. S. Shah, and H. L. Tuller. The defect and transport properties of donor doped single crystal tlbr . *Journal of The Electrochemical Society*, 158:J47–J51, 2011.
- [65] Sean R. Bishop, William Higgins, Alexei Churilov, Guido Ciampi, Hadong Kim, Leonard Cirignano, V. Biteman, Josh Tower, Kanai Shah, and Harry Tuller. Characterization of conductivity in single crystal TlBr . *ECS Transactions*, 28:333–338, 2010.
- [66] F.E. da Costa, C.H. de Mesquita, and M.M. Hamada. Temperature dependence in the long-term stability of the tlbr detector. *Nuclear Science, IEEE Transactions on*, 56:1817–1822, 2009.
- [67] A.J. Nelson, L.F. Voss, P.R. Beck, R.T. Graff, A.M. Conway, R.J. Nikolic, S.A. Payne, J.-S. Lee, H. Kim, L. Cirignano, and K. Shah. X-ray photoemission analysis of chemically modified tlbr surfaces for improved radiation detectors. *Journal of Applied Physics*, 113:143713–143713–4, 2013.

- [68] Burçin Dönmez, Zhong He, Hadong Kim, Leonard J. Cirignano, and Kanai S. Shah. Collection of holes in thick TlBr detectors at low temperature. *Nuclear Instruments and Methods in Physics Research Section A: Accelerators, Spectrometers, Detectors and Associated Equipment*, 689:7 – 11, 2012.
- [69] Jae Cheon Kim, William R. Kaye, Weiyi Wang, Feng Zhang, and Zhong He. Impact of drift time variation on the Compton image from large-volume CdZnTe crystals. *Nuclear Instruments and Methods in Physics Research Section A: Accelerators, Spectrometers, Detectors and Associated Equipment*, 683:53–62, 2012.
- [70] Vernon Gerrish. Polarization and gain in mercuric iodide gamma-ray spectrometers. *Nuclear Instruments and Methods in Physics Research Section A: Accelerators, Spectrometers, Detectors and Associated Equipment*, 322(3):402 – 413, 1992.
- [71] Alan Owens and A. Peacock. Compound semiconductor radiation detectors. *Nuclear Instruments and Methods in Physics Research Section A: Accelerators, Spectrometers, Detectors and Associated Equipment*, 531:18 – 37, 2004.
- [72] Vincenzo Lordi. Point defects in cd(zn)te and tlbr: Theory. *Journal of Crystal Growth*, pages –, 2013.
- [73] H. L. Malm and M. Martini. Polarization phenomena in cdte nuclear radiation detectors. *Nuclear Science, IEEE Transactions on*, 21(1):322–330, Feb.
- [74] A. Holzer and M. Schieber. Reduction of polarization in mercuric iodide nuclear radiation detectors. *Nuclear Science, IEEE Transactions on*, 27(1):266–271, Feb.
- [75] Michael R. Squillante, William M. Higgins, Hadong Kim, Leonard Cirignano, Guido Ciampi, Alexei Churilov, and Kanai Shah. Hgs: a rugged, stable semiconductor radiation detector material. pages 74491U–74491U–6, 2009.
- [76] Hadong Kim, Leonard Cirignano, Alexei Churilov, Guido Ciampi, Alireza Kargar, William Higgins, Patrick O’Dougherty, Suyoung Kim, Michael R. Squillante, and Kanai Shah. Continued development of room temperature semiconductor nuclear detectors. pages 780604–780604–13, 2010.
- [77] I.B. Oliveira, F.E. Costa, P.K. Kiyohara, and M.M. Hamada. Influence of crystalline surface quality on tlbr radiation detector performance. *Nuclear Science, IEEE Transactions on*, 52:2058–2062, 2005.
- [78] Weiyi Wang, Willy R. Kaye, Jae Cheon Kim, Feng Zhang, and Zhong He. Improvement of compton imaging efficiency by using side-neighbor events. *Nuclear Instruments and Methods in Physics Research Section A: Accelerators, Spectrometers, Detectors and Associated Equipment*, 687:62 – 68, 2012.
- [79] Weiyi Wang, C.G. Wahl, J.M. Jaworski, and Zhong He. Maximum-likelihood deconvolution in the spatial and spatial-energy domain for events with any number of interactions. *Nuclear Science, IEEE Transactions on*, 59:469 –478, 2012.

- [80] C.G. Wahl and Zhong He. Gamma-ray point-source detection in unknown background using 3d-position-sensitive semiconductor detectors. *Nuclear Science, IEEE Transactions on*, 58:605–613, 2011.